HEAVY QUARKONIUM PRODUCTION AT $\sqrt{S_{NN}} = 200$ GEV

A Dissertation

by

MATTHEW CLARE CERVANTES

Submitted to the Office of Graduate Studies of
Texas A&M University
in partial fulfillment of the requirements for the degree of

DOCTOR OF PHILOSOPHY

Approved by:

Chair of Committee,	Saskia Mioduszewski
Committee Members,	Carl A. Gagliardi
	Ralf Rapp
	Che-Ming Ko
	Sherry Yennello
Department Head,	George R. Welch

December 2012

Major Subject: Physics

ABSTRACT

Heavy quarkonium production is not fully understood, but often described by two different models, the Color Singlet Model (CSM), and the Color Octet Model (COM). Previous measurements at the Tevatron collider by the CDF and D0 experiments are not fully in agreement with predicted observables from either model. The Relativistic Heavy Ion Collider (RHIC), and the Solenoidal Tracker At RHIC (STAR) is well suited to further explore heavy quarkonium production. The Heavy Flavor program in STAR encompasses various heavy-flavor analyses, taking advantage of its large solid-angle acceptance, including measurements that explore the properties of heavy quarkonium production using J/ψ and Upsilon (Υ) reconstructions via the di-electron channel, in p+p, d+Au, Cu+Cu, and Au+Au collision systems. This thesis presents results of reconstructed Upsilon (Υ) to study the Upsilon(nS) [n = 1, 2, 3] line-shape and measurements of the production-related observables of spin-alignment ('polarization') and Upsilon + hadron correlations (Υ + h) to investigate the Upsilon production mechanism, using triggered data from Run-8 (2008) d+Au and Run-9 (2009) p+p collisions at $\sqrt{s_{NN}} = 200$ GeV, detected at STAR. The result of the spin-alignment measurement is $\alpha = 1 \pm 0.3$ with χ^2/n.d.f. $= 18.71/7$ indicating a large (transverse) polarization. The measurement of hadronic activity near the vicinity of an Upsilon, within current uncertainties, is in reasonable agreement with both CSM and COM predictions from PYTHIA, but slightly favors the COM prediction for the near-side Υ + h correlation.

To my Mother and Father, and Michael

ACKNOWLEDGEMENTS

Dr. Mioduszewski accepted me as her student during a very critical moment in my academic career. A thesis advisor and a friend, I am indebted to her for the completion of this dissertation.

To William Lynn, for providing a reassuring hand in my affairs in Kansas while I have spent my time here in Texas. He has done more for my family during my absence than I could possibly repay. To Dr. Dave Besson and Peter Brabant, whom both introduced me to the field of experimental high energy physics while an undergraduate at the University of Kansas. I appreciate their encouragement to pursue my Ph.D., and consider them irreplaceable friends in my life.

To the Texas A&M Cyclotron Institute and the STAR collaboration. To Dr. Hyo-In Park, Dr. Jim Drachenberg, and Yasser Mohammed for listening; without their care to listen, there is no doubt that my path through this analysis would have been much more difficult and precarious. To Dr. Rory F. Clarke, for the initial software development making this analysis possible, and for the many in-depth and late-night discussions, without which not only would my personal understanding of this analysis have suffered, but my overall world-view would be less. To Dr. Ahmed Hamed for his generosity, communication, and time spent performing various consistency checks against my analysis. To Dr. Pibero Kisa Djawotho, for discussions on each of the analysis topics found within this thesis, for the evolution, implementation, and testing of much of the software used to perform this analysis. Ahmed and Pibero are two of the most sincere men that I have ever met. To Dr. Che-Ming Ko, for the kind words after the defense of my dissertation. To Dr. Michael Weimer, for the kind words upon hearing of the defense of my dissertation, and sentiments of sympathy on the passing

of my brother. To Kevin Resil for his succinct statement on the topic of ignorance: 'We [physicists] can admit our ignorance, and yet still function. That is our strength. Most people [cannot] do either of those, or both. I am all about being ignorant properly. We are all born into ignorance, so that is not the problem with people. The problem is people don't know how to be ignorant. They are incapable of living with doubt in the world.' To Dr. Murad Sarsour, Dr. Lorenzo Ravagli, Dr. Xingbo Zhao, Dr. Vladilen Goldberg, Dr. Nate Pogue, Dr. Sheldon Campbell, Dr. Au Kim Vong, Dr. Zhonghai Liu, Dr. Eunsin Lee and Grace, Dr. Noam Erez, Dr. Richard Arnowitt, Dr. Valery Pokrovsky, Dr. Ronald Bryan, Robert Burch, David Carson Fuls, Lucas Naveira, Sandi Smith, Thomas Weimar, Shuai Yang, Sergio Dagach, Michael Cone, Sam Gooding, Dave Maffei, Ricardo Castro, Jonathan Button and Elisabeth, Tracy Harrell, Juan Baca and Elizabeth Mora, Dat Nguyen, and Jonathan Kovar. Sanity near the end of graduate work is due to Ludwig van Beethoven, Mini-Ludwig, Johann Pachelbel, Uh or sand, the cognition of birds, a black 650i, and my Yamaha P-155.

I met Abigail during my second year of graduate school. Vonda Finke noticed a female, chocolate Labrador puppy for sale in the local newspaper. Initially, I was told that she had already been selected and was no longer available, but a few days later a phone call informed me that her status was now available. There is not the time nor space available to express how much Abigail has meant to me. I promised Abigail a good life the first night with her, but because of Quantum Mechanics, I needed her patience. It worked. Abigail ate a bit of my quantum mechanics homework that semester, and over the next few years, destroyed books on Calculus, Differential Equations, Partial Differential Equations, Linear Algebra, and Mathematical Methods for Physicists. Abigail will be missed some day, and I want to thank my friend Vonda, for having acted on my subtle comment about having wanted a chocolate colored Labrador. I also want to express that Vonda provided to

me, a new discovery about myself - that the moment does not always last forever, and that it is important to laugh and smile and not be afraid to sometimes act like a child. We should all do better to not lose sight of that. Vonda is a very intelligent and respectable woman, with a disarming personality and the ability to effortlessly make friends in a room full of strangers. I wish her success in current and future endeavors and hope to maintain our friendship. I thank Dr. Ranjini Murthy for a phone call about a puppy found on the side of a road, in a cardboard box, that acquired the name Sarah. Sarah also holds a special place in my heart, though not quite as scholarly as Abigail. Instead of eating my homework and textbooks, Sarah chewed on furniture and pilfered through my trashcan. It is very peculiar to have found coffee grinds in each of their teeth. Sarah has a very sweet disposition and is also now growing herself a grey chin; only a few years younger than Abigail, Sarah has also been by my side for many of the well over one thousand sleepless nights spent in pursuit of this Ph.D. I consider myself lucky to have had their companionship over these years. They have both helped to teach me that time and age will ultimately catch us all, and that love can be just as unspoken as it is expressive. They have expressed love with their faces and eyes, and I will always think of them.

I also have much admiration and respect for a very special woman and her son, Marina and Ray. She is as much responsible for making me a better person as 'uh or sand' is for keeping me sane. As much as I have accumulated across the spectrum of academia, I have with the luck of a fool, stumbled upon another masterpiece. We once had a discussion about the need for the part of a clown, and now I understand, as it has already been written: 'We all need the clowns to make us smile.' - Journey.

I owe absolutely everything to my parents, Andrew and Beverly Cervantes, whom sacrificed and stressed the value of education - their confidence in me provides me with confidence in myself. To my seven siblings: Michael, Andrea, Karen, Marcia,

Enrique, David, and Amanda. To my nephew, Nathan Cervantes. To my grandparents, aunts, uncles, cousins, nieces, nephews, brother- and sister-in-laws, and all family for their words of encouragement.

My oldest brother, Michael Brandon Cervantes, suffered a stroke days prior to the defense of this dissertation. Loss has a way of focusing one's purview of life onto its simplest, but most important pieces, forcing perspective and reflection on the lives of those around us instead of our own. As much as I have collected knowledge, I hold no misconception that I fully grasp the impact of what it means to have the love and support of those whom were, and still remain my life. I concede that without them, I would not have made it this far, and that without them I will never be the same. I told my brother in his last hours that every time someone called me 'Dr.', that I would think of him. His life departed from my life much too early, and before I could attempt to repay him for all the good things in life that he had shared with me. What Michael did for me, and the many memories that his life has given to mine, I will keep to help me through my own life, when I need to be reminded of how great one can become through silent acts of giving. I will miss your phone calls, the KU and WSU games, and the pick-up basketball - but, I will now take my memory of you with me, wherever this life takes me, because as you used to always say, 'life goes on.' May you also know that I, Janet and Claire, and the rest of us continue to miss and love you. God bless your kind soul and may we find some comfort in knowing that you took pieces of us with you as well. Rock Chalk Jayhawk!

I thank my thesis committee chair and members: Dr. Saskia Mioduszewski, Dr. Carl A. Gagliardi, Dr. Ralf Rapp, Dr. Che-Ming Ko, and Dr. Sherry Yennello for gathering at the final defense of this dissertation, on August 31, 2012. I will always associate the successful defense of this dissertation with the memory of my brother, Michael B. Cervantes (December 5, 1959 - September 1, 2012).

TABLE OF CONTENTS

LIST OF FIGURES

LIST OF TABLES

1. INTRODUCTION

Physics as a discipline, is anchored to observation and measurement. The attempt at ordering the Universe is achieved by constructing physical theories based on those observations, from which these physical theories are then used to make further predictions. Mathematics appears to be embedded in this Universe just as is mankind, and as such, it has become the responsibility of mankind to connect their natural curiosity of the physical to the mathematical, for the explicit purpose of probing Nature's secrets. Only within this tight framework might Nature unveil these secrets at their most simple, and deepest level - if and only if the opportunity to observe them is exercised.

The Standard Model of Particle Physics is a major achievement of 20th Century physics, allowing for the description of fundamental particle interactions to an unprecedented level of accuracy. The tenant of the Standard Model is that the fundamental forces are mediated by gauge vector boson exchange particles called 'field carriers', with the relative strength of an interaction determined by a characteristic 'coupling' of the field carrier to a particle of 'unit charge.' All particles possessing electrical charge are affected by the electromagnetic force, with the massless photon being the field carrier. Closely related is the weak force, carried by the massive $W^{\pm}$ and Z^0 gauge vector bosons, acting on particles possessing 'flavor charge.' The theoretical models for these interactions are called Quantum Electrodynamics (QED) and Quantum Flavordynamics (QFD), respectively. The most dominant of the Standard Model forces on the scale of, and below, the nucleon size (≈ 1 fm $= 10^{-15}$ m) is the strong force. The strong force gauge vector bosons, the 'gluons', mediate all quark interactions. A complexity of the strong force, relative to electromagnetic and

weak forces, is that the gluons themselves carry 'color charge', and hence, the gluon self-interactions play a significant role in strong force processes. The theory of the strong interactions is Quantum Chromodynamics (QCD).

The fundamental interactions of QED, QFD, and QCD dominate on the quantum scale and are each highly successful, yet there does remain deficiency in understanding. The role of the weakest of the four fundamental forces on the quantum scale is unknown - the gravitational force. Historically, gravity is precluded from interacting with elementary particles within the framework of Standard Model. It poses huge technical and theoretical challenges - issues that lay beyond the scope of this thesis. However, the relative strength of gravity is so much weaker than the other three fundamental forces on the quantum scale, that its absence has allowed for the predictive power of the Standard Model. The quantum mechanical viewpoint of gravity is that it acts between all particles with 'mass charge' and a yet to be identified 'gravitational field carrier.' While the Standard Model of fundamental interactions has been confirmed by almost all experimental observations to date, the exclusion of gravitation from the Standard Model dictates that it cannot stand as a complete theory.

Not only does the Standard Model lack the capacity to incorporate gravitation, it also fails to fully describe the lepton family; there are no predictions for non-zero neutrino masses without resorting to extensions of the Standard Model. The Standard Model also fails to describe present Cosmological models and known cosmological observations, which suggest that 22% of total mass-energy of the observable Universe is made up of Dark Matter, and that 74% of total mass-energy of the observable Universe is tied up in Dark Energy [42] - reducing the Standard Model contribution to a mere 4% of the observable Universe.

1.1 The Standard Model

The Standard Model is a Lagrangian Quantum Field Theory based upon the idea of local gauge invariance. The gauge symmetry group of the Standard Model is $SU(3)_C$ x $SU(2)_L$ x $U(1)_Y$, where $SU(3)_C$ is the symmetry group describing the strong interactions, and $SU(2)_L$ x $U(1)_Y$ represents the symmetry group of the electroweak sector describing the weak and electromagnetic interactions.

Figure 1.1 shows the fundamental particle content of the Standard Model, that are categorized into two groups of particles; the fermions of half-integral spin obeying Fermi-Dirac statistics and the gauge vector bosons of integral spin obeying Bose-Einstein statistics. There are 12 known fermions, each with a corresponding anti-particle; the quark family consisting of six quarks of type up (u), down (d), strange (s), charm (c), bottom (b) and top (t), and the lepton family consisting of six leptons of type electron (e), muon (μ) and the tauon (τ), and their corresponding neutrinos.

The defining property of the quarks is that they carry a quantum number defined as 'color charge', and hence, interactions take place via the strong force. The color charge is quantized as colors of red, blue, and green. The anti-particle of a quark (anti-quark) also carries the color charge, but in the case of the anti-quark, the color charge is labeled anti-red, anti-blue, and anti-green. Nature strictly forbids the observation of quark combinations, hadrons, that have a residual color, i.e. the hadrons must be colorless. In fact, QCD forbids the observation of a free, isolated, color charge. It is forbidden to observe a free quark in nature.

The strong or 'color force' interaction between quarks is described in terms of the gauge vector bosons of $SU(3)_C$. There are 9 gluon states carrying the three quantum numbers of color. However, one of the gluon states is a color-singlet state, $(r\bar{r} + b\bar{b} + g\bar{g})/\sqrt{3}$, which only allows interactions with other color-singlet states and

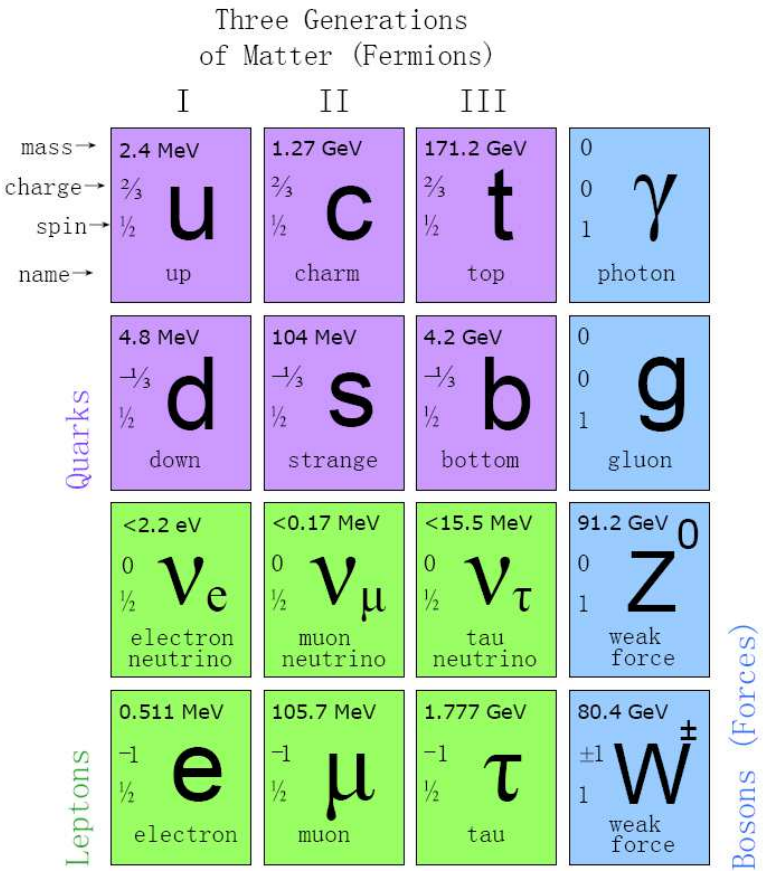

Figure 1.1: The Standard Model.

therefore, does not exist. The number of mediating bosons is 3^2 - 1 = 8. This eight mediating-gluons of QCD is called an eightfold multiplicity [34], and gluons are labeled by a combination of color and anti-color charges. The consequence of the $SU(3)_C$ symmetry of the color interaction means that the mediating gluons are a massless. The intrinsic property that a gluon has a color charge allows gluons to interact with other gluons. The gluon self-interaction in QCD underpins the mechanism for which a bound state of quarks experiences a binding potential that increases with separation distance between quarks, thus confining quarks to colorless

combinations. The gluons and quark interactions are described by the theory of QCD.

Leptons do not carry a color charge, but instead the leptons e, μ and τ carry integral electric charge, thus interactions take place via the electromagnetic force. The three corresponding neutrinos do not carry electric charge, and their motion is directly influenced only by the weak nuclear force.

The theories of QED, QFD, and QCD lend great reach to the Standard Model, and they are used to describe a great range of interactions between the particles: the electromagnetic force description of Bhabha scattering [17]; the weak force beta decay of the lone neutron [58]; the strong force, being responsible for 'gluing' together three quarks to form hadronic matter called protons and neutrons, which in turn bundle themselves together to serve as the core of an atomic nucleus [68]; to the extensive catalogue of hadrons that are built up from quarks [34]. The Standard Model is not complete, but it has thus far been proven to be an accurate theory.

1.2 Quantum Electrodynamics

Mathematically, Quantum Electrodynamics (QED) is an Abelian gauge theory with the symmetry group $U(1)_Y$ and has one gauge field. The theory of QED describes charged interactions mediated by a massless photon. Figure 1.2 shows the primitive vertex of QED - a particle of charge 'e' moving in space-time enters, emits (or absorbs) a photon, then exits[1].

The quantitative approach to QED interactions is a systematic building up of primitive QED vertices in the framework of Feynman diagrams formulated by R.P. Feynman [32] [33]. The calculation of the Feynman diagram is done in accord with

[1]The electron cannot emit a virtual photon in free space, it needs some other 'real' charge to properly close the diagram.

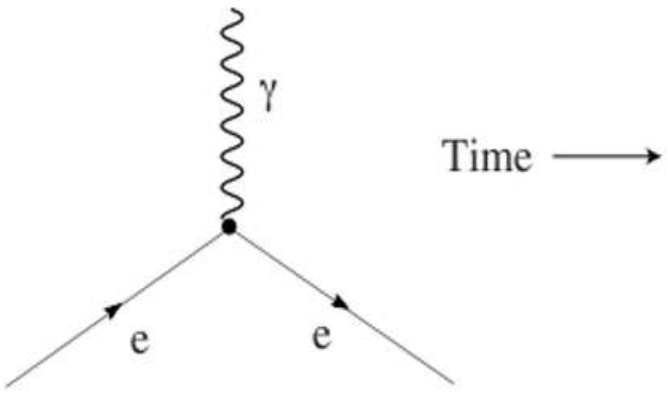

Figure 1.2: Primitive vertex of QED.

the Feynman-calculus, and the representation of a QED process by Feynman diagrams provides an aesthetically intuitive approach to study QED interactions. The lowest-order physical diagrams are called 'tree-level' Feynman diagrams, while the higher-order (increasing number of vertices) diagrams have internal loops - these loop diagrams require 'renormalization' under an appropriate renormalization-scheme. However, any given QED process taking place will be represented by infinitely many Feynman diagrams with ever increasing numbers of vertices. The small nature of the fine structure constant, $\alpha_{em} \approx 1/137$ allows for these diagrams to be interpreted as a perturbative expansion, and higher orders rapidly become less significant to the overall QED calculation. In QED, each vertex within a diagram introduces a characteristic coupling factor $g_{em} = \sqrt{4\pi\alpha_{em}}$, and thus, for the physical process in question the subsequent QED calculation becomes less and less sensitive to diagrams containing 'higher-order' numbers of vertices.

The Heisenberg Uncertainty Principle of quantum mechanics, $\Delta E \Delta t \geq \hbar$, dictates

that the energy of empty space-time itself undergoes vacuum fluctuations within the uncertainty of time between physical interactions. These energy fluctuations of the fermionic field results in the creation and annihilation of electron-positron pairs within the space-time QED vacuum. The influence of vacuum energy fluctuations are physically measurable. Experimental expectations with the Hydrogen atom using pre-QED theory suggested that the energy levels of $2S_{1/2}$ (n = 2, l = 0, j = 1/2) and $2P_{1/2}$ (n = 2, l = 1, j = 1/2) should remain perfectly degenerate under a pure Coulomb potential. In 1947 Lamb and Retherford experimentally demonstrated that the energy level of the S state is marginally higher than the energy level of the P state [46]. In the semiclassical framework of electromagnetic interactions the conflict between theory and experiment was unsettling. However, the findings of the Hydrogen Lamb Shift experiment was explained by the formalism of QED - the Lamb Shift directly results from the quantization of the electromagnetic field, as shown via QED calculations performed by Hans Bethe, Richard Feynman, Julian Schwinger, and Sin-Itiro Tomonaga. Figure 1.3 shows the Lamb Shift represented as a subtle radiative correction due to 'loop diagrams', for which the semiclassical framework is not sensitive. The theory of QED elegantly extended the understanding of the quantum domain.

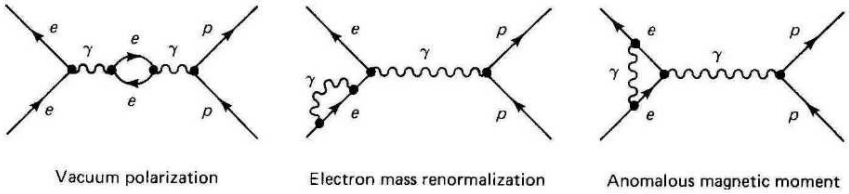

Figure 1.3: QED Lamb Shift loop diagram corrections.

In the QED vacuum, for an electron far removed from the nucleus, the QED characteristic coupling factor α_{em} rapidly tends to $\alpha_{em} \approx 1/137$ and the force experienced by the electron is Coulomb-like. However, at high energy an electron approaches the spontaneous cloud of virtual electron-positron pairs that surround the Hydrogen nucleus, leading to a 'partial screening' of the nucleus' proton charge. To extend the QED vacuum argument further, consider the case of bringing any charge 'near' an electron. In lieu of the behavior of the QED vacuum, bringing a charge in from infinity towards the electron is equivalent to probing the virtual electron-positron particle 'cloud' that surrounds that electron. Once the cloud is fully penetrated, the charge is subjected to the 'bare' charge of the electron.

Figure 1.4 (upper panel) shows that the QED coupling factor increases rapidly as the separation distance between the charge and the electron decreases. At separation distances greater than the atomic nucleus the bare charge is effectively screened by the electron's cloud of virtual electron-positron pairs. In short, the electron is the source of its own vacuum-induced virtual electron-positron pairs that screen it at large distances. Figure 1.4 (lower panel) shows the QCD analog to the phenomena of QED charge screening (upper panel), called 'color anti-screening.' Color anti-screening is attributable to the 'color vacuum polarization', which is later discussed in more detail.

The validity of QED has been experimentally tested and confirmed to a few parts in a trillion. QED successfully and matter-of-factly explained the observation of the Lamb Shift and provided the machinery to more deeply calculate other physical processes, such as Hyperfine structure and g-2. The diagrammatic approach of QED provided a theoretical-segue towards the construction of the Standard Model by enabling analogous constructions of Feynman diagrams for the theories of QFD and QCD. QFD calculations modestly fall inline with the methods used in the theory of

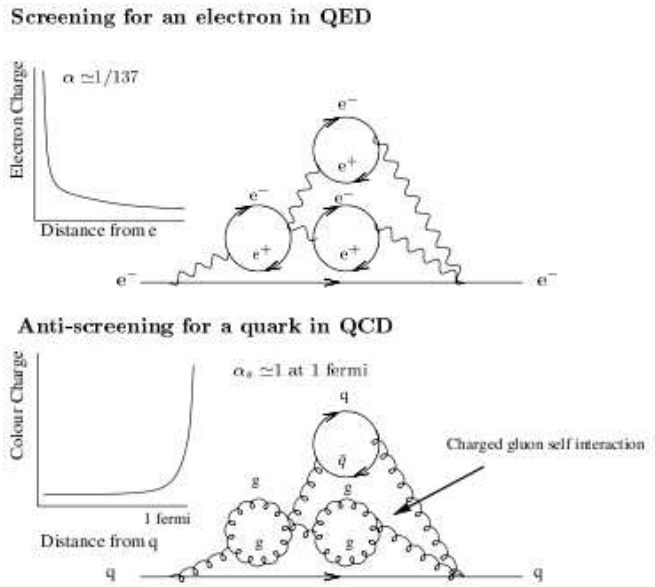

Figure 1.4: QED and QCD screening effects.

QED; QFD has been tested and confirmed to be correct to a few parts in a thousand. In fact, the electroweak unification [35] [66] [59] by Glashow, Weinberg and Salam exploited the natural similarities between QED and QFD.

A priori, in the theory of QCD, calculations are not straightforward; it is not allowed to resort to perturbative expansions for low energies, as the coupling constant α_s rapidly tends towards unity, and the higher-order diagrams of QCD can not be ignored. The QCD primitive vertex dominates the power series expansions as contributions from the higher-order vertex diagrams are included in the calculation, ultimately leading to non-convergent behavior of QCD. However, this divergent behavior does not destroy the theory of QCD; at low energies the computations of QCD are performed 'on the lattice', while at high-energies the computations are based on 'perturbative' methods which result in a mathematical treatment similar to QED.

1.3 QED and QCD Lagrangian

The Lagrangian action formalism is an immensely powerful and general method suited for the Classical and Quantum mechanics. Constructing the Lagrangian consolidates the motions of the particles and the field interactions, allowing for the equations of motion to be solved via the Euler-Lagrange variational methods. In QED and QCD, the fields are quantized and the form of the Lagrangian is expressed in standard four-vector notation, with summation over repeated indices assumed:

$$\mathcal{L}_{\mathcal{QED}} = -\frac{1}{4}F^{\mu\nu}F_{\mu\nu} - \bar{\psi}_e\gamma^\mu[\partial_\mu + ieA_\mu]\psi_e + m_e\bar{\psi}_e\psi_e \tag{1.1}$$

$$F_{\mu\nu} = \delta_\mu A_\nu - \delta_\nu A_\mu \tag{1.2}$$

$$\mathcal{L}_{\mathcal{QCD}} = -\frac{1}{4}\sum_{i=\alpha}^{8} F^{\mu\nu}_{\alpha}F^{\alpha}_{\mu\nu} - \bar{\psi}_n\gamma^\mu D_\mu\psi_n + \sum_{n=1}^{N_f} m_n\bar{\psi}_n\psi_n \tag{1.3}$$

$$F^{\alpha}_{\mu\nu} = \delta_\mu A^{\alpha}_{\nu} - \delta_\nu A^{\alpha}_{\mu} + C^{\alpha}_{\beta\gamma}A^{\beta}_{\mu}A^{\gamma}_{\nu} \tag{1.4}$$

The overall structure of $\mathcal{L}_{\mathcal{QCD}}$ is similar to $\mathcal{L}_{\mathcal{QED}}$, but differences in their structure lead to different physical phenomena. The first term in Eqn. (1.1) describes the quantized free Electromagnetic (EM) field, expressed in terms of the EM field strength tensor, and the EM four-vector potential $A^\mu = (\phi,\vec{A})$. Comparing the first term in each Lagrangian, Quantum Electrodynamics has one quantized EM field (the photon), while Quantum Chromodynamics has eight quantized 'color fields', one for each of the eight gluons. The second term in Eqn. (1.1) is the the description of the electron's field interacting with the EM field, dependent on the local gauge invariance nature of the QED Lagrangian density. The second term in Eqn. (1.3) is, in short,

the analogue to the second term in the QED Lagrangian, which accounts for colored quarks interacting with the color fields. The third term in Eqn. (1.1) accounts for a free electron at rest in otherwise 'empty' space-time, while the last term in Eqn. (1.3) represents the free[2] fermionic quarks (running from n = 1,..., N_f.), at rest. The deviation of the behavior of QCD relative to QED can be accredited to the differences in structure of their respective field tensors, described by Eqn. (1.2) and Eqn. (1.4). The third term in the QCD field tensor contains self-interactions between the field carriers (gluons), in contrast to the noninteracting field carriers (photons) of QED.

1.4 Quantum Chromodynamics

Mathematically, Quantum Chromodynamics (QCD) is a non-Abelian gauge theory with the symmetry group $SU(3)_C$. In analogy to QED, the physical aspect of the theory of QCD is the description of quark interactions being mediated by a massless gluon, the QCD field carrier. Figure 1.5 shows the primitive vertex of QCD - a quark of color moving in space-time enters, emits (or absorbs) a gluon, then exits.

In the theory of QCD, the strong interaction is much more intricate; quarks come in three different 'color charges' and because the gluons carry color charge the gluons couple to each other. The gluon self-interactions in QCD mandate that a set of primitive gluon-gluon vertex diagrams exist. Figure 1.6 shows the allowed vertices for gluons of color moving in space-time entering, then emitting, or absorbing, a gluon, then exiting.

The quantitative approach to QCD interactions mimics the building up of primitive vertices in QED - substituting primitive QED vertices for primitive QCD vertices and couplings. Analogous to contributions from QED vertices, each QCD vertex

[2]This does not infer the existence of free quarks in nature. A quark in isolation would create so many gluons from the QCD vacuum that the complete wave function would not be normalizable. Solutions corresponding to free quarks do not exist.

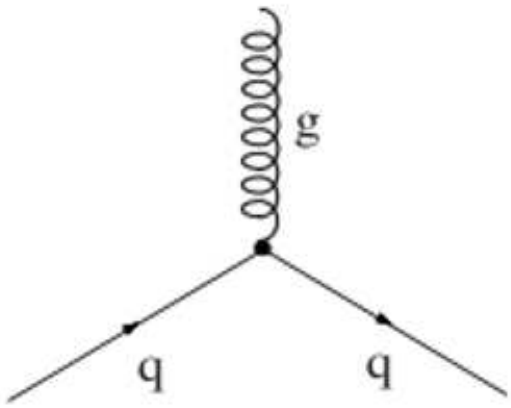

Figure 1.5: Primitive quark-gluon vertex of QCD.

within a QCD diagram introduces a characteristic coupling factor g_s. Calculations of the interactions in QCD closely follow the 'blueprint' of the Feynman calculus for QED, and as in QED, any given QCD process taking place in space-time may be represented by infinitely many Feynman diagrams. However, the perturbative series expansion of QCD diagrams are afflicted by the large size[3] of α_s. In QCD the coupling factor $g_s = \sqrt{4\pi\alpha_s} > 1$, leading to QCD calculations that become more heavily dependent on diagrams containing 'higher-order' numbers of vertices - i.e., a divergence in the theory of QCD. Quantum Chromodynamics appeared to be antithetical to the finite calculation methods (perturbative power series expansions) that worked well in Quantum Electrodynamics.

QED needs only to handle the scalar nature of electrical charge, but QCD must deal with the color charge as a vector coming from the $SU(3)_C$ group. The coupling between quarks and gluons, and gluons and gluons, is set by the strong running

[3]The strong coupling constant (α_s) is not a true constant - it is more accurately called a 'running' coupling constant.

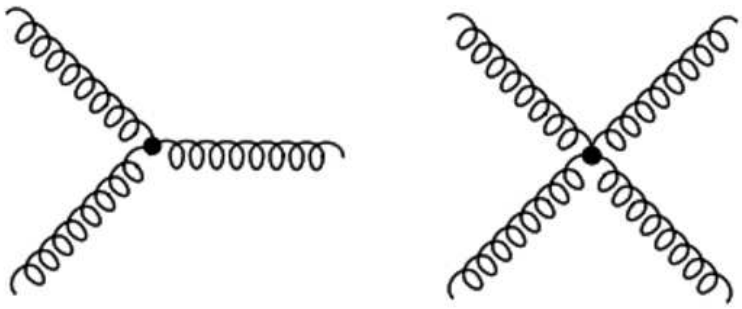

Figure 1.6: Primitive gluon-gluon vertices of QCD.

coupling constant, which is in turn set by the the vacuum renormalization. In empty space-time (low energy), the running strong coupling constant is very close to unity for the vacuum fluctuations of gluons. As previously mentioned, QCD has analogous color 'anti-screening', attributable to the 'color vacuum polarization' of the gluon field (what has been frequently referred to as the 'color field'). The level of interplay between color fields elevates the complexity of the QCD vacuum relative to the QED vacuum, because gluons possess color charge, and the color fields induced by these gluons sequentially spawn more color fields to self-interact with. The strong coupling of gluons to the color charge of the virtual gluons produced in the vacuum fluctuations means that the induced virtual gluons will induce their own colored gluon field. There is no mass barrier to overcome for the massless virtual gluon to produce the secondary virtual gluons, hence, the secondary virtual gluons will then spawn their own generation of virtual gluons with just as strong of a color field, which then again induces another field of colored virtual gluons, and so on. The QCD vacuum is quickly becoming the prototypical description of a run-away process on the quantum scale, but the run-away process is subdued by the constraint of a finite formation

time allowed by the uncertainty relation $\Delta E \Delta t \geq \hbar$. In other words, the sequentially induced colored gluon fields arising from the strong coupling to virtual gluons in the QCD vacuum will propagate out and polarize the QCD vacuum within the time Δt, allowed by the uncertainty relation. The dynamical vacuum of QCD is no different than any other dynamical system found in nature, and in QCD, the formation of the gluon color field occurs in such a way as to minimize the overall energy configuration of the vacuum. The resulting configuration of the self-inductive virtual gluon field is described as having a 'foam-like' behavior [48], and the vacuum gluons are described as a forming a 'gluon-condensate.' Figure 1.7 is a snapshot of the typical behavior seen in the 'four-dimensional' structure of the QCD vacuum gluon-field, in a space-time volume large enough to contain a couple of protons, according to lattice QCD (lQCD) simulations [41].

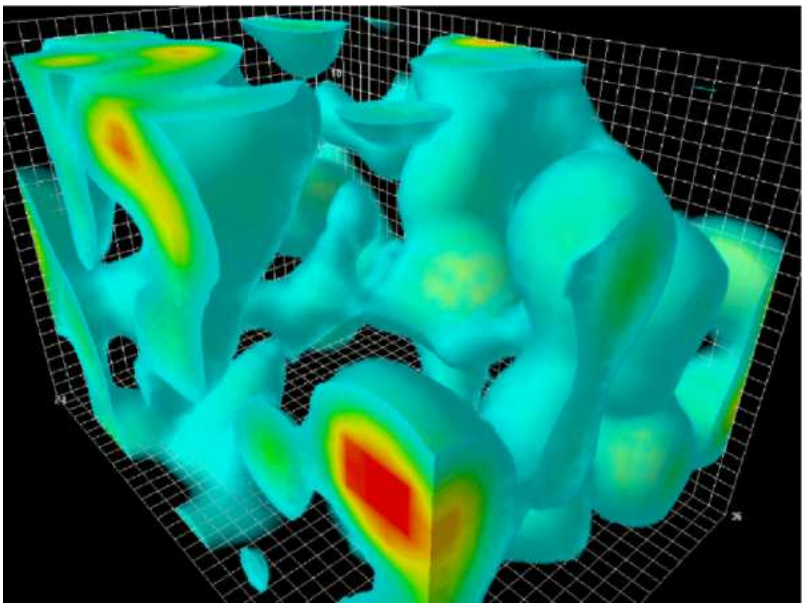

Figure 1.7: Foam-like structure of the QCD vacuum [48].

Consider an analogy to bringing an electrical test charge near the electron in the QED vacuum, but instead, the intent is to probe the nature of the QCD vacuum by considering a red colored quark in the QCD vacuum. The strong red gluon field surrounding the red quark will color-polarize the local QCD vacuum at the expense of energy necessary to overcome the original polarization of the vacuum. As the local QCD vacuum becomes polarized by the presence of the red quark, the increased local red charge is now interacting with more of the already polarized gluon vacuum, requiring even more energy. The red charge of the gluon field will propagate out, converting the whole of the QCD vacuum to this color charge; this 'run-away process' would require an infinite amount of energy. To negate this run-away process, let us consider an anti-red colored quark as being locally 'close' to the red colored quark. It can be shown that the color polarization of the red quark and anti-red quark system would become 'localized' and the overall colorless combination of the red and anti-red quark pair will disturb the QCD vacuum 'less' than if the red quark was 'alone' in the color field vacuum. This minimum disturbance to the vacuum is achieved with the gluon-flux between quark and anti-quark being confined to a tube-like structure called a 'color flux tube.' This allows a quark-antiquark pair to be added to the QCD vacuum with a finite amount of energy. The colorless quark-antiquark combination is a bound state, defined as a meson. According to QCD, the other allowed colorless combination of bound state quarks is a system of three quarks (one of each color), called the baryon. The strong force coupling, the gluon self-interactions, and the underlying minimization of the energy configuration of the QCD vacuum, all work in unison to restrict the formation of any additional bound states; the addition of another colored quark joining the two (three) quark system is not allowed. Thus, in QCD only the observations of colorless mesons or baryons (collectively named hadrons) as the bound states of matter are allowed.

The gluon is said to have an 'anti-screening' effect, compared to the 'screening' effect of QED where the virtual photons can spread out into the vacuum and the force drops, as the Coulomb force, with increasing distance of separation. In the QCD vacuum, bound state quarks need an ever increasing amount of energy to be separated as the distance between the quarks increases. The quarks are effectively bound together by the 'color tubes' of the strong force - it has been shown that these color tubes resist 'delocalization' of the bound state with approximately 10 - 15 tons of color force, regardless of how far apart they are. The lone color charge of a quark in the QCD vacuum is a highly unfavorable configuration, and the QCD vacuum abhors color charge, keeping quarks confined to within spatial distances less than approximately 1 fm.

Having localized the quarks to a bound state, suppose that the separating of these quarks is attempted. As the quarks are separated, the minimum disturbance to the already polarized vacuum will confine the quark-gluon exchanges to the previously mentioned color flux tubes. Continuing to separate the quarks will require an increasingly large amount of energy to exclude the current QCD vacuum polarization and keep the localized vacuum polarized to the quarks' own color field. For the sake of argument, an astute application of an 'outside force' is applied in such a way as to impart sufficient energy to completely separate the quarks. This applied outside force does work on the quarks via momentum transfer, and as enough momentum is imparted on these quarks it can effectively 'break apart' the quarks' bound state. To be more precise, as the quarks recede from each other, the 'delocalization' of the bound quarks continues and the QCD vacuum begins to 'see' the configuration of a 'lone' color charge (quark). This delocalization initiates the polarization of the entire QCD vacuum, and upon increased separation this causes the vacuum fluctuations to grow increasingly violent, exerting an enormous and destructive 'squeezing-

pressure' on the ever stretching color tube. As the color tube stretches, the force between the quarks remains constant while the color tube linearly increases its own potential energy - the color tube remains approximately constant in radius by effectively 'siphoning' the kinetic energy away from the moving quarks and spontaneously creating gluons of the appropriate color. Thereby, the color tube is strengthening and maintaining its color field configuration through spontaneous gluon production, and thus, expelling the increasingly violent QCD vacuum fluctuations that impinge upon the structure of the color tube. Figure 1.8 shows the snapshot of a bound, asymptotically-free hadron system (left) to a system with 'large' separation distance (right) in which the QCD vacuum fluctuations are expelled from the interior region of a meson/baryon [48].

The color tube's continuous production of gluons increases its potential energy up until a critical threshold is crossed. Instead of continuing with the process of expelling the violent QCD fluctuations and preserving the color tube's structure, the dynamical situation crosses over the threshold, into a configuration which is energetically favorable to initiate quark-antiquark production. The color tube 'fragments', facilitating a spontaneous conversion of the color tube's potential energy (stored in the tubes' color field vacuum) into massive quark-antiquark production. The formation of this new set of bound state quarks (hadrons) are each confined by their own individual color tubes, and the violent QCD vacuum fluctuations quickly relax. This fragmentation process makes it impossible to directly probe color fields or work with quarks directly.

1.5 QCD Vacuum and Quark Mass

The measured hadron masses are much heavier than the sum of their constituent quark bare masses. In the case of the proton, its measured mass is approximately

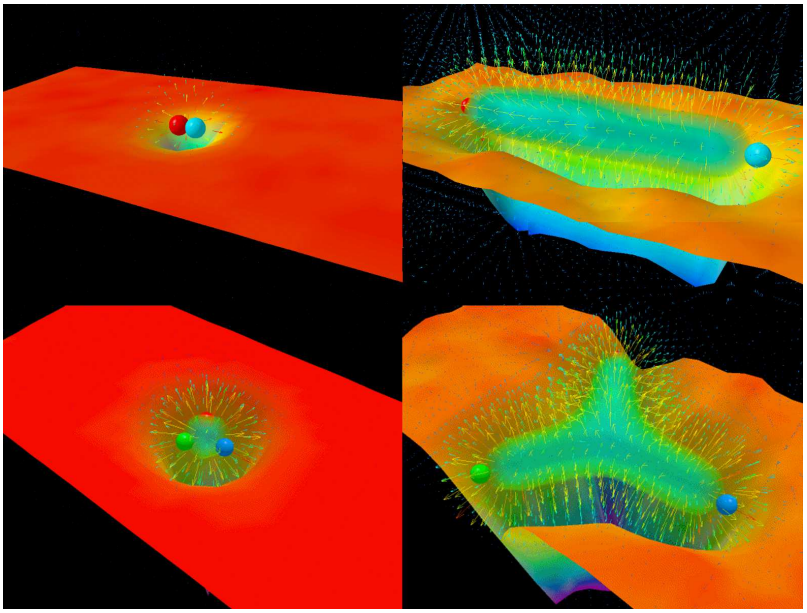

Figure 1.8: The vector field illustrates the gradient of the reduction of the vacuum action density and the emergence of color tubes in QCD [48]. Upper left: Asymptotically-free Meson, Lower left: Asymptotically-free Baryon, Upper right: Separation-stressed Meson, Lower right: Separation-stressed Baryon.

0.98 GeV/c^2, roughly 80 times greater than the sum of the uud quarks bare masses [30]. QCD vacuum fluctuations not only contain the previously discussed gluon-condensate, but they also contain a sea of virtual quark-antiquark pairs, leading to an analogous condensate called the 'quark-condensate.' According to QCD, the quarks are exchanging gluons as well as interacting with the QCD vacuum gluon- and quark-condensates, making the internal dynamics of the protons, and in general, any hadron, quite complicated. However, it is believed that the energy of the quarks and gluons in a region within a proton, in addition to the massive amounts of energy of the quark- and gluon-condensate of the QCD vacuum is what accounts for over 98% of the proton's mass [30]. The QCD vacuum is described as giving the proton's constituent quarks a 'dynamical mass', and the calculations that model the contributions to the

mass of the proton are results from lQCD [30].

1.6 Asymptotic Freedom

The color anti-screening effect that arises from color polarization in the QCD vacuum means that the strong coupling constant between quarks increases as the bound state undergoes separation. Conversely, the strong coupling constant between quarks becomes arbitrarily weak in the limit of short distances, or large energy scales. Mathematically, the behavior is asymptotic, and the reduction in the value of the strong coupling constant in these limits is called 'asymptotic freedom' [54] [38] [36] [53] [37]. Quantitatively, it has been shown that the strong coupling constant goes as the inverse log of distance at a separation of approximately 1 fm. The mathematical form of the 'running coupling constant' for the strong force between two quarks is given by

$$\alpha_s(Q^2) = \frac{-12\pi}{(33 - 2n_f)log(Q^2/\Lambda^2_{QCD})}. \tag{1.5}$$

The expression Q^2 represents the relative momentum between the virtual gluon and probe quark, and n_f is the number of quark flavors with mass less than the energy scale μ and the Λ^2_{QCD} 'scale parameter' that enters through QCD renormalization. At sufficiently low Q^2, the effective coupling becomes large. The parameter Q^2 must be determined by experiment and has a value somewhere in the range of typical hadronic masses, 0.1 to 0.5 GeV. The scale parameter has the form

$$\Lambda^2_{QCD} = \mu^2 exp\left[\frac{-12\pi}{(33 - 2n_f)\alpha_s(\mu^2)}\right]. \tag{1.6}$$

The behavior of $\alpha_s(Q^2)$, for Q^2 values much larger than Λ^2_{QCD}, results in a small coupling and the quarks and gluons interact 'weakly' (asymptotically free), thus a perturbative description of QCD is justified. Near Q^2 values on order of Λ^2_{QCD}, the strength of coupling is large and the interactions between quarks and gluons becomes very 'strong' (confinement) and they tightly bundle themselves, to form hadrons. The physical interpretation of Λ^2_{QCD} may be thought of as defining the boundary between the quasi-free quark and gluon interactions, and the bound states of hadronic matter (e.g. pions, kaons, protons, and so on). Inspection of Eqn. (1.5) reveals a divergence as $Q^2 \to 0$. There is a crucial role in considering the infinities that arise in the limit of $Q^2 \to 0$ and they play an important role in pQCD. The divergent behavior is classified an 'infrared divergence' and further details are beyond the scope of consideration in this thesis.

Summarily - the catharsis of QCD was discovering that the strong coupling constant α_s is actually not a constant, instead α_s is dependent upon the distance between the strongly interacting particles of color; a consequence of color vacuum polarization and the induced color 'anti-screening.' The α_s was labeled as a running coupling constant and the disclosure of its variability led to phenomenon of QCD color anti-screening as the mechanism behind the asymptotic freedom occurring between quarks. The strong force coupling constant becomes arbitrarily weak in the limit of short distances (high-energy), and the calculation methods applied to QCD interactions become analogous to those used in QED, indicating that a perturbative approach to solving the QCD Lagrangian should be effective, and convergent.

1.7 Perturbative Quantum Chromodynamics

Discovering that vacuum color polarization implies an asymptotic freedom for the bound states of quarks finally gave physicists a handle on the non-convergent

behavior of the solutions to the QCD Lagrangian. Asymptotic freedom transitioned QCD to a calculable theory, and has become the seminal approach to strong interactions in the high-energy regime. The theoretical construct of a perturbation theory for QCD at high-energy emerged and is aptly called perturbative QCD (pQCD).

In the case of high-energy experiments, pQCD immediately makes contact with attempts to study the strong interactions. If a quark from one nucleon collides with a quark from another nucleon with sufficient energy, the initial dynamics of the collision will follow the classical description of two-body elastic scattering to first-order. On a short enough time scale, the magnitude of the momentum transfer is much greater than the magnitude of the change in potential energy of the quark as it escapes the nucleon. Under this constraint, high-energy experiments make it possible to make contact with the boundary-specified QCD Lagrangian, provided that the tuning of the experimental initial conditions of the incident particles (colliding beams) are done appropriately. In high-energy collisions, quarks can scatter with a large momentum transverse to the collision-axis while the remaining quarks obtain little transverse momentum. Momentum conservation will result in the hard-scattered quark momentum (high-p_T) becoming observable on the macroscopic- (detector-) level through an event reconstruction using hadrons that are from the associated fragmentation process.

However, from a physical standpoint QCD at high-energy is by definition, insufficient at calculating quark and gluon interactions at low-energy scales. I.e., the QCD Lagrangian is calculated perturbatively in high-momentum transfer interactions (short-distances), but in the low-energy regime where the strong coupling behavior of confinement dominates pQCD breaks down. This break down necessitates alternative methods for solving the QCD Lagrangian at large-distances. The large-distance methods developed are based on numerical techniques on the lattice - 'lattice

QCD' [41].

1.8 Lattice Quantum Chromodynamics

The QCD Lagrangian is solved in the 'low-energy' (quark confinement regime), where the non-linear running coupling constant of the strong force α_s tends to unity, via a method called lattice QCD [41]. Lattice QCD is a non-perturbative approach to QCD, formulated on an array of discretized space-time points, where fields representing quarks are defined only on the sites of the lattice points, and the gluon fields are only defined on the links connecting the neighboring sites. The non-linearity of α_s and the discretization of the QCD Lagrangian results in a mathematically well-defined lattice, suitable for low-energy QCD calculations.

The lattice sets a shortest-distance and time for the interactions and greatly simplifies QCD calculations. Furthermore, the lattice QCD approximation approaches the QCD-continuum as the spacing between lattice sites is allowed to approach zero [67]. However, the smaller the lattice spacing, the more computationally intensive the lattice calculations, leading to an inevitable dependency on millions of variables - requiring the use of supercomputer processing power. Lattice QCD calculations often involve analysis at different lattice spacings to determine the dependence which can then be extrapolated to the continuum. Successful lattice QCD calculations have resulted in proper calculation of the proton mass [30], but they fail to give sensible quark mass results. At the moment, lattice QCD is only applicable in the domain of low density and high temperature. In the region of greatest interest, higher densities, the 'fermion sign problem' renders results from lattice calculations as useless [26] [28] [39] [49] [50].

There is another particularly interesting prediction from lattice QCD calculations. Lattice QCD predicts the existence of a phase transition from normal QCD matter

to a new state of QCD matter, namely the Quark Gluon Plasma (QGP) [61] [62], with newly formed color degrees of freedom. In a QGP, the mesons and baryons lose their identities and dissolve into a liquid of quarks and gluons. In this plasma, the quarks and gluons freely move large distances rather than being confined within the hadrons. This freedom of quarks and gluons is called deconfinement and lattice QCD shows that at high temperature, the confining potential between quarks will diminish due to the effect of Debye color screening, thus liberating the quarks.

1.9 Quark Gluon Plasma

Integrating the broad range of QCD phenomena, it has been noted that the quarks adopt asymptotic freedom, but continually experience confinement from which they can not be isolated. It has also been seen that if the energy conditions are suitably arranged, then the QCD vacuum energy lends itself to the creation of color flux tubes (composed of gluons) that inevitably commence into a cascading process of hadronization. If isolating a quark from this vacuum it is not allowed by nature, then perhaps there exists a modified environment within which the quarks are confined, such that the quarks are deconfined over a volume larger than the volume of a typical nucleus. Theoretical calculations predict the existence of a state of matter at high temperature and/or density, in which this may occur - the Quark Gluon Plasma [61] [62]. Current estimates from lattice QCD predict the transition from the hadron-dominated phase into a deconfined and locally thermalized QGP state at high temperature and small baryon density. Predictions for the formation of a QGP are expected at an energy density of order 1 GeV/fm^3 or, for baryon-symmetric matter, at the temperature $T_c = 165 \pm 10$ MeV [43].

A more physically descriptive picture may be formed by considering the case of increasing the kinetic energy of the real quark interactions with the virtual gluons

and virtual quark-antiquark pairs in the QCD vacuum. These types of interactions will provide the virtual particles with the kinetic energy to induce a phase change, exciting the virtual particles into having enough energy to become real particles. This is the condition where the QCD vacuum is regarded as having melted. Recalling that the QCD vacuum is composed of gluon- and quark-condensates, naturally it could be expected that there are two independent phase changes - the melting of the gluon-condensate and the melting of the quark-condensate. Lattice QCD calculations predict these phase changes to occur at the same point, but debate continues. As the gluon-condensate melts, there will no longer exist a color neutral vacuum to confine gluon exchanges between quarks to the color tubes and the color anti-screening with distance will cease (see Figure 1.4), and the quarks will no longer experience the confinement of the strong force. As the quark-condensate melts, the real quarks will no longer acquire dynamical-mass from moving through the vacuum, and the quark masses will reduce to their bare masses. At the QGP phase transition, hadronic matter ceases to exist and the quarks and gluons act like free particles over a larger than nucleus-type volume.

The phase transition at zero net baryon density is expected to not be a true discontinuous one, but rather a rapid crossover, becoming a first-order transition at a critical point [64]. The theoretical calculations have however still large uncertainties and the exact location of the critical point and even the order of the phase transition expected to happen are far from certain. This uncertainty facilitates the need of experimental measurements to better clarify the theoretical models. The Relativistic Heavy Ion Collider (RHIC) at Brookhaven National Laboratory (BNL) has a physics program that includes creating a QGP in the laboratory through the high-energy, heavy-ion collisions.

1.10 Heavy Quarkonia

The use of heavy quarkonia, i.e. bound systems of charm-anticharm (charmonium) and bottom-antibottom (bottomonium) quark pairs can be used as probes [56] [31] for studying the medium (possibly a QGP) produced at RHIC, at the partonic level. Figure 1.9 and Figure 1.10 show the spin-parity of the charmonium and bottomonium resonant states, respectively.

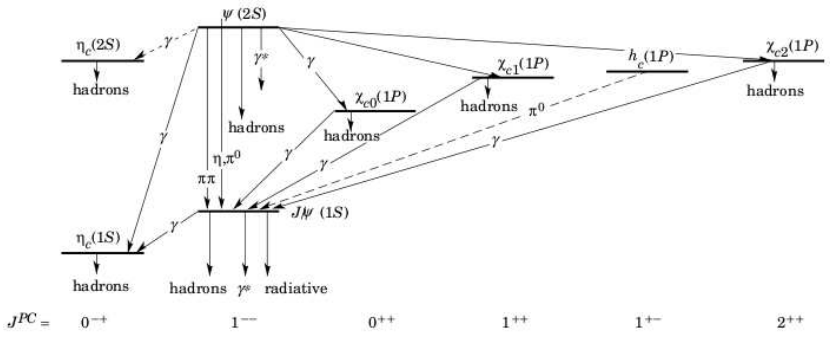

Figure 1.9: The charmonium system and the allowed decay transitions.

There are several reasons that heavy quarkonia can be validated as sufficient and feasible probes for studying this possible QGP: 1) the (relatively) substantial bare-masses of the charm (1.15 to 1.35 GeV) and bottom (4.1 to 4.4 GeV) quarks allows for perturbative calculations of heavy quark production. These production-timescales occur 'fast enough' ($\tau \propto 1/m_Q$) to be sensitive to the early conditions (pre-QGP formation) created by the heavy-ion collision, 2) the wave-functions describing heavy quarkonium states predict spatial sizes (of the quarkonia) that are much smaller than the intrinsic hadronic scale, $1/\Lambda_{QCD}$, in direct contrast to the sizes of 'light' hadrons

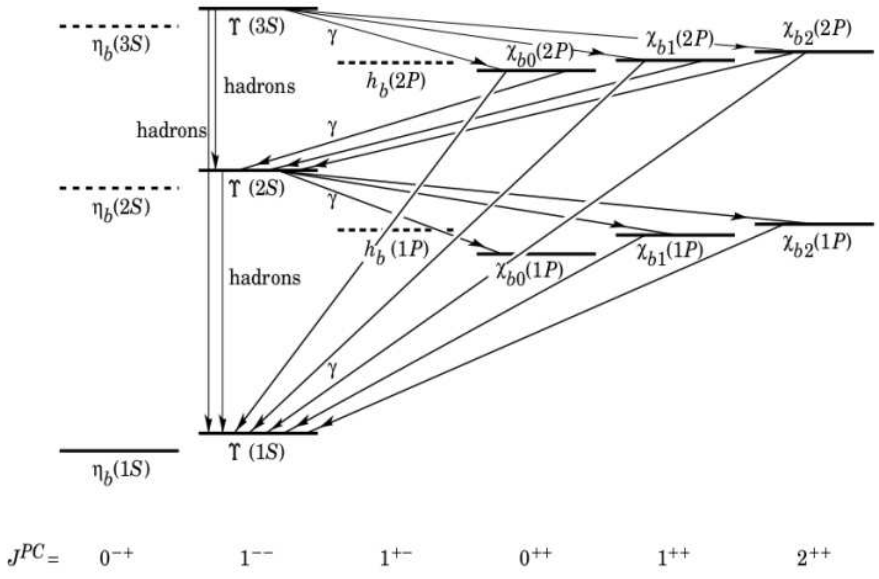

Figure 1.10: The bottomonium system and the allowed decay transitions.

containing (u, d, s) quarks, and 3) the electromagnetic decays of heavy quarkonium states proceed at timescales which are much greater than the lifetime of the medium, hence the decay daughters (di-leptons) are not influenced by the (colored) medium - making quarkonium production cross-sections at STAR experimentally accessible.

The standard assumption in modeling quarkonia production is that they can only be produced in low-multiplicity hard-scattering processes, thus any observed suppression pattern results from the interactions between the quarkonium state and the medium created in the collisions. Alternative models not based on this assumption do exist, where modeling of the quarkonium production occurs at hadronization, but no direct access to information about the early stages of the collision is discernible.

1.11 Production Mechanism of Heavy Quarkonia

The systematics of prompt production of heavy quarkonium is not fully described by current models, e.g. the Color Singlet Model (CSM) and the Color Octet Model (COM). Figure 1.11 shows an Υ produced with the single hard-gluon emission expected in CSM production vs. the multiple soft-gluon emissions expected in COM production. The production mechanism of J/ψ and Υ was assumed to take place via

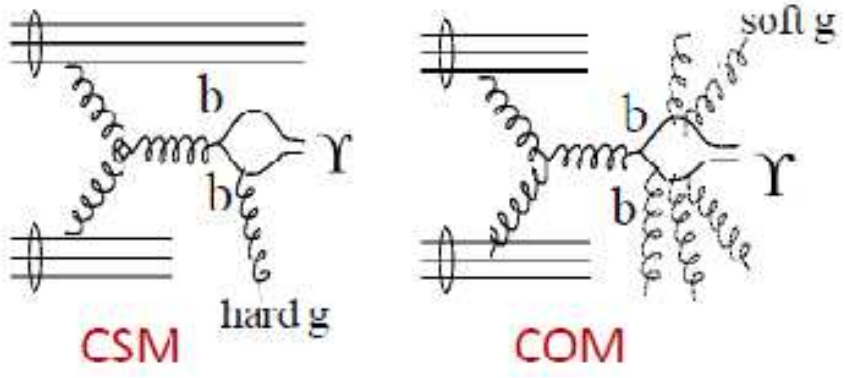

Figure 1.11: CSM vs. COM gluon radiation.

the leading order CSM processes, but in 1997, CDF studies showed large excesses in the amount of prompt quarkonia produced with respect to theoretical predictions. Historically the calculations grossly under-predicted the production cross-section, but later developments/refinements with higher-order corrections [47] have better described the results from data. Another popular approach to production mechanisms is Non-Relativistic QCD, where production at the parton level can also take place via a color octet quark pair. The COM is quite successful in explaining the p_T-spectra of quarkonia. However, polarization predictions disagreed with experimental

data [3] - the production via a color octet state predicted a significant transverse polarization of J/ψ and Υ, but Tevatron data contradicted these predictions.

The STAR program has the capabilities for reconstructing the heavy quarkonium states of both the J/ψ and Υ particles produced by the collisions at the Relativistic Heavy Ion Collider (RHIC), promoting production-based analyses in STAR. The measurement with Cu+Cu collisions at STAR and the observation of a lack of expected [52] suppression in high-p_T J/ψ R_{AA} [2]. The lack of J/ψ suppression at high-p_T suggests that J/ψ cannot exist in a colored state on a long enough timescale to be affected by the medium, and ultimately leads to an interpretation that the production of J/ψ is possibly not dominated via a color (octet) channel [2] - possibly, the primordial J/ψ is produced as color singlet state, traversing unaffected through the (colored) medium produced at RHIC. However, it is the only hadron exhibiting this behavior in RHIC heavy-ion collisions. While quarkonium production in the hadronic collisions at RHIC energy is dominated by direct production via gluon fusion followed by CSM and/or COM transitions [20], quarkonia production is not yet fully understood. In fact, current models, e.g. the CSM and the COM each have their inherent deficiencies in describing the data; it is known that the CSM and COM framework does not simultaneously describe the cross-section, p_T-spectra, and spin-alignment measurements seen in data [3] [5] [6] [4] [1].

1.11.1 Color Singlet Model

One of the earliest and most successful proposals for explaining heavy quarkonium production following the 1974 discovery of the J/ψ meson, was the construction of the Color Singlet Model (CSM) [14] [9]. In the CSM scenario the formation of quarkonium (e.g. J/ψ and Υ) is constructed as a two step process: 1) the creation of two on-mass-shell heavy quarks; 2) the binding of these two heavy quarks into

mesonic states. In the first step, the inelastic partonic scattering induces the creation of charm (or bottom) quarks with a bare-mass much larger than the QCD scale Λ_{QCD} and the cross-section is computed in pQCD. In principle, the cross-section is calculable to any desired order in α_s and generally dependent on the specific collision process - center-of-mass energy ($\sqrt{s}$) and other kinematic variables like transverse momentum (p_T) [60]. In the second step, the $q\overline{q}$ pair exists in a J^{PC} state, in the color-singlet configuration. Since the heavy quarks ($c\overline{c}$ or $b\overline{b}$) are at rest in the meson's frame and because spin and color of the heavy quark pair does not change during the process of binding, the full-evolution of the $q\overline{q}$ pair must retain its initial color-singlet state and result in a bound quarkonium (J/ψ and Υ) with the same J^{PC} state and color-singlet configuration. In high-energy collisions (e.g. RHIC energies), the leading contribution to quarkonium production comes from the gluon-gluon fusion process: $gg \rightarrow {}^3S_1g$ [55], where the standard spectroscopic notation for the radial and angular momentum quantum numbers denotes the state of the $q\overline{q}$ pair and g represents a gluon (see Figure 1.11).

Initially, the CSM calculations compared well to measurements from various high-energy experiments. The CSM successfully calculated observables for heavy quarkonium production over a wide spectrum of processes, including J/ψ photo- and hadron-production, Z decays, and b-hadron decay [14] [9] [10] [12] [22] [45] [29]. However, in the early 1990's, nearly two decades after the discovery of J/ψ, the development of accelerator-colliders with increased collision-energies led to an accumulation of experimental (and theoretical) evidence that was symptomatic of an incomplete model/framework - leading-order (LO) α_s^3 CSM was failing in its predictions of the observed production rates for charmonium (and bottomonium). Inclusive J/ψ, ψ' and χ_c cross-section measurements from CERN (UA1 experiment) and the Tevatron (CDF experiment) uncovered discrepancies between data and the CSM predictions.

However, the CSM was afforded a way to mitigate these apparent discrepancies seen in data by endowing a substantial B-meson contribution to the inclusive charmonium states, thus making B-meson feed-down decay a dominate source of J/ψ production at these high center-of-mass energies. The CDF experiment suffered from a lack of sensitivity to measure these B-meson feed-down contributions and the CSM was able to temporarily sidestep the initial non-conformity to data. In turn, the CDF experiment subsequently addressed its lack of B-meson feed-down sensitivity[4], subjecting the CSM to more rigorous tests via the measurements on B-meson feed-down contributions. The CDF experiment was able to differentiate between charmonium states coming from B-meson feed-down decays and charmonium states which were coming directly from prompt charmonium production. The CDF experiment presented their results in the form of a cross-section measurement on direct ψ' production - reporting that only 23% of the measured ψ' were from the B-meson feed-down decays [23]. The predictions from CSM underestimated measurements of prompt, high-p_T ψ' (p_T $>\sim$ 4.0 GeV) production by orders of magnitude, yielding rates approximately 50 times lower than the CDF measurements [11]. Additionally, the CDF experiment isolated the χ_c radiative cascade contributions to ψ' production, finding the 32% of the prompt ψ' observed were daughters of χ_c radiative decay, and again at odds with predictions of the CSM [23] [11].

The recurring lack of consistency between LO CSM predictions and experimental observations led to a consensus that higher-order α_s processes (next-to-leading-order, α_s^4) in gluon and heavy quark fragmentation had to be taken into account - dethroning initial beliefs that such processes did not play a large role in heavy quarkonia production. These newly-tuned CSM calculations, incorporating the processes of gluon and heavy quark fragmentations, now predicted the higher cross-sections desired and

[4]CDF installed a silicon micro-vertex detector in the 1992-1993 runs.

more closely conformed with the J/ψ and ψ' results in data. In fact, the high-p_T contributions from fragmentation processes have a much harder shape ($1/p_T^4$ vs. $1/p_T^8$) and the CSM predictions approached prompt J/ψ cross-section measurements to the extent that the discrepancy was absorbed by experimental and theoretical uncertainties. However, as was done for the ψ' measurement, the CDF collaboration isolated and removed the feed-down from radiative χ_c decay, leaving a stand-alone measurement on the prompt J/ψ cross-section; whereupon the CSM was again ruled insufficient for under-predicting the J/ψ cross-section by a factor of 30. The most recent results coming from CSM calculations make use of even higher-order processes (next-to-next-to-leading-order, α_s^5) are currently available [47]. These NNLO CSM calculations more accurately describe the observed Υ spin-alignment distribution seen in Tevatron (CDF [3] and D0 [1]) measurements, but these NNLO CSM calculations are consistent with RHIC measurements of J/ψ low-p_T spectra - however, the observed shape of high-p_T J/ψ seen at the Tevatron experiment deviates from CSM calculations up to NNLO.

In summation, the ongoing discrepancies between the predictions from the Color Singlet Model and the experimental measurements leads to two noteworthy theoretical developments in the understanding of the physics of heavy quarkonium production. The first realization came in the form of the discovery that heavy quarkonium at large transverse momentum is produced primarily by a hard scattering and the fragmentation process at high-p_T. The second development was that even with the higher-order α_s processes in gluon and heavy quark fragmentation accounted for, there is still something missing from the viewpoint of theoretical production. The need for new perspective on heavy quarkonia production led to the construction and first publication of a Velocity Scaling Model (VSM) in 1992 - more often referred to as the Color Octet Model (COM), in which the COM was applied to P-wave decays

[19]. The COM P-wave formalism was then extended to a treatment on the production in B-meson decays [21]. In short, the COM is a non-relativistic QCD (NRQCD) treatment, in which the color-octet mechanism governing the $q\overline{q}$ pair is produced at short distances in a color-octet state, sometimes dominating the production in heavy quarkonia. The Color Octet Model will be discussed in more detail in the next section.

1.11.2 Color Octet Model

The Velocity Scaling Model (VSM), also referred to as the Color Octet Model (COM), is constructed within the effective field theory framework of Non-Relativistic QCD (NRQCD). The schema of NRQCD COM relies on the assumption of very massive quarks - enabling calculations of inclusive heavy quarkonium production cross-sections, based on systematic expansions in both the strong coupling constant (α_s) and bound state quark velocity (v). The partonic quarkonium production cross-section of the quarkonium state is a sum of the products of short-distance coefficients and NRQCD matrix elements.

The COM description of the production (and decay) of heavy quarkonia is attributed as arising from both color-singlet and color-octet initial states. According to the COM production cross-section rates are partitioned into 1) the short-distance scale factors associated with annihilation and production, set by the heavy quark mass (M) and 2) the long-distance scale factors associated with the structure of heavy quarkonium, set by Mv and Mv^2, where v represents the relative velocity of the heavy quarks within the quarkonium. The short-distance coefficients are the process dependent partonic cross-sections for making $q\overline{q}$ pairs, which are computed via pQCD. According to the COM, the color-octet mechanism produces the $q\overline{q}$ pair

at short-distances (in a color-octet state) by either gluon fragmentation or direct parton reactions, and are in principle, allowed to dominate the $q\overline{q}$ pair production. The long-distance matrix elements represent the probability for the $q\overline{q}$ pair to evolve into a color-singlet bound state, and are non-perturbative parameters. Each matrix element is expanded in powers of the heavy quark velocity according to the velocity scaling rules, and only the most dominant terms are kept [21] [19] [20].

Contrary to the basic assumption of the CSM, the $q\overline{q}$ pair that is produced in the color-octet state is allowed to transition into the final color-singlet bound state of quarkonium. However, the transition from color-octet state (charmonium or bottomonium) is followed by single or multiple long wavelength (soft) gluon emissions (color-neutralization), which takes place at space-time coordinates far removed from the collision point (see Figure 1.11). The COM formalism provides a very natural way to accommodate relativistic corrections to leading order estimates. With the arrival of the VSM, quarkonium calculations were placed on a more solid theoretical foundation.

1.12 Motivation and Observables

The basic processes underlying quarkonium production at RHIC includes direct production via gluon fusion and 'color-octet' and 'color-singlet' transitions [20]. The interpretation of 'Υ suppression' observed by the SPS and RHIC experiments requires an understanding of these quarkonium production mechanism in hadronic collisions. As previously mentioned, STAR data (Cu+Cu) of J/ψ at high-p_T showed a lack of suppression , possibly indicating that J/ψ cannot exist in a colored state on a long enough timescale to be affected by the medium produced in RHIC collisions. It has been conjectured that this lack of J/ψ suppression at high-p_T indicates that a non-color production mechanism dominates primordial J/ψ production .

One analysis technique for studying the production mechanism of heavy quarkonia is to investigate the Spin-alignment ('polarization') of heavy quarkonia. In the CSM framework, no strong correlation between the initial gluon polarization and final state observation is expected from CSM calculations, and therefore a value of $\alpha = 0$ is expected for the polarization in data. In the COM framework, the production of octet ('colored state') quarkonia inherits the transverse polarization, ($\alpha = +1$), from the gluon. Comparison of the $\cos(\theta)$ angular distribution, to the predicted shapes from COM and the CSM could lend insight into the heavy quarkonia production mechanism. Figure 1.12 shows the scenario for a measurement of the two-body Υ decay (left panel), and theoretically expected $\cos(\theta)$ distributions with corresponding α values (right panel).

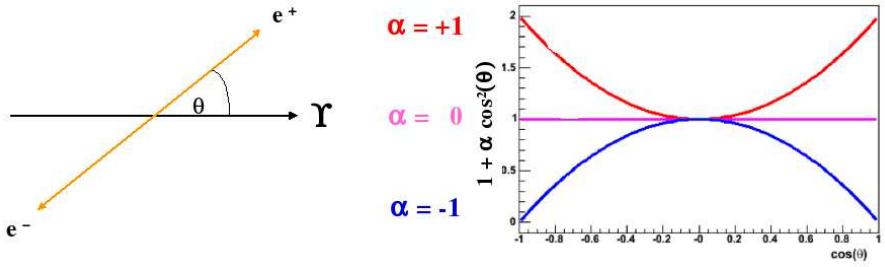

Figure 1.12: two-body $\Upsilon \to e^+e^-$: decay topology (left panel) and $\cos(\theta)$ distributions (right panel).

The STAR experiment is also looking for new ways to study the prompt production mechanism of heavy quarkonium, and the approach taken here is the Upsilon + Hadron azimuthal correlations. This type of correlation analysis will search for the presence of hadronic activity directly around the heavy quarkonium - a feature that

has been suggested as an experimental observable to indirectly measure the gluon radiation emitted off the colored heavy quark pair during production [44]. The CSM predicts the emission of a single 'hard' gluon in association with Υ production, while the COM predicts the emission of multiple 'soft' gluons in association with Υ production. Figure 1.13 shows a heuristic depiction of COM-induced Υ production in tandem with soft-gluon radiation, and the eventual associated near-side hadronization. Insight into the prompt production mechanism of heavy quarkonium can be obtained from this measured hadronic activity (or lack thereof).

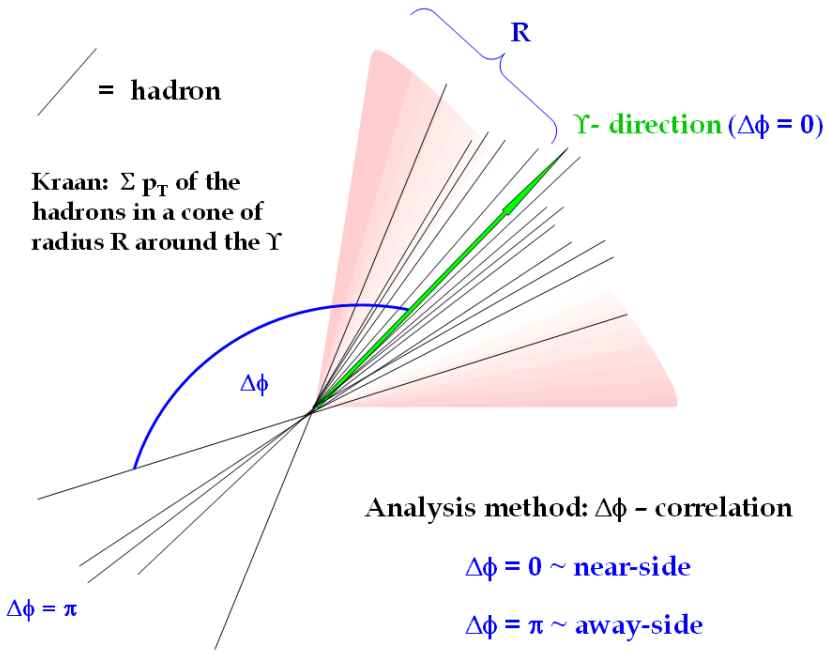

Figure 1.13: COM soft-gluon radiation: Υ near-side hadronic activity.

The STAR experiment is capable of achieving a high signal-to-background ratio

(S/B) in Υ reconstruction. This enables the pursuit of the aforementioned measurements of the heavy quarkonium production-related observables: 1) Upsilon Spin-alignment ('polarization'); 2) Upsilon + Hadron azimuthal correlations. The centerpiece of the analysis presented is framed by these two measured observables, and is performed with STAR d+Au and p+p collision data sets, each taken at $\sqrt{s} = 200$ GeV.

2. EXPERIMENTAL APPARATUS

2.1 RHIC Accelerator Complex

The Relativistic Heavy Ion Collider (RHIC) complex is located at Brookhaven National Laboratory (BNL) on Long Island, New York. RHIC became operational in 2000, after 10 years of development and construction. The facility was the first to collide heavy-ion beams, reaching and sustaining a peak center-of-mass collision energy of 200 GeV per nucleon pair (approximately 10 times greater than any previous fixed-target nuclear experiment). The objective of the RHIC complex is three-fold: 1) accelerate and collide heavy ions 2) accelerate and collide protons 3) accelerate and collide polarized protons. Figure 2.1 shows the RHIC Accelerator Complex positioned at BNL, as seen from a satellite photo.

Figure 2.1: Satellite view of the RHIC complex at BNL (small circle, inset yellow box), on Long Island, New York.

The RHIC component of the complex consists of a two-ring, quasi-circular particle accelerator which measures 3.8 km (2.4 miles) in circumference. The rings house six independent intersection points which can guide the particle beams to collision

at energies up to $\sqrt{s_{NN}}$ = 200 GeV for Au+Au and $\sqrt{s_{NN}}$ = 500 GeV for p+p. The RHIC accelerator is designed to pursue two major physics programs: 1) create a Quark-Gluon Plasma (QGP) using heavy-ion collisions and 2) untangle the source of the spin of the proton using polarized proton collisions, at high luminosity and variable center-of-mass energies. The cross-section for heavy-flavor production depends strongly on the collision energy [65]; RHIC has ample capability to create heavy-ion collisions at an energy of $\sqrt{s_{NN}} = 200$ GeV, achieving not only production of multiple charm quarks in each collision, but also extending RHIC's reach into the sector of bottom quark production.

Figure 2.2 shows a schematic diagram of the RHIC accelerator complex. The individual facilities produce the heavy-ions and protons, execute the acceleration phase, and handle beam storage before their entrance into the RHIC colliding ring (where the final energy-ramping and steering towards beam-beam collisions is achieved). The RHIC accelerator complex [40] maintains and operates a Tandem Van de Graaff facility, a Linear Proton Accelerator, a Booster Synchrotron ring, an Alternating Gradient Synchrotron (AGS), and the RHIC.

Figure 2.3 shows the facilities which are directly responsible for the production of ions/protons, and their acceleration and collision. The procedures for creating the particles to accelerate and collide is dictated by the desired beam-type (heavy ions, protons or polarized protons). The use of heavy-ions as collision systems, e.g. Au+Au, begins with Au ions emerging from the Tandem Van de Graaff accelerator in a charged state of +1. The Au ions emerge from a pulsed sputter ion-source at the Tandem Van de Graaff, where they are partially stripped of their electrons with a stripping-foil, where the Tandem's high voltage terminal accelerates them to an energy of 1 MeV/nucleon. As the Au ions exit the Tandem Van de Graaff they undergo additional stripping, bringing the Au ions to a charge state of +32. Next,

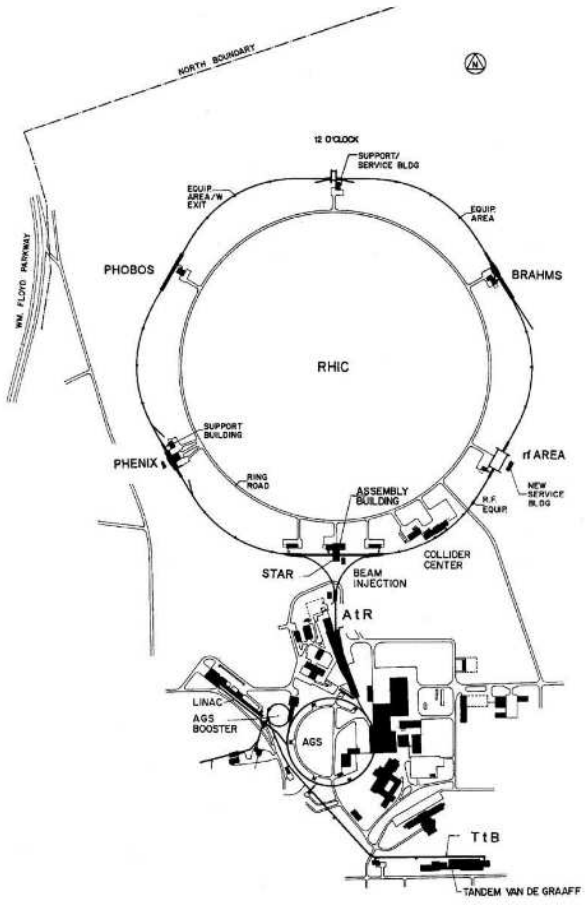

Figure 2.2: Schematic diagram of the RHIC accelerator complex - The STAR experiment is located at the 6 o'clock position along the RHIC ring.

bending magnets are used to select and guide the +32 charged ions to the Booster Synchrotron, where the Au ions are accelerated to an energy of 95 MeV/nucleon. After acceleration in the Booster, the Au ions exiting the Booster are stripped again, to a charged state of +77 before injection into the AGS for acceleration up to an energy of 10.8 GeV/nucleon - the RHIC injection energy. Immediately before the Au ion bunches exit the AGS, they undergo one final stripping to a charged state of +79. The final step is entrance into an AGS-to-RHIC Beam Transfer Line, where

the Au ion bunches are injected into the RHIC tunnel for final energy-ramping and steering towards collision. The RHIC proton-proton is more straight-forward: linearly accelerated protons make their transition from the 200 MeV Linac line via an injection into the Booster, where they are further accelerated in the AGS ring. After AGS acceleration, the protons are injected into RHIC ring for the final stage of energy-ramping before collision.

Initially, the RHIC program came online with the commissioning of four different detector programs, each conceived to provide independent and complementary measurements. The two large experiments are called STAR and PHENIX (located at 6 o'clock and 8 o'clock, respectively), and the two small experiments that are currently non-operational, called PHOBOS and BRAHMS (formerly located at 10 o'clock and 12 o'clock, respectively). The RHIC complex has run beam-beam collision systems with p+p, d+Au, Cu+Cu and Au+Au configurations. There are plans[1] to collide Uranium-Uranium (U+U) systems.

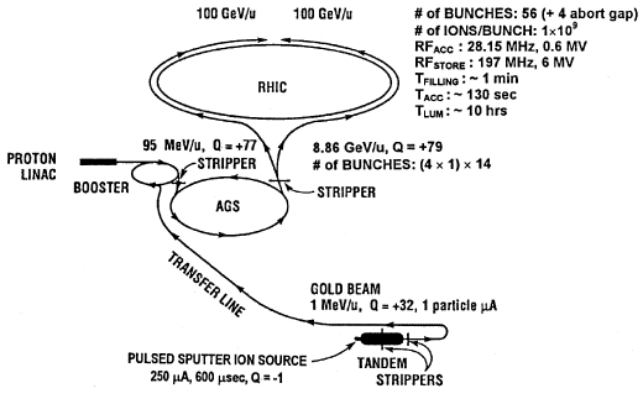

Figure 2.3: Schematic diagram of the Linac and RHIC acceleration stages.

[1]RHIC Beam Use Requests for Run-12 and Run-13

2.2 STAR Detector

This thesis is concerned with the experimental methods and data collected by the STAR (Solenoid Tracker At RHIC) program. The STAR detector records outward-moving hadrons and leptons produced during the intense RHIC collisions over a large phase space. The significant geometrical acceptance of the STAR detector is ideally suited to measure the rare (low production cross-section) and wide opening-angle decays of heavy-flavor vector mesons. The specifications of detector sub-systems are described in the next section. The two largest sub-detector components in STAR are the Time Projection Chamber (TPC) [7], used for charged-particle tracking, and the Barrel Electro-Magnetic Calorimeter (BEMC) [13], used for energy-deposition-related measurements. These two core-detector components enclose a significant geometrical volume: full-azimuthal ($0 \leq \phi \leq 2\pi$) with substantial central-rapidity (η-coordinate in STAR geometry) acceptances. Figure 2.4 shows a composite drawing of the STAR detector.

It is useful to differentiate between rapidity and pseudo-rapidity. The rapidity is given by the equation:

$$y = -\frac{1}{2} \ln \left(\frac{E + p_L}{E - p_L} \right) \tag{2.1}$$

where E represents the energy of the particle, and p_L represents the longitudinal momentum of the particle parallel to the beam line ($\pm$z-axis in STAR geometry). High-energy collisions generally result in a produced particle's mass (M) being small relative to its total momentum ($\vec{p}$), and for all intents and purposes a mass that is *a priori* unknown. Frequently, an approximation that $y \simeq \eta$, where η is called the pseudo-rapidity (like rapidity, also boost-invariant along the beam-axis), and is given by the expression:

$$\eta = -\ln \left[\tan \left(\frac{\theta}{2} \right) \right] \tag{2.2}$$

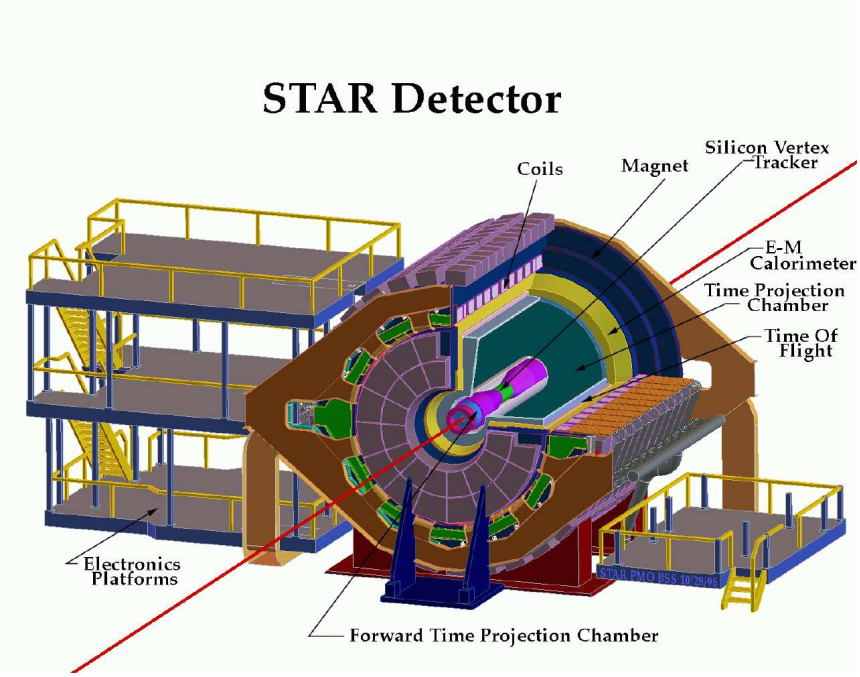

Figure 2.4: The central line through the STAR detector denotes the collision beam-axis.

where θ represents the angle between the particle trajectory and the beam-axis. In the limit $|\vec{p}_{particle}| \gg \mathrm{M}_{particle}$, the pseudo-rapidity ($\eta$) is equivalent to the rapidity (y).

The combined geometrical coverage and high readout performances achieved by the TPC and BEMC during data collection are necessary but not sufficient to perform physics-level analyses at RHIC's peak collision rates and energies. Further integration of these two core-detector systems into a larger, multi-detector platform is required in order to attain the overall tracking and calorimetry objectives of the STAR program. The cornerstone for all of STAR's tracking at central-rapidity acceptance is the STAR magnet. General discussions of STAR tracking and STAR calorimetry that focus on the detectors relevant to this the thesis (TPC and BEMC) will follow.

2.2.1 STAR Magnet

The STAR Solenoidal Magnet [15] is a cylindrical design with length L = 6.85 meters and inner- and outer-diameters of D_{inner} = 5.27 meters and D_{outer} = 7.32 meters, respectively. The STAR magnet is capable of generating a maximum magnetic field-strength (Full-field) along the length of the cylinder (±z-axis in STAR geometry) of $|B_z|$ = 0.5 T. The STAR magnet further retains the ability to exercise 'variable-polarity', thus allowing for multiple data-taking field-configurations: full-field, reversed full-field and half-field. Immersion of the STAR detector into this magnetic field is the underpinning for which all of STAR's tracking system(s) capabilities rest (at central-rapidity acceptance) - for example, measurements of three-dimensional helical trajectories and associated properties, as well as charge-separation. Figure 2.5 depicts the STAR magnet (left) and its circumplacement over the STAR Time Projection Chamber (right).

2.2.2 STAR Tracking, Time Projection Chamber

The available STAR tracking detectors: The Time Projection Chamber (TPC) [7] for 'general-purpose' charged-particle tracking, and the Silicon Vertex Tracker (SVT) and Silicon Strip Detector (SSD) - both facilitating charged-particle tracking closer to the STAR[2] interaction region. At more forward geometry, the Forward Time Projection Chambers (FTPC) allow for charged-particle tracking in more forward-rapidity regions.

The TPC is a cylindrical-geometry chamber, partitioned by a central membrane held at a high voltage - setting up an axial E-field parallel to the axial B-field established by the STAR magnet. The inner- and outer-field cages are divided up into rings that are individually maintained at voltage settings to insure uniformity

[2]The SVT and SSD were removed after Run-7.

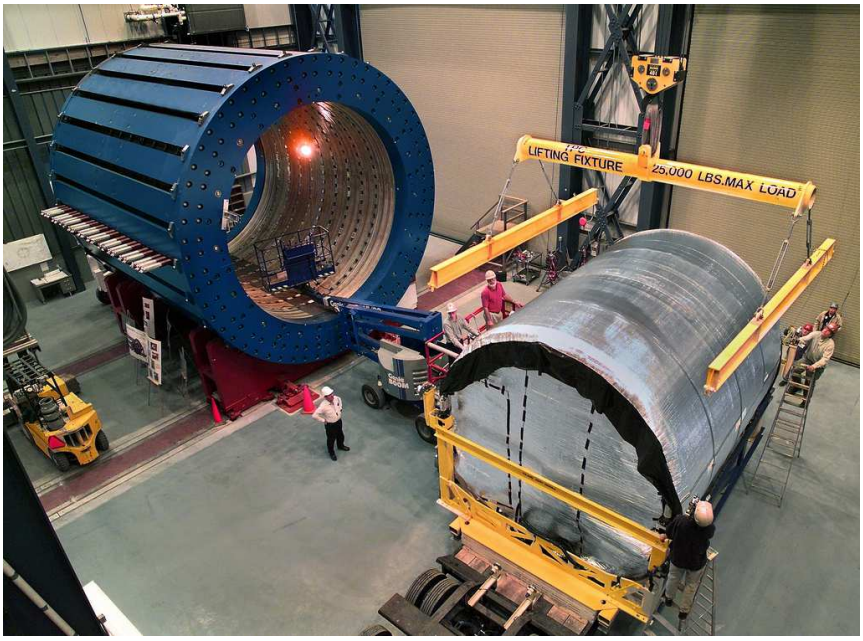

Figure 2.5: The STAR Magnet (left) prior to insertion of the TPC (right).

in the E-field from central membrane (z = 0) to endcap positions. Figure 2.6 shows a schematic representation of the STAR TPC.

The TPC chamber is a gas-filled chamber (admixture of 90% Argon and 10% Methane Gas), held at 2 mbar above atmospheric pressure. The immersion of the TPC into the strong magnetic field yields track measurements that are left by the charged particles ionizing the gas-filled chamber as they traverse outwards from the collision. The known 'drift velocities' of these ionized particles moving through the gaseous mixture in the applied E-field allows for proper three-dimensional TPC track reconstruction. Once these drifting ions reach the endcap-boundaries of the TPC, they are collected by sectors of highly-pixilated 'pads.' The 'patchwork' of pad-elements is designed with two principles in mind: 1) good resolution on the inner-sector (13 pad-rows) for vertex finding, and 2) fine resolution on the outer-sector (32

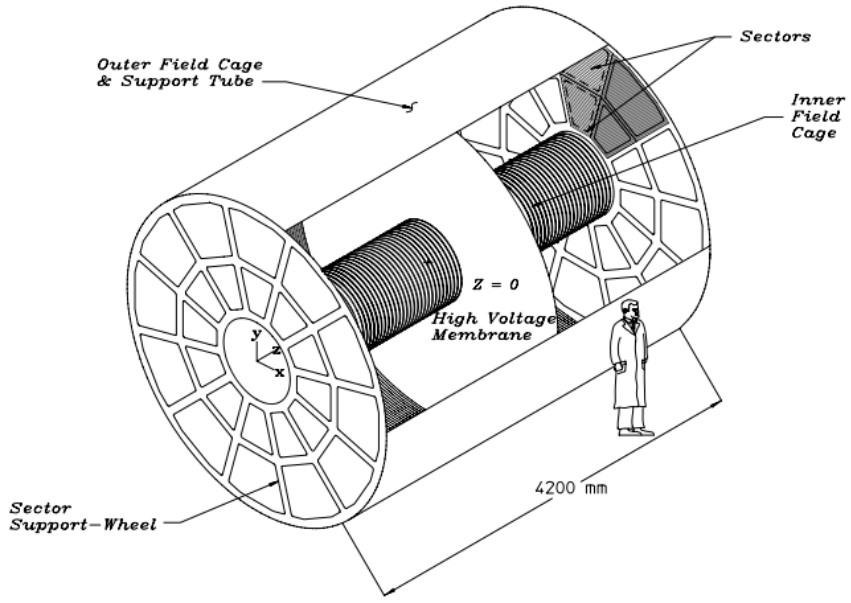

Figure 2.6: Schematic diagram of the STAR TPC.

pad-rows) for maximal dE/dx resolution. Figure 2.7 shows the TPC readout system - the endcaps are partitioned into 12 sectors (TPC sectors).

Post-reconstruction of the TPC tracks opens access to track momentum, track charge, and track energy-losses (e.g. particle identification via dE/dx) - essential to event reconstruction/analysis. The TPC also aides in locating the primary vertices from initial production, as well as secondary vertices arising from cascading decay-chains.

2.2.3 STAR Calorimetry, Barrel Electro-Magnetic Calorimeter

The STAR electro-magnetic calorimetry consists of three main detectors. The Barrel Electro-Magnetic Calorimeter (BEMC), the Endcap Electro-Magnetic Calorimeter (EEMC), and the Forward Meson Spectrometer (FMS). These provide photon

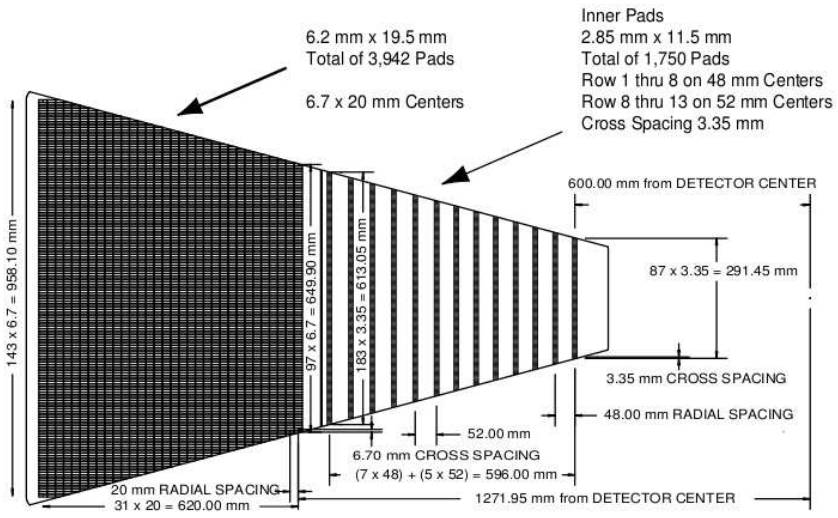

Figure 2.7: TPC sector pad.

identification, electron identification (where tracking is available), as well as extending the reach of measurements into hadron decay channels that cascade through electromagnetic processes. The BEMC has a pseudo-rapidity coverage of $|\eta| \leq 1$ and $0 \leq \phi \leq 2\pi$ in azimuth, matching the acceptance of TPC tracking, while the EEMC has pseudo-rapidity coverage of $1 < \eta \leq 2$ and $0 \leq \phi \leq 2\pi$ in azimuth. The FMS provides full azimuthal coverage for rapidities $2.5 < \eta < 4$. The BEMC (and EEMC) design incorporates independent read-out capabilities embedded within each of the 4800 barrel calorimeter towers (and 720 endcap calorimeter towers for each endcap) - specifically, the Shower Maximum Detectors (SMD) and the Preshower (PRS) subdetectors. The SMD and PRS detectors independently exist for the barrel (BSMD) and (BPRS) and for the endcap (ESMD) and (EPRS). The SMD and PRS detectors provide a measurement of the shower's profile (additional to calorimeter energy measurements), and additional electron selection (hadron-rejection) capabilities, respectively.

The position of the BEMC is inside the STAR solenoid between the TPC and the magnet coils, with the inner-surface of the BEMC running parallel to the beam axis and has a radius of about 220 cm. The 4800 calorimeter towers are segmented into 120 modules, running from the West-end to the East-end of the STAR detector. Each of the 120 calorimeter modules subtends 6° in $\Delta\phi$ ($\approx$ 1 radian) and 1.0 unit in $\Delta\eta$. These modules are mounted 60 in ϕ and 2 in η. Each of the modules is approximately 26 cm wide and 293 cm in length, with 23.5 cm of 'active-depth' and an additional $\approx$ 6.6 cm in structural plating ($\approx$ 1.9 cm of the plating is located on the front of each module). Each of the 120 calorimeter modules are further segmented into groupings of 40 towers (2 in ϕ and 20 in η), with each individual tower subtending 0.05 in $\Delta\phi$ by 0.05 in $\Delta\eta$. Figure 2.8 shows a side-cross-section view of a BEMC module, running along the $+\eta$-coordinate (+z-axis) in STAR geometry, displaying each projective tower pointing towards the center of the STAR TPC (the location of the interaction region).

2.2.3.1 Alternating Pb-Scintillator Sampling Calorimeter

The BEMC system is a 4800-count, sampling calorimeter that uses Pb and scintillating plastic towers to construct the large cylindrical surface area. Figure 2.9 shows a schematic side-view of a single tower with the mounting system and the compression-plate components. The essential operational element of each BEMC tower consists of a stacked Pb-scintillator configuration, with sub-detector units embedded within each tower, called the Shower Maximum Detector (SMD), which are situated approximately 5.6 radiation lengths from the front of the stack. The SMD will be discussed in more detail in Subsection 2.2.3.2. The total Pb-scintillator layering is discretized and quantified in the following way: there are 20 layers of 5 mm thick Pb, 19 layers of 5 mm thick scintillator and 2 layers of 6 mm thick scintilla-

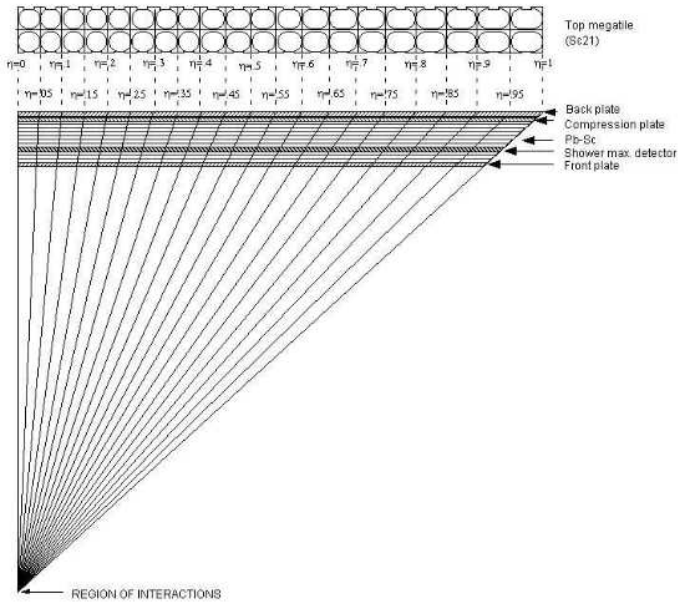

Figure 2.8: A schematic diagram of a BEMC module in STAR clearly shows the η-projective design of the towers.

tor. Each BEMC tower has a total depth of $\approx$ 20 radiation lengths (20 X_0) at η = 0. The 2 thicker scintillator layers are the defining elements of the sub-detector, called the preshower detector, conceived to help with both π^0/γ and electron/hadron discrimination.

The physical quantity measured by the BEMC is the energy deposited by a particle into the calorimeter. Each BEMC tower has a total depth of $\approx$ 20 radiation lengths (20 X_0) at $\eta = 0$, and any given tower has an energy resolution of $\sigma E/E \approx 1.5\% + 14\%/\sqrt{E}$ [13]. However, even though hadronic interactions within a calorimeter tower (contributing a contaminant background energy) can decrease the effective resolution, the energy deposits can be used to 'trigger' (select) electromagnetic-type events (see Section **??**). Together, the information from the TPC and BEMC allows for complementary matching of the track information to energy depositions for addi-

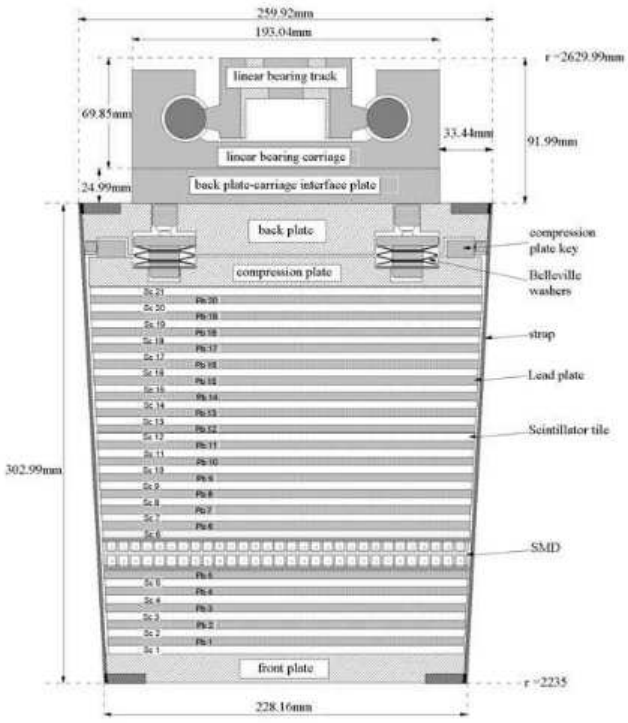

Figure 2.9: Calorimeter Tower Unit: Side-view of a STAR Pb-scintillator sampling BEMC tower showing the compression plate components and the mounting system. The location of the Shower Maximum Detector, at a depth of approximately $5.6X_0$ from the front plate at $\eta = 0$, is defined by two grid-like layers (planes).

tional electron (or photon) identification. Figure 2.10 shows reconstructed charged TPC tracks matched to energy deposits in the BEMC towers.

2.2.3.2 Shower Maximum Detector

Embedded within each tower approximately $5.6X_0$ from the front plate of the stack, is the Shower Maximum Detector (SMD) sub-detector. Figure 2.11 shows the relative position of the SMD within the calorimeter tower. Not only does the SMD allow for position-resolution of incident electromagnetic particles, but the placement

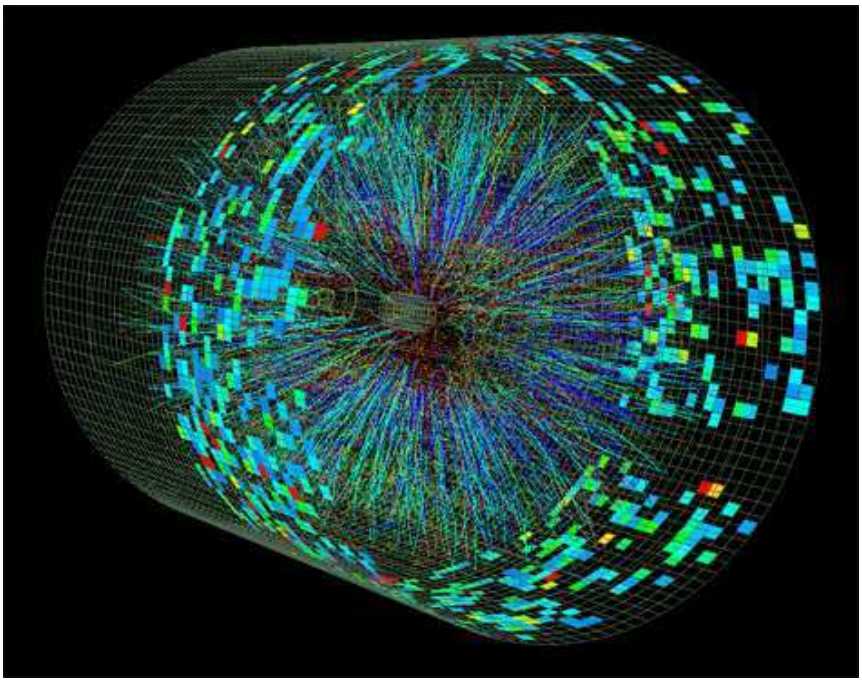

Figure 2.10: Level 3 (L3) reconstructed Au+Au event at $\sqrt{s_{NN}} = 200$ GeV.

of the SMD, behind the front plate and calorimeter material, is purposely chosen because the maximum density of electromagnetic showers from incident particles E $> \approx$ 1-2 GeV develops near this region [13]. The SMD also takes advantage of the maximum density of energy deposition for hadronic showers being nearly one interaction length (e.g., 17 cm for Pb) and thus they exhibit a much broader longitudinal distribution [13]. A technique for suppressing or rejecting hadron contaminants with the use of SMD information takes advantage of the distinctive differences in shower development between electromagnetic and hadronic processes, both longitudinally and transversely.

The longitudinal technique makes use of the energy deposited in the SMD (E_{SMD}) for comparison[3] to the total energy deposited in the tower (E_{Tower}). The maximum

[3]Internal STAR analyses have determined this to not be a straightforward implementation, due

depth of electromagnetic showering is logarithmically dependent on energy, making the longitudinal shower signal useful over a comfortably wide energy spectrum (1-2 GeV) [13]. At lower reach of the SMD energy spectrum, 1 GeV and below, the depth of most developing showers dissipates to less than $5.6X_0$, and the overall effectiveness of the SMD to contribute towards electron discrimination subsides [13]. The presence of hadrons passing SMD electron identification cuts are accredited to hadronic showers which developed early in the tower.

Figure 2.11: SMD in a BEMC tower in STAR (red-highlight).

The transverse technique for suppressing or rejecting hadron contaminants with the SMD can be facilitated by noting the distinctive differences in shower development for electromagnetic particles versus hadronic particles and the transverse-direction (Molier radius), centered at the 'seed' of shower activity. The response of the strips of the SMD to electromagnetic activity (e.g. electrons) relative to hadronic activity is, in principle, noted by the differences in the 'broadness of a shower profile' - the Moliere radius ($R_{Moliere}$). Electromagnetically-induced showers exhibit more narrow (compact) profiles with typically 95% of the shower energy contained in a

to 'saturation' in the E_{SMD}.

radius R = $2R_{Moliere}$ (e.g., $2R_{Moliere}$ = 3.2 cm in Pb) [13]. On the other hand, the transverse dimensions of hadronic showers are much larger when fully developed at approximately one hadronic interaction length. However, given that they are not usually fully developed at $5.6X_0$, hadrons leave a much narrower signal in the BSMD. Figure 2.12 shows the grid-like planes of the SMD, allowing for the $\phi - \eta$ position and shower profile of incident particles.

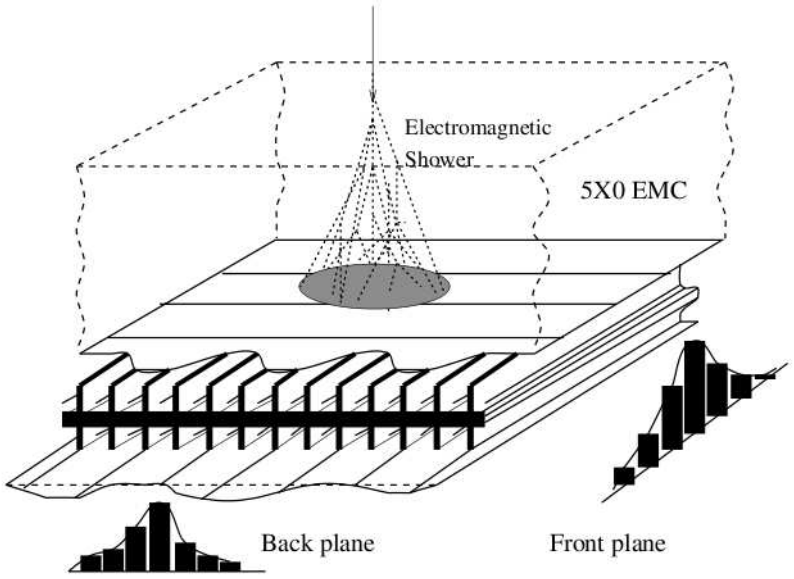

Figure 2.12: SMD-planes.

2.2.3.3 Preshower Detector

The data from the first 2 layers of each BEMC tower is read out separately and formally defines the Barrel Preshower (BPRS) detector in STAR. The BPRS distinguishes between electrons developing a shower early in the calorimeter tower as

opposed to interactions that occur beyond these first 2 layers. Figure 2.13 shows the BPRS (blue-highlight), relative to the location of the SMD detector (red-highlight). The interaction probability for hadrons (Pb only) is $\approx 3\%$ before layer 1 and $\approx 6\%$ before layer 2. In the BPRS, $\approx 63\%$ of electrons will shower before the scintillator layer 1 and $\approx 84\%$ before layer 2. A more extensive overview of the BPRS, its role in electron identification and its calibration will be given in Chapter 3.

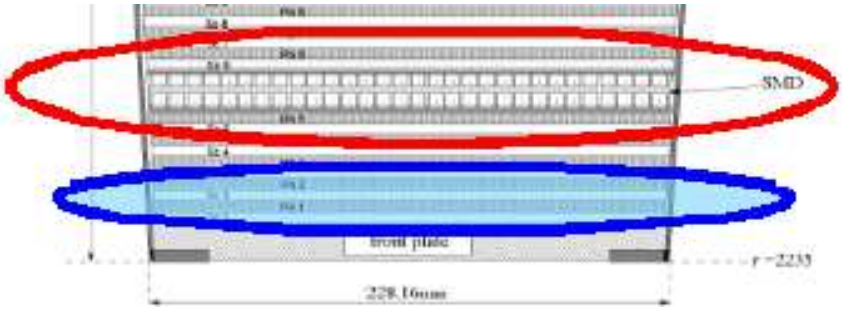

Figure 2.13: BPRS in a BEMC tower in STAR (blue-highlight).

3. ELECTRON IDENTIFICATION

This chapter details electron identification in STAR and a study of the STAR Barrel Preshower (BPRS) as a means to identify electrons. The need for electron identification is presented along with the standard methods used for electron identification, as well as an investigation into the effect of using the BPRS detector. Comparison of an electron-based analysis with and without the BPRS will be discussed. Concluding remarks about the effect of the BPRS selection on the J/ψ and Υ invariant mass peaks in Run-7 Au+Au 200 GeV (2007) collisions are presented.

3.1 Standard STAR Selection-cuts

Reconstructing decays such as $\Upsilon \rightarrow e^+e^-$ depend critically on strong electron identification. STAR electron identification is performed with the core detectors: 1) Time Projection Chamber (TPC) and 2) Barrel Electro-Magnetic Calorimeter (BEMC). The complimentary information from the TPC and BEMC may be used to match track information to energy deposition.

3.1.1 Identification: dE/dx

The gas-filled TPC chamber is the transport media for the ionization process for measuring the energy loss experienced by charged particles per unit path length. The electrons (or other charged particles) traversing a known media will lose their energy as predicted by the Bethe-Bloch equation

$$\frac{dE}{dx} = Kz^2\frac{Z}{A}\frac{1}{\beta^2}\left[\frac{1}{2}\ln\frac{2m_ec^2\beta^2\gamma^2T_{max}}{I^2} - \beta^2 - \frac{\delta}{2}\right] \tag{3.1}$$

where A, Z are the atomic mass and number of the gas, K = $4\pi N_A$ $r_e m_e c^2$ and δ is the density-effect correction. T_{max} is the maximum kinetic energy which may be imparted to a free electron in a single collision, and can be calculated as

$$T_{max} = \frac{2m_e c^2 \beta^2 \gamma^2}{1 + 2\gamma m_e/M + (m_e/M)^2} \tag{3.2}$$

for particles with mass M and momentum $M\beta\gamma$c. The mean excitation energy I is estimated based on experimental stopping-power measurements[1].

To first-order the energy loss dE/dx may be considered as a function of particle velocity β. Therefore, a momentum measurement allows the particles of different masses to be distinguished. It is expected that the mean energy loss behaves as a function of the momentum. Figure 3.1 shows different particle species which can be clearly distinguished. The predictions for electron, pion, kaon, proton, and deuteron are plotted and describe the data well. However, the identification of electrons is difficult at low-p_T because the electron band crosses over (overlaps) with several of the hadron bands. The strong 'relativistic rise' of electrons at high-p_T makes dE/dx identification less difficult; for example, the high-momentum (high-p_T) electron daughters from an Υ decay.

It is important to mention the more precise Bichsel Eqn. (3.3), applicable for thin materials. This formulation quantitatively describes the particle identification with dE/dx in terms of the definition of a variable $n\sigma_x$ (where x = π, K, p, e, etc.) is defined as:

$$n\sigma_x = \frac{1}{R} \log \left[\frac{(dE/dx)_{measured}}{\langle dE/dx \rangle_x} \right]. \tag{3.3}$$

Here $(dE/dx)_{measured}$ is the measured mean dE/dx value for a charged track, $\langle dE/dx \rangle_x$ is the expected mean dE/dx value from Bichsel's formula for charged-particle x, for a

[1]The main source of uncertainty in the calculations of the expected mean energy losses in dE/dx.

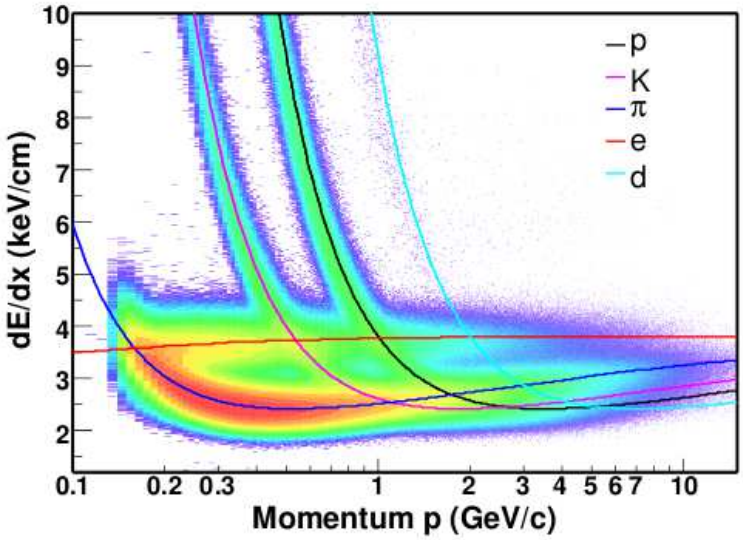

Figure 3.1: The distribution of dE/dx vs momentum for BEMC triggered data in Run-6 p+p collisions.

given momentum. The quantity R is the resolution of dE/dx - this value depends on the characteristics of each track, such as number of hits (N_{hits}) as measured by the TPC and used to calculate the measured dE/dx value, as well as the pseudo-rapidity (η) of a charged track (see Eqn. (2.2)). Recalling the previous discussion of the TPC in Chapter 2, the criteria for 'good' dE/dx resolution requires that the number of dE/dx hits included in the truncated mean method to be $N_{hits} \geq 15$. Figure 3.2 shows the difference of $n\sigma_e$ between electron and various charged hadrons (π, K, p). The e and π separation is within 3σ at $p_T < 0.2$ GeV/c, the e and K separation is within 3σ at $0.35 < p_T < 0.65$ GeV/c shows the e and p separation is within 3σ at $0.7 < p_T < 1.2$ GeV/c. The electron dE/dx band in the low-p_T range does not separate significantly from the other hadrons. At higher p_T, due to the relativistic rise of the electron, the ability to differentiate electrons and hadrons improves, and

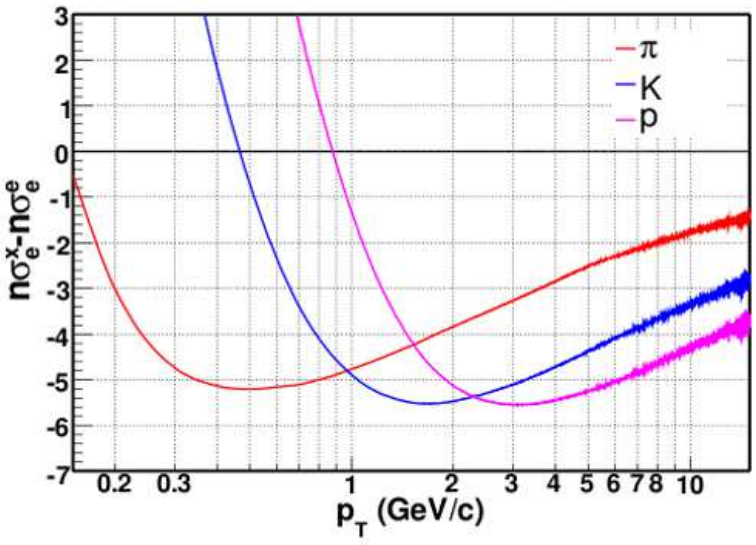

Figure 3.2: The Bichsel function plotted as a function of p_T: expected $n\sigma_e$ difference between e/π, e/K and e/p.

the electron band is situated well above all of the three hadron bands. However, the electron yield in this region is too sparse to allow for easy identification.

3.1.2 Identification: p/E

Charged tracks which follow helical trajectories are projected onto the BEMC. The measured energy deposition in the BEMC tower(s) from any particular projected track candidate is compared to the TPC-measured momentum. The relatively small rest energy of an electron that carries sufficient transverse momentum to reach the BEMC will undergo electromagnetic interactions with a tower(s), and in the process, the electrons will deposit most of their energy within the tower(s) [13]. As such, the relativistic energy of the electron reaching the TPC is dominated by the momentum term, and the energy recorded by the BEMC tower(s) is effectively equivalent

to a measurement of the momentum measured in the TPC. In electron identification, one should expect an electron to have a value of p^{TPC}/E^{tower} centered at an approximate value of 1. Hadrons will not deposit all of their energy within the BEMC and p^{TPC}/E^{tower} will have a wide distribution. The signature of hadrons in a p^{TPC}/E^{tower} distribution is identified via the presence of the notably wider distribution in p^{TPC}/E^{tower}. Hadron tracks that have passed the strict dE/dx electron cuts will leave a well defined TPC track, but will not undergo a high level of interaction with an electromagnetic calorimeter. The strict electron-rich dE/dx cut will reduce the population of hadronic tracks in the electron track sample, but the hadrons that do make it through electron cuts will have a *predictably* smaller denominator in the p^{TPC}/E^{tower} quantity, and thus higher values in p^{TPC}/E^{tower} will be seen. Figure 3.3 shows the electron candidates (black) overlayed with the hadron background (red) in Run-6 p+p at 200 GeV [27]. It is important to point out that the effect of 'energy sharing' (leakage) between two (or more) adjacent towers from an electron depositing energy will skew the p^{TPC}/E^{tower} distribution from unity.

3.1.3 Identification: BSMD

The response of the BSMD to electrons relative to the response of hadrons can also be of use in electron-based analyses. The differences in the broadness of shower profiles is one of the features that can be exploited. Figure 3.4 shows the electron candidates (left) compared to the hadron candidates (right) in Run-6 p+p at 200 GeV. The figure shows how a cut on the number of strips can help differentiate between electron and hadrons.

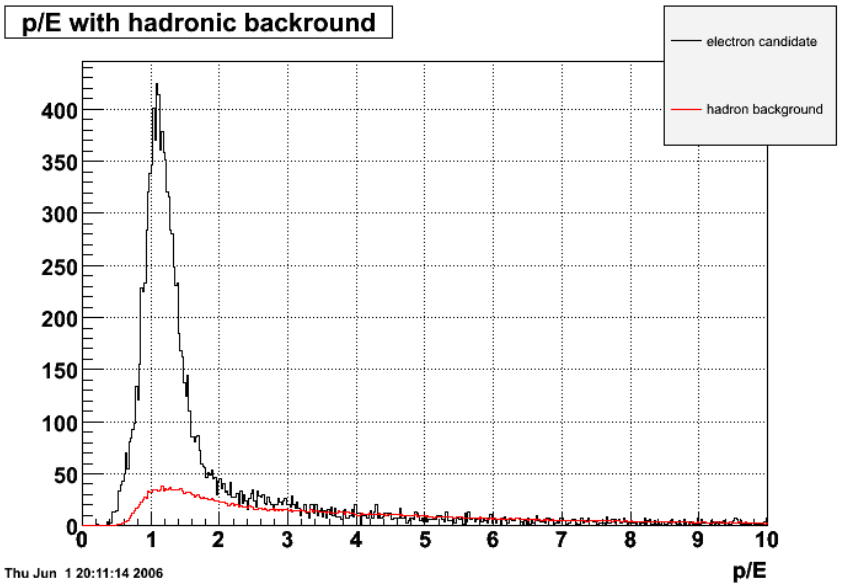

Figure 3.3: The p/E distribution plotted for electron candidates (black) and hadron background (red) in Run-6 p+p at 200 GeV data [27].

3.2 Exploring the BPRS Signal

Recall from Chapter 2 that the BSMD is embedded within the design of the calorimeter tower. There is another detector element defined within each calorimeter tower, having separate data readout and functionality. The data from the first 2 layers of each calorimeter tower is formally defined as the Barrel Preshower (BPRS) detector. The BPRS is designed to differentiate between electrons which develop a shower early in the calorimeter tower, as opposed to interactions that occur beyond these first 2 layers. Therefore, use of the BPRS can help to reduce the hadronic background by increasing the electron-hadron separation in the BEMC.

Figure 3.5 shows the BPRS ADC readout for Run-7 (2007) data. The individual readout of each BPRS channel can be projected for each tower and any distinguishing features may be discerned from the spectrum, such as towers that are 'dead.' The

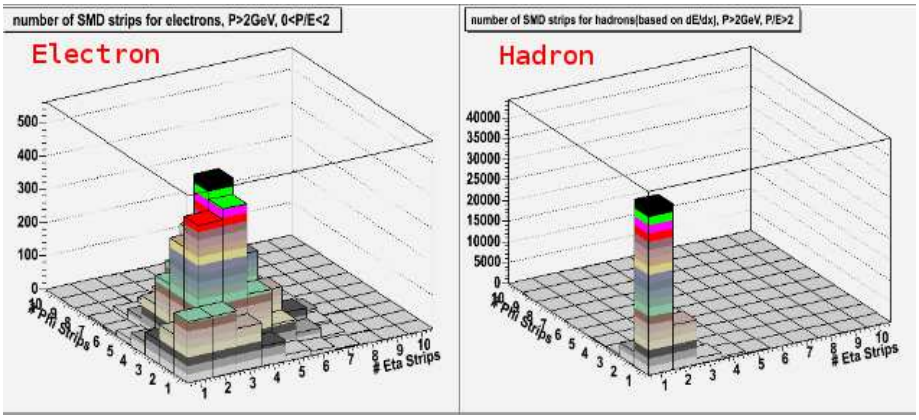

Figure 3.4: The BSMD distribution plotted for electron candidates (left) and hadron candidates (right) in Run-6 p+p at 200 GeV data.

BPRS may also suffer from incorrect 'cable mappings' which must be accounted for and corrected. The corrected maps and swaps are provided and taken as the starting point for the analysis. The combined fix of hardware/software readout issues results in an approximate 10-15% improved resolution with all bad channels masked, translating to an approximate 88% of preshower channels working during Run-7 Au+Au collisions. Figure 3.6 show the typical shape of the ADC spectrum for BPRS channel 237 and it can be seen that the ADC spectrum is 'shifted upwards' in ADC value, the result of underlying electronics voltages in the detector. Each BPRS ADC channel sits on top of what is called a 'pedestal.' The pedestal is a baseline ADC signal stemming from the electronic detector sitting on top of the background voltage that is used to 'set' the BPRS within reach of its threshold for detecting electrical activity from interactions with charged particles, called Minimum Ionizing Particles MIPs (such as electrons). The pedestal values for the BPRS channels can be calculated by collecting data when there is no-beam present in the STAR detector (or by using data with no tracking). The pedestal values can be systematically

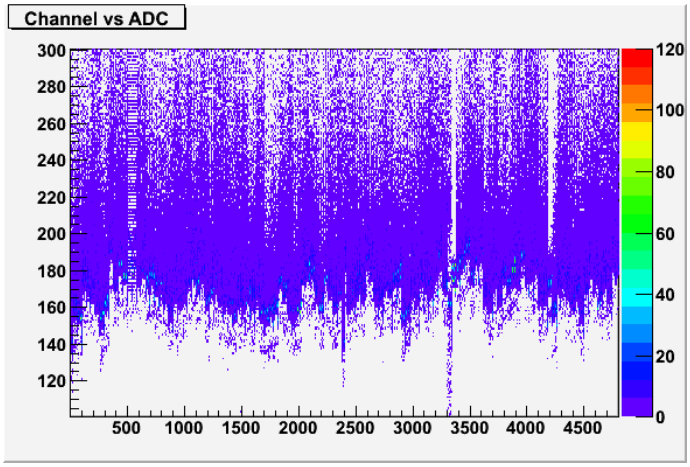

Figure 3.5: BPRS - Run-7 Au+Au 200 GeV data: Typical ADC vs. Channel number.

subtracted from the physics data, collected for each channel. Figure 3.7 shows BPRS channel 237, before pedestal subtraction (upper panel), and after subtraction of the pedestal value (lower panel). Also shown in Figure 3.7 (lower panel) is the fit of the ADC spectrum (pink line), which provides us with information on the mean and width of the ADC MIP, as well as the slope of the ADC spectrum in the electron-rich region of the BPRS ADC spectrum. The electron-rich region is where the subject of calibrating the BPRS will focus. Figure 3.8 shows an ADC spectrum from the BPRS Channel number 237. A general study using the ADC $>$ 65 (electron-rich portion of the spectrum) is used to procure a qualitative and semi-quantitative 'proof-of-principle' statement, in the absence of a full calibration (which was performed at a later time).

3.3 Effectiveness of BPRS in Electron Identification

Sampling approximately 360K Level 2 BEMC 'gamma-triggers' allows for an electron identification study in Run-7 Au+Au 200 GeV data to be performed. Only

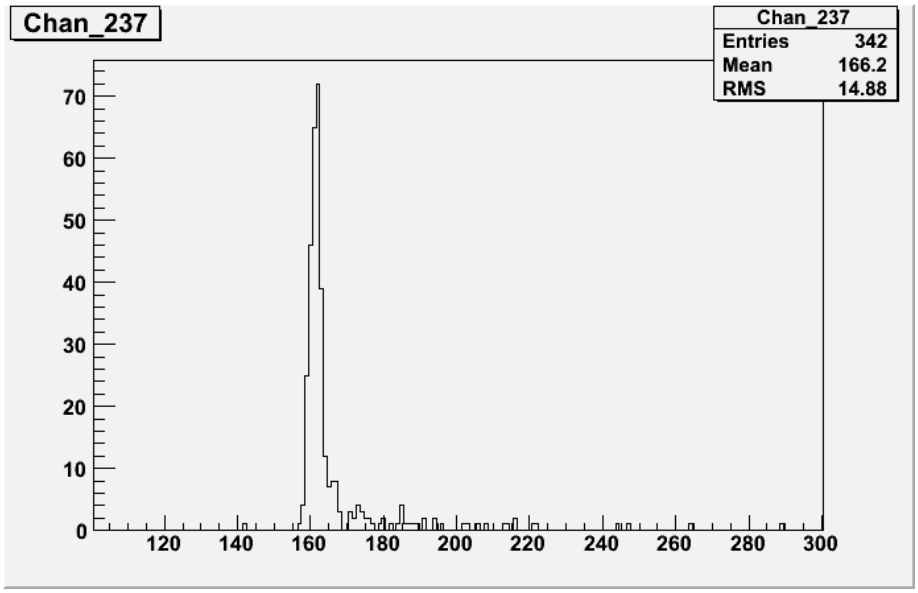

Figure 3.6: BPRS - Run-7 Au+Au 200 GeV data: ADC values recorded for Channel number 237.

a rough calibration of this data set was available during the time of the study, but all gamma-triggered candidates were required to satisfy the tower energy condition of $E_{tower} > 2$ GeV. This gamma-triggered data set relied on dE/dx calibrations from Run-6 p+p (2006) data, the tower energy was not fully calibrated, and status tables for the BPRS were not yet completed. The ultimate goal for using the BPRS will be in heavy-flavor analyses (e.g. Υ and J/ψ reconstruction), and the results will be discussed in later sections. However, in the following study, the effect of a strong BPRS cut (ADC_{BPRS} signal region > 65) relative to the other methods of electron identification available in STAR is performed. Reiterating, the methods of electron identification that will be used are: TPC (dE/dx), TPC and BEMC (p/E), BSMD (shower profile), and the limiting the BPRS data to an electron-rich region via the use of the initial cut of $ADC_{BPRS} > 65$.

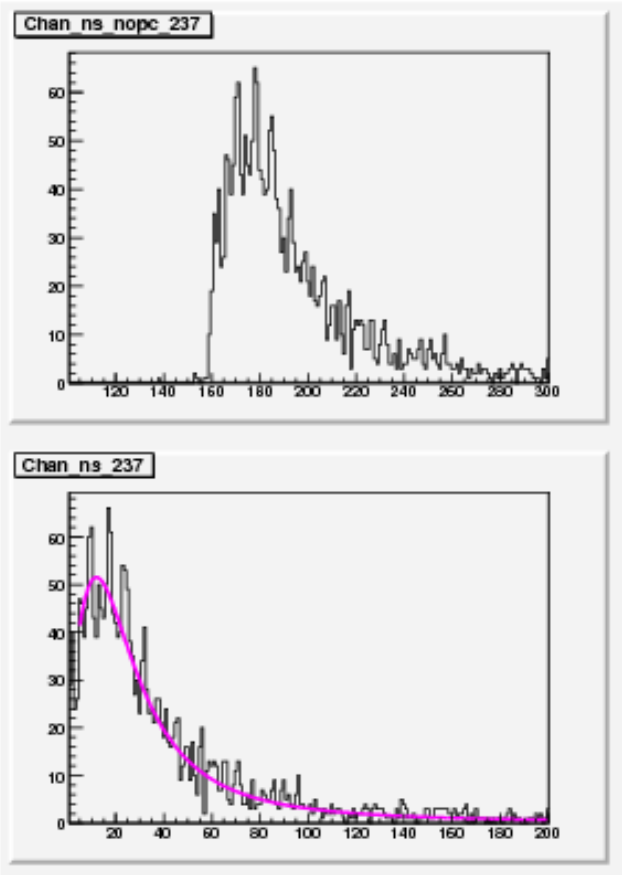

Figure 3.7: BPRS - Run-7 Au+Au 200 GeV data: Channel 237 ADC pedestal (upper panel) and ADC pedestal value subtracted (lower panel).

All TPC tracks in this study are required to project onto the BEMC tower and satisfy $E_{tower} > 2$ GeV. As a starting point, the distribution of dE/dx as a function of momentum for tracks in Run-7 Au+Au (2007) gamma-triggered data is plotted. Figure 3.9 shows the dE/dx vs. p distribution, where the red-shaded box denotes the dE/dx region in STAR which is heavily populated by electrons. In addition to the $E_{tower} > 2$ GeV trigger condition, a cut on the transverse momentum of $p_T \geq 2$ GeV/c is made. Figure 3.10 shows the one-dimensional (projected) dE/dx distribution with the $p_T \geq 2$ GeV/c applied, and overlayed with a red line that denotes the location

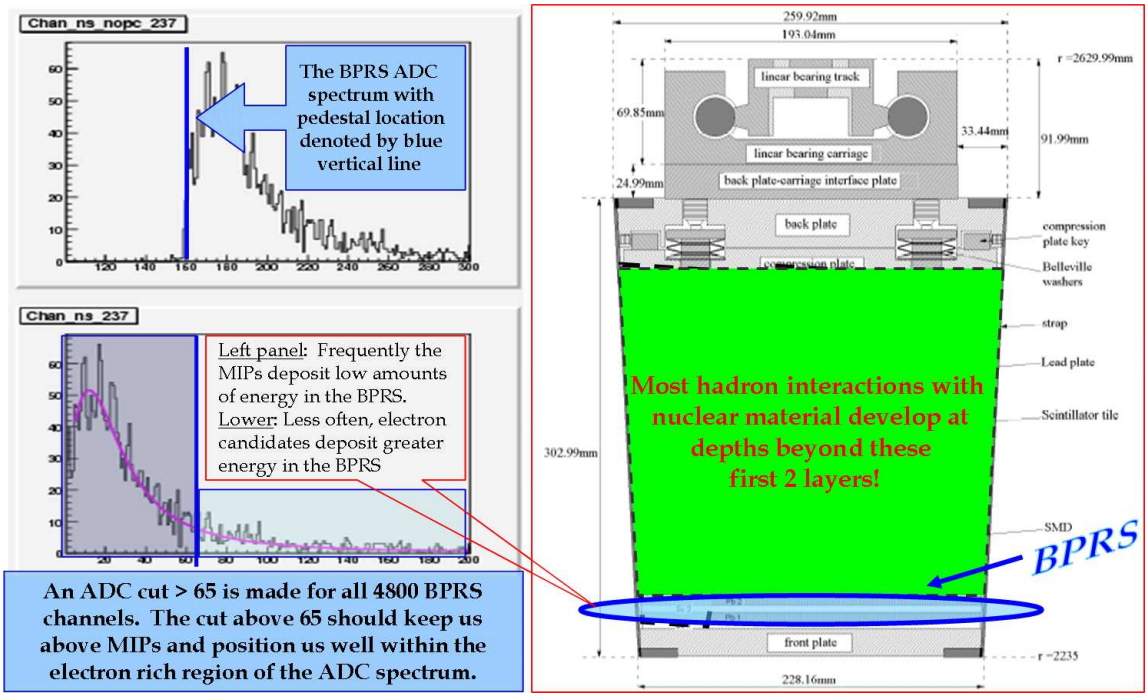

Figure 3.8: BPRS Channel 237: ADC pedestal, pedestal value subtracted, and general features.

of the the dE/dx $\geq$ 3.4 x 10^{-6} keV/cm selection[2], which is used throughout the discussions that follow.

The next step tried to determine the level of impact of a p/E cut on electron identification. Figure 3.11 shows the p/E distribution for $p_T \geq 2$ GeV/c, where it can be seen immediately that the shape is in relative accord with the expectations from the previous discussions in Section 3.1.2. The distribution has a peak at a value greater than unity, with a semi-bulky, right-side shoulder, indicative of the non-gaussian behavior of p/E due to hadronic background for which E < p. Given that there is still heavy contamination from the hadronic tracks, imposing the additional constraint that tracks be required to pass an electron identification cut of 3.4 x 10^{-6}

[2]The selection is 3.4 x $10^{-6} \leq$ dE/dx $\leq$ 5.0 x $^{-6}$ keV/cm

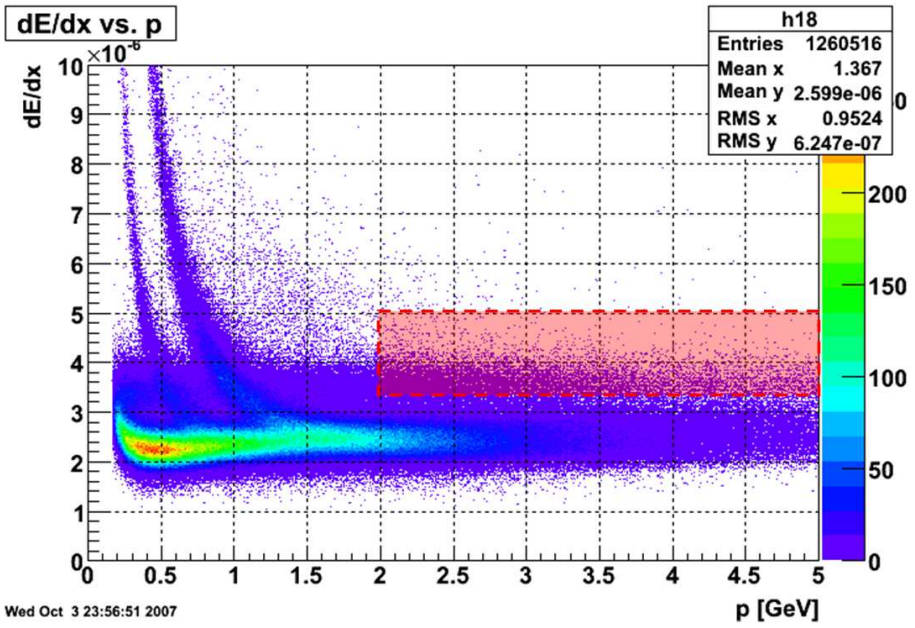

Figure 3.9: Au+Au 2007: dE/dx vs. p with a red-shaded box denoting the electron-rich region of dE/dx in STAR.

$\leq$ dE/dx $\leq$ 5.0 x $^{-6}$ keV/cm is made. Figure 3.12 shows the p/E distribution for $p_T \geq 2$ GeV/c and with the dE/dx cut applied. It can be seen that the shape is more narrow in profile, again, consistent with general expectations discussed in Section 3.1.2, thus indicating that the p/E sample undergoes a sizable reduction in the levels of hadron contamination. Note also that Figure 3.12 shows the typical p/E < 2 cut used in STAR (indicated by the red line), clearly showing that p/E $<$ 2 will provide only a minimal effect on data. The tight electron dE/dx cut is the workhorse of the two, when removing hadrons, and is particularly effective for $p_T >$ 2 GeV/c.

To understand the effect that a BSMD cut would have on electron identification in the high-multiplicity environment of Run-7 Au+Au collisions, the BSMD profile (η-strips and ϕ-strips) in the low-multiplicity environment of Run-6 p+p collisions

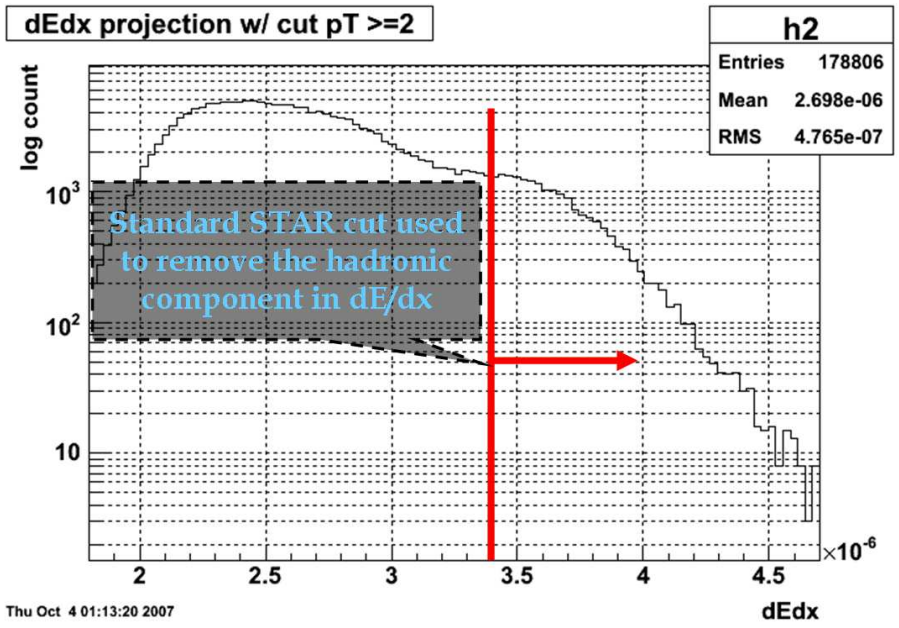

Figure 3.10: Au+Au 2007: One-dimensional dE/dx projection with a red line denoting the electron-rich region of dE/dx in STAR.

was studied first. Figure 3.13 shows the lego plot of η-strips vs. ϕ-strips in the (dE/dx $<$ 3.4 x 10^{-6}) hadron region (upper panel) and in the (dE/dx $\geq$ 3.4 x 10^{-6}) electron region (lower panel). To measure the relative strength of any given electron identification cut, the behavior of the dE/dx distribution is chosen as a standard 'reference point', upon which additional cuts may be applied. The first step defines a dividing-line that splits the dE/dx distribution into two regions - this dividing-line splits the dE/dx region into dE/dx $<$ 3.4 x 10^{-6} (the hadron region) and the dE/dx $\geq$ 3.4 x 10^{-6} (the electron region). The BSMD distribution allows for the resolving between electron-like and hadron-like interactions in the calorimeter - hadrons are indicated by a more narrow profile than that of the distribution for the electrons. Using the BSMD electron identification cut of $\eta_{\#strips} > 1$ and $\phi_{\#strips} > 1$, allows for the effect on the shape of the dE/dx distribution in Run-6 (2006) p+p collisions

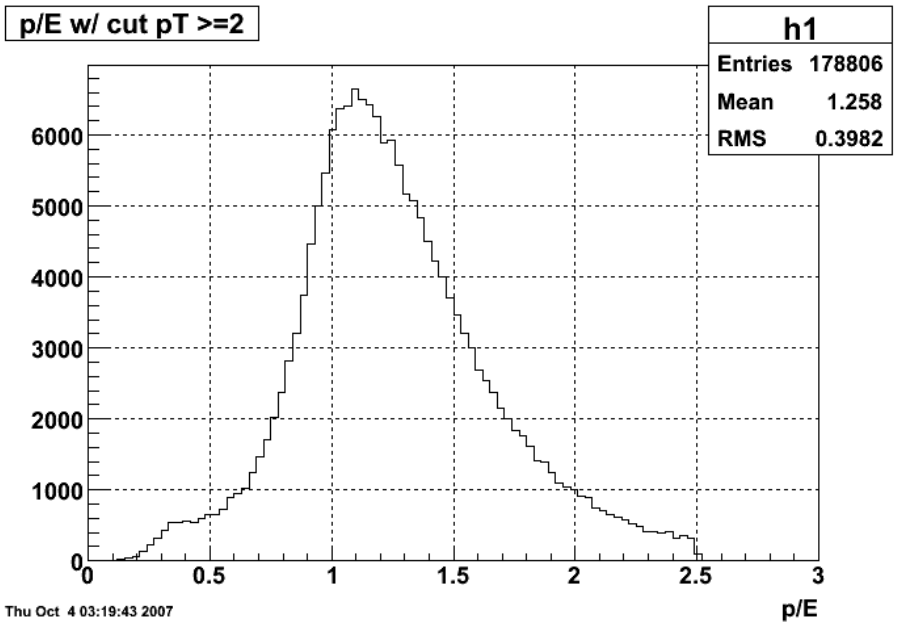

Figure 3.11: Au+Au 2007: STAR p/E distribution for $p_T \geq 2$ GeV/c and no dE/dx cut applied.

to be made. To make comparisons between whether or not the particular use ('on') or non-use ('off') of a particular cut it is beneficial in electron identification, the ratio of $\text{cut}_{on}/\text{cut}_{off}$ is used. Extending the use of this ratio a bit further, a definition is made

$$ {}^{AA}R_{pid}^{region} = \frac{\left(\frac{dE}{dx}\right)_{[pid(on)]}}{\left(\frac{dE}{dx}\right)_{[pid(off)]}} \tag{3.4} $$

where ${}^{AA}R_{pid}^{region}$ is the fraction of events (tracks) which survive in a particular region (hadron or electron) and AA denotes the collision system (p+p or Au+Au). The value of ${}^{AA}R_{pid}^{region}$ will be used to form a semi-quantitative argument about the relative strength of a specific cut (or cuts) relative to each other. The '*pid*' is variable or interchangeable, indicating which electron identification cut/method is currently being used (SMD, BPRS, etc.), and the '*region*' specifies whether this value is as-

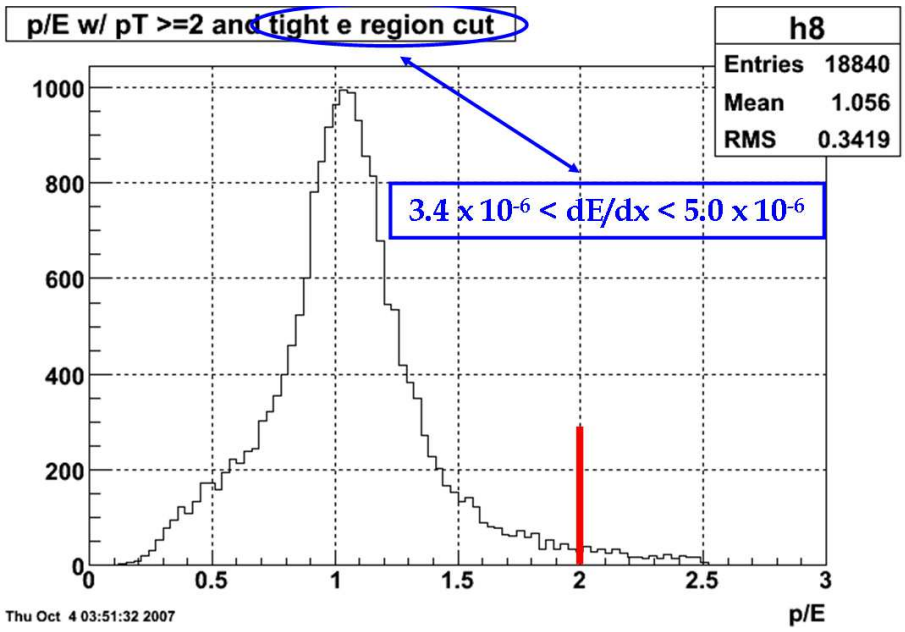

Figure 3.12: Au+Au 2007: STAR p/E distribution for $p_T \geq 2$ GeV/c and a strong dE/dx cut applied.

sociated with the hadron or electron region. Finally, the status of a cut/method is indicated by the use of '*on*' or 'off', respectively.

Immediate use of Eqn. (3.4) helps to study the effect of a BSMD cut on the population of tracks in the dE/dx distribution in Run-6 p+p data by taking the ratio of the dE/dx distributions,

$$^{pp}R_{SMD}^{region} = \frac{\left(\frac{dE}{dx}\right)_{[SMD(on)]}}{\left(\frac{dE}{dx}\right)_{[SMD(off)]}}. \tag{3.5}$$

Figure 3.14 shows the dE/dx distribution used in the numerator (left panel) and the corresponding dE/dx distribution used in the denominator (right panel). The SMD cut in Figure 3.14 (left panel) clearly shows a dE/dx distribution with a more

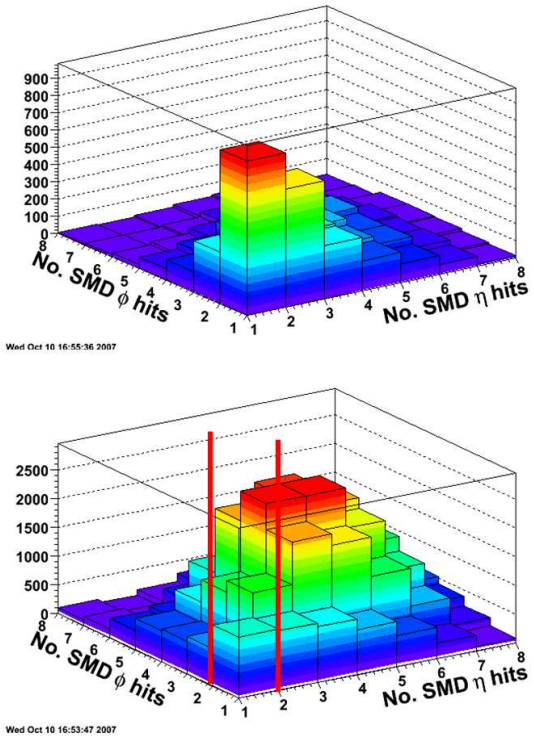

Figure 3.13: SMD - Run-6 (2006) p+p 200 GeV data: SMD profile in the hadron region (upper panel) and electron region (lower panel). The red vertical lines indicate the locations of standard STAR electron identification cuts: $\eta_{\#strips} > 1$ and $\phi_{\#strips} > 1$.

pronounced 'hump' in the electron region. I.e. the overlapping hadron and electron gaussian distributions are clearly more distinguishable than in the case where the SMD cut is not applied (off), as depicted in Figure 3.14 (right panel). To find the relative fraction surviving the SMD cut in each region (${}^{pp}R_{SMD}^{hadron}$ vs. ${}^{pp}R_{SMD}^{electron}$), the distributions from the Figure 3.14 are input into Eqn. (3.6).

Figure 3.15 shows that in the hadron region there is an approximate loss of 45% of events (${}^{pp}R_{SMD}^{hadron} \approx 55\%$), while the electron region shows an approximate loss of 15% (${}^{pp}R_{SMD}^{electron} \approx 85\%$). The semi-quantitative SMD rejection difference on the track

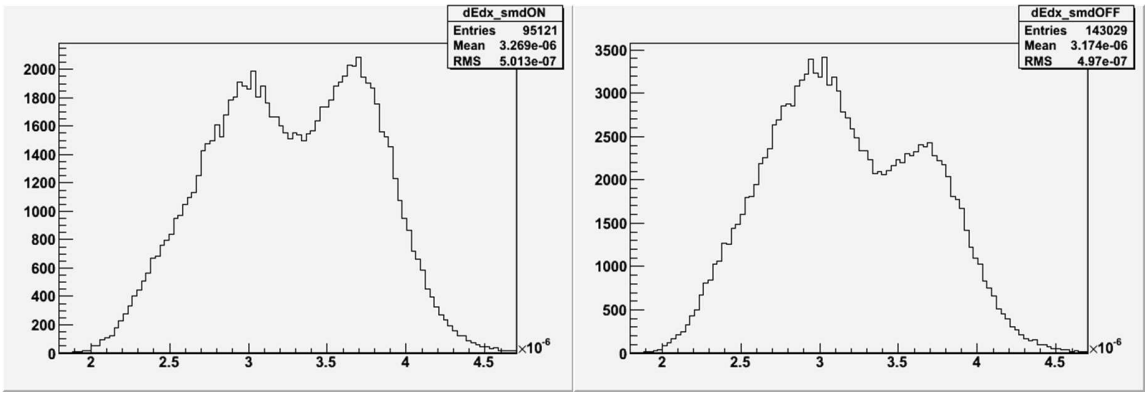

Figure 3.14: The dE/dx distribution plotted for SMD on (left) and SMD off (right) in Run-6 p+p at 200 GeV.

sample between hadron and electron regions is $\Delta^{pp}R_{SMD} \equiv {}^{pp}R_{SMD}^{electron}$ - ${}^{pp}R_{SMD}^{hadron} \approx$ 30%.

The SMD distributions in Run-6 p+p data for hadron (dE/dx $<$ 3.4 x 10^{-6}) and electron (dE/dx $\geq$ 3.4 x 10^{-6}) regions were shown in Figure 3.13 and the same set of profile distributions in Run-7 Au+Au (gamma-triggered) will presumably suffer in its ability to resolve or differentiate, due to the higher multiplicity of charged tracks produced during Au+Au collisions. It was seen that in Run-6 p+p collisions the SMD profile allowed for differentiation between hadron-like and electron-like signals (Figure 3.13), and it was also concluded that $\Delta^{pp}R_{SMD} \approx 30\%$ indicates an advantage in making this cut in data (larger values of $\Delta^{AA}R$ are good). However, the level of functionality for making this cut in the Au+Au collision system was not obvious and required due consideration. Figure 3.16 shows the BSMD profile for the Run-6 and Run-7 samples, for the hadron and electron (dE/dx) regions in discussion. Recall that the BSMD distributions for the electron and hadron regions in the p+p data (Figure 3.16 lower-left and lower-right panels) does appear to sufficiently discriminate

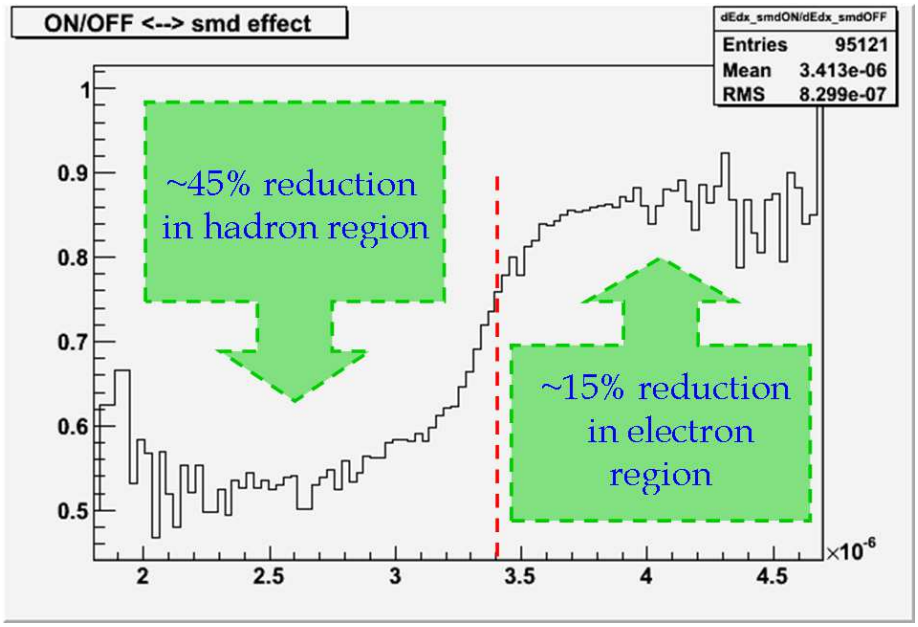

Figure 3.15: p+p 2006: Fraction of events remaining after the SMD cut of $\eta_{\#strips} > 1$ and $\phi_{\#strips} > 1$, as a function of particle dE/dx.

between the different particle species. Unfortunately, the BSMD distributions in the Au+Au data for electron and hadron regions (Figure 3.16 upper-left and upper-right panels) does not look to be as effective in discriminating relative to the p+p data. The SMD appears to be less effective in the high-multiplicity environment of Au+Au collisions, and therefore the use of the BSMD for electron identification is not straightforward in Au+Au data.

Using Eqn. (3.4) to explore the effect of an SMD cut on the population of tracks in the dE/dx distribution, in Run-7 Au+Au data, by taking the ratio of the dE/dx distributions,

$$ {}^{AuAu}R_{SMD}^{region} = \frac{\left(\frac{dE}{dx}\right)_{[SMD(on)]}}{\left(\frac{dE}{dx}\right)_{[SMD(off)]}}. \tag{3.6}$$

Figure 3.17 shows the dE/dx distribution used in the numerator (left panel) and the

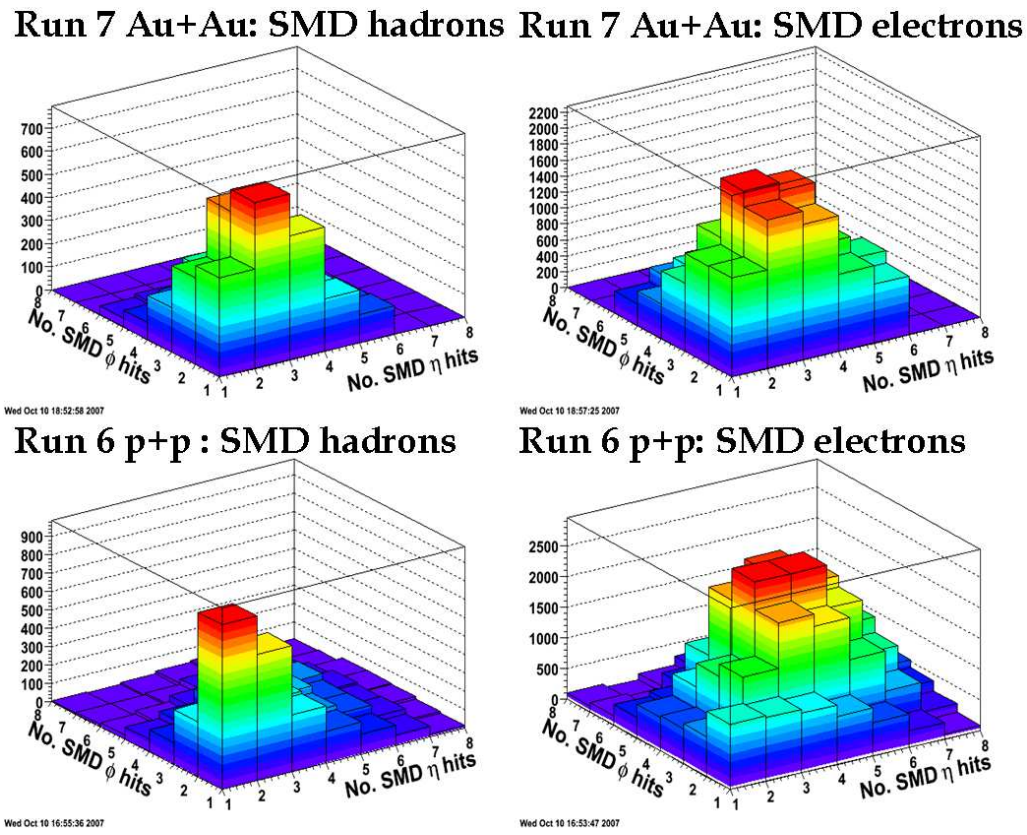

Figure 3.16: SMD response: Au+Au - hadronic region (upper-left) and electron region (upper-right). p+p - hadronic region (lower-left) and electron region (lower-right)

corresponding dE/dx distribution used in the denominator (right panel). The SMD cut in Figure 3.17 (left panel) also clearly shows a dE/dx distribution with a more pronounced 'hump' in the electron region. The overlapping hadron and electron gaussian-like distributions are only slightly more discernible in the case where the SMD cut is not applied (off), as depicted in Figure 3.17 (right panel). Similarly, to find the relative fraction surviving the SMD cut in each region ($^{AuAu}R_{SMD}^{hadron}$ vs. $^{AuAu}R_{SMD}^{electron}$), the distributions from the Figure 3.17 are input into Eqn. (3.6).

Figure 3.18 shows that in the hadron region there is an approximate loss of 50%

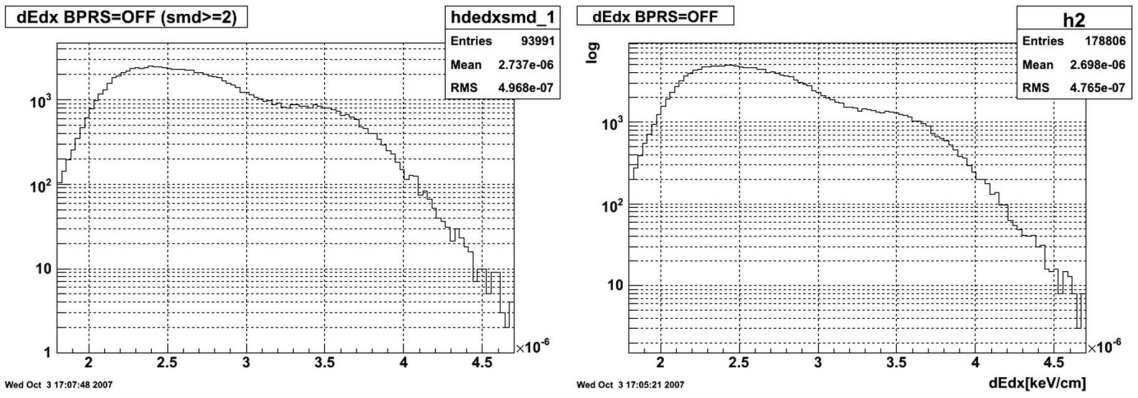

Figure 3.17: The dE/dx distribution plotted for SMD on (left) and SMD off (right) in Run-7 Au+Au at 200 GeV.

of events ($^{AuAu}R_{SMD}^{hadron} \approx 50\%$), while the electron region shows an approximate loss of 35% ($^{AuAu}R_{SMD}^{electron} \approx 65\%$). The semi-quantitative SMD rejection difference on the track sample (Run-7 gamma-trigger) between hadron and electron regions is $\Delta^{AuAu}R_{SMD} \equiv {}^{AuAu}R_{SMD}^{electron}$ - $^{AuAu}R_{SMD}^{hadron} \approx 15$ %.

The use of the SMD in Run-6 p+p collisions allowed differentiation between hadron and electron signals (Figure 3.13), and it was also concluded that $\Delta^{pp}R_{SMD} \approx$ 30%. The Au+Au distribution of Figure 3.18 shows $\Delta^{AuAu}R_{SMD} \approx 15\%$, i.e. $\Delta^{AuAu}R$ has decreased. The functionality for making this cut in the Au+Au collision system is not strikingly obvious, and while the hadron region is subjected to an extra $\approx 5\%$ hit relative to p+p data, the electron region suffers from an additional $\approx 20\%$ hit relative to the p+p data - meaning that the discrimination of hadrons and electrons in Au+Au data with the SMD appears to be heading in the wrong direction. Relative to the low-multiplicity p+p collisions, the effectiveness of the SMD cut appears to be dropping for high-multiplicity Au+Au collisions in STAR.

Studying the effectiveness of the BPRS is next. The harsh BPRS cut (ADC_{BPRS}

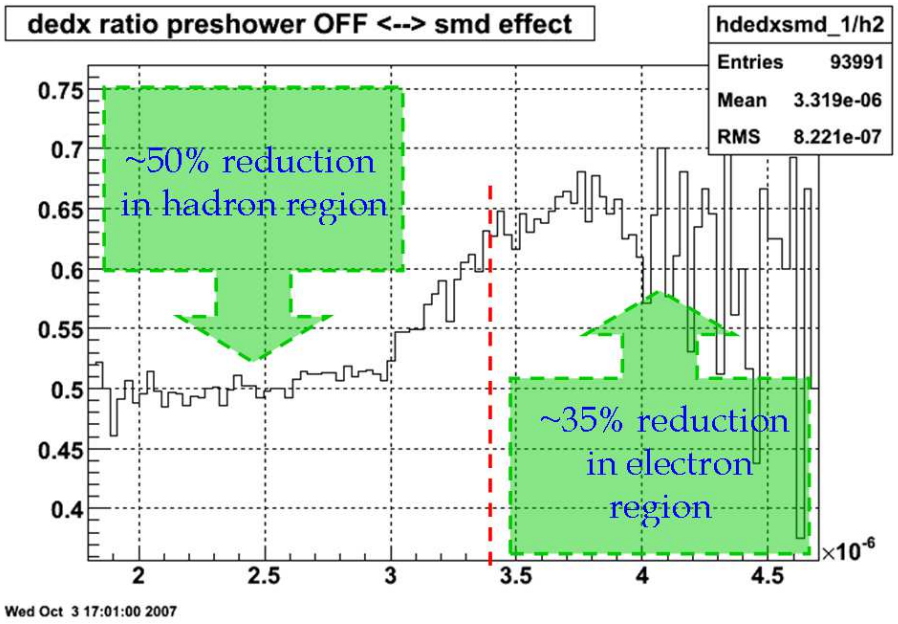

Figure 3.18: Au+Au 2007: Fraction of events remaining after the SMD cut of $\eta_{\#strips} > 1$ and $\phi_{\#strips} > 1$, as a function of particle dE/dx.

electron region > 65) is made on the tracks in the high-multiplicity Au+Au data, and then some qualitative remarks are made. The study of the BPRS cut will follow the same prescription used thus far - i.e. observing the ratio of the dE/dx distribution

$$ {}^{AuAu}R_{BPRS}^{region} = \frac{\left(\frac{dE}{dx}\right)_{[BPRS(on)]}}{\left(\frac{dE}{dx}\right)_{[BPRS(off)]}}. \tag{3.7}$$

Figure 3.19 shows the dE/dx distribution used in the numerator (left panel) and the coresponding dE/dx distribution used in the denominator (right panel). The BPRS cut in Figure 3.19 (left panel) also shows a dE/dx distribution with the electron gaussian distribution clearly distinguishable relative to the case where the BPRS cut is not applied (off), as depicted in Figure 3.19 (right panel). The relative fraction

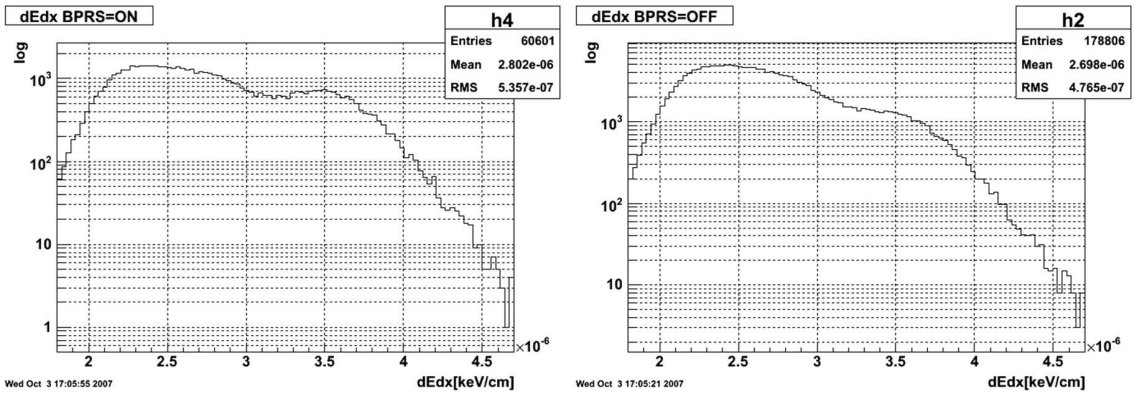

Figure 3.19: The dE/dx distribution plotted for BPRS on (left) and BPRS off (right) in Run-7 Au+Au at 200 GeV.

surviving the BPRS cut in each region (${}^{AuAu}R^{hadron}_{BPRS}$ vs. ${}^{AuAu}R^{electron}_{BPRS}$) is found using the Eqn. (3.7). Figure 3.20 shows the hadron region reduced by 70% (${}^{AuAu}R^{hadron}_{BPRS} \approx 30\%$), while the electron region is reduced by 40% (${}^{AuAu}R^{electron}_{BPRS} \approx 60\%$). The BPRS rejection difference on the track sample (Run-7 gamma-trigger) between hadron and electron regions is $\Delta^{AuAu}R_{BPRS} \approx 30\%$.

Recalling the conclusion from Figure 3.12, further electron identification (and hadron rejection) with p/E $<$ 2 GeV/c had minimal impact in the high-multiplicity environment of Au+Au data - dE/dx was the dominant source of hadron removal. It can be anticipated that the fraction of tracks removed by the BPRS + SMD + p/E in the hadron and electron regions will be approximately at the same level as the BPRS cut alone. Figure 3.21 and Figure 3.22 show that this is in fact the case, with a ${}^{AuAu}R^{hadron}_{BPRS+SMD+p/E} \approx 30\%$ and ${}^{AuAu}R^{electron}_{BPRS+SMD+p/E} \approx 60\%$, signifying a $\Delta^{AuAu}R_{BPRS+SMD+p/E} \approx 30\%$.

STAR currently has in place well-established methods for electron identification, but additional hadron discrimination using the Barrel Preshower (BPRS) is a real

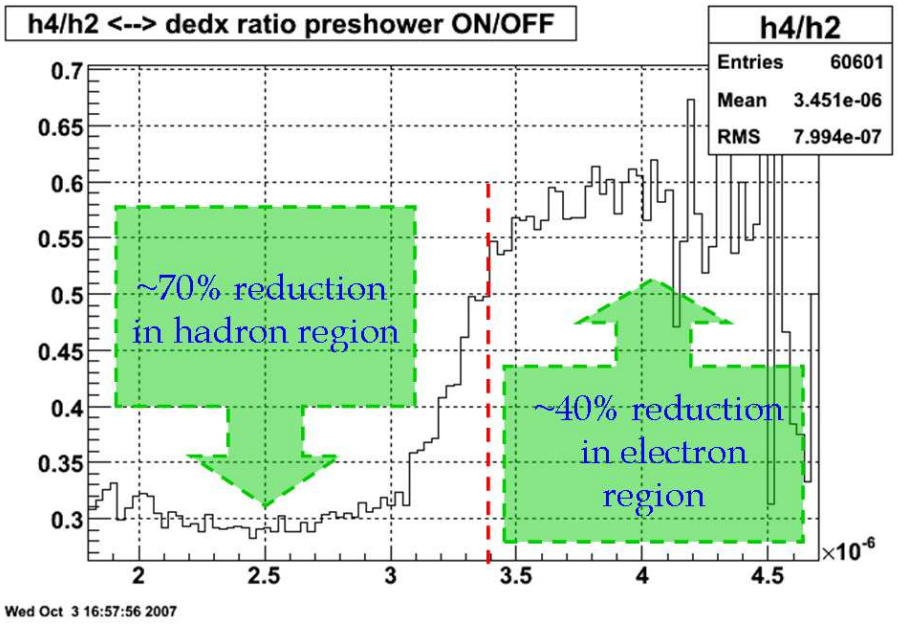

Figure 3.20: Au+Au 2007: Fraction of events remaining after the cut of $\mathrm{ADC}_{BPRS} > 65$, as a function of particle dE/dx.

possibility. The Barrel Preshower alone has a stronger effect than the cuts with Shower Maximum Detector and/or p/E < 2 cuts alone, but studies of the Shower Maximum Detector performance in high-multiplicity events (Au+Au collisions) is still necessary. The proof-of-principle provides strong indications for the possibility to improve the electron identification in STAR by using the Barrel Preshower detector. However, the performance of the BPRS in L2 Upsilon triggered electron-rich data and J/ψ from Run-7 will be the ultimate functionality test of the BPRS, but further refinements to the calibration of the BPRS are required before this is pursued.

3.4 Calibration of BPRS

The relative calibration of the BPRS channels is performed using the Au+Au 2007 MinBias data set. In principle, the BPRS may be calibrated fitting MIP peaks in the

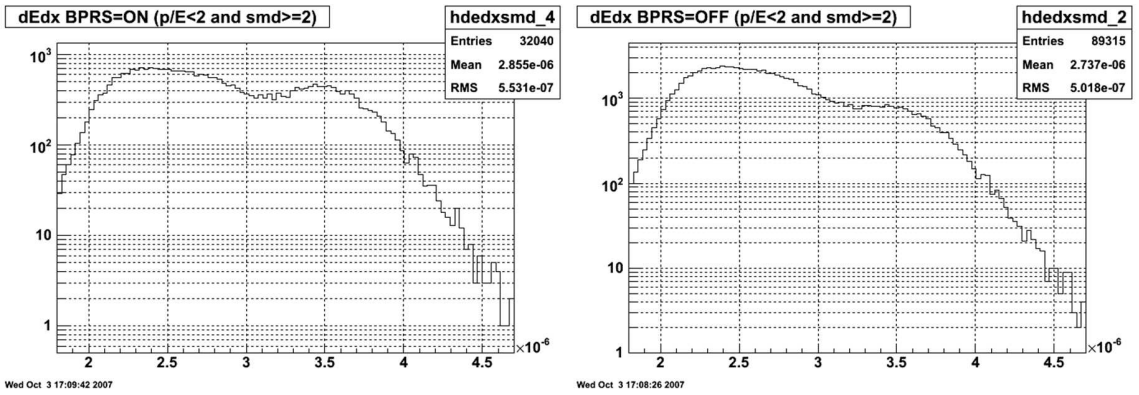

Figure 3.21: The dE/dx distribution plotted for $(\text{BPRS} + \text{SMD} + \text{p/E})_{on}$ (left) and $(\text{BPRS} + \text{SMD} + \text{p/E})_{off}$ (right) in Run-7 Au+Au at 200 GeV.

BPRS ADC spectrum as discussed in Section 3.2, but in addition, the calibration of the BPRS channels can be done by choosing an ADC region that is displaced 'far enough' above the MIP region and well into the 'slope region' (electron region) of an exponentially falling ADC spectrum. The practicality of using a slope region in the high-multiplicity environment of Au+Au at 200 GeV is because the MIP peak is more-or-less buried under the ADC spectrum (the MIP is too close to the pedestal location) at the tower-by-tower level, while the exponentially falling ADC spectrum provides a more distinguishable platform with which to calibrate. The use of the full ADC spectra with the no-tracking requirement[3] to fit slopes in the electron-rich region. The 2007 Production Minimum Bias data is used with no requirement to have track associations to the BPRS, providing a maximal amount of statistics with which to calibrate BPRS. The same dataset with tracking requirements is later used to perform an invariant mass analysis, using the calibrated BPRS.

[3]This requirement means that no TPC information is required, only information from the BEMC is necessary.

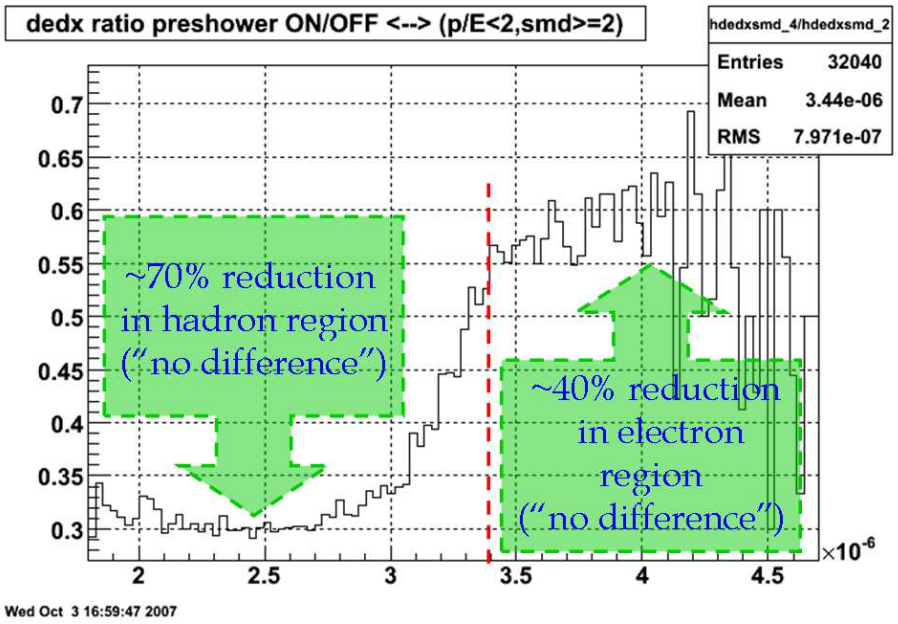

Figure 3.22: Au+Au 2007: Fraction of events remaining after the use of all electron identification methods (BPRS + SMD + p/E), as a function of particle dE/dx.

3.4.1 Exponential Slope Region

During the RHIC and STAR running, the pedestal mean and RMS (Root Mean Square) values of the BEMC and BPRS detectors are periodically recorded and stored in the database. Retrieval of these recorded pedestal mean and RMS values from the database is executed, and the reasonable assumption that subtracting the Pedestal + 5*RMS values from the ADC of each BPRS channel will move us safely into the electron region (exponential region). Comfortably situated within the sloped region, the BPRS calibration fitting routine is restricted to the constraint that each of the slope region fits must be from $30 \leq \mathrm{ADC}_{BPRS} \leq 70$. Having defined the suitable slope region and the endpoints for fitting the exponential ADC segment, there are two methods to calibrate the BPRS : 1) Area Method and 2) Slope Method. The

BPRS was calibrated on a ring-by-ring basis, with 40 rings over the full η range with each ring containing 120 towers and each ring fully azimuthal in coverage ($0 < \phi \leq 2\pi$). Both methods are discussed and the equivalency of the results from each method is confirmed.

The Area Method determines the average area (beneath the $30 \leq \mathrm{ADC}_{BPRS} \leq 70$ endpoints) of an ADC distribution for a given ring, then selects a reference channel within this ring whose ADC distribution area is closest to that ring average area. Each of the channel distributions within this ring are then adjusted to the distribution of the selected channel, such that the slope of each channel is adjusted to that of the reference channel slope.

The Slope Method determines the ring slope average (between the $30 \leq \mathrm{ADC}_{BPRS} \leq 70$ endpoints) of an ADC distribution for a given ring, then selects a reference channel within this ring whose slope is closest to that ring slope average. Each of the channel distributions within this ring are then adjusted to the distribution of the selected channel, such that the slope of each channel is adjusted to that of the reference channel slope.

The area and slope method were both used to calculate channel-by-channel gain values for the BPRS. Gain values were calculated for each method and were found to be consistent with each other. For illustrative purposes, the 'slope method' is presented.

The first step was to align the slopes of each BPRS channel within a particular ring to the slope of that ring. Figure 3.23 shows the exponential function fit to the to the slope of Ring 10 (note the log scale on the y-axis). After the slope of Ring 10 is determined, each channel within Ring 10 is exponentially fitted and the slope that most closely matches the slope of Ring 10 is used to calibrate (stretch) the ADC_{BPRS} distribution. The corrected-slope is calibrated relative to the channel

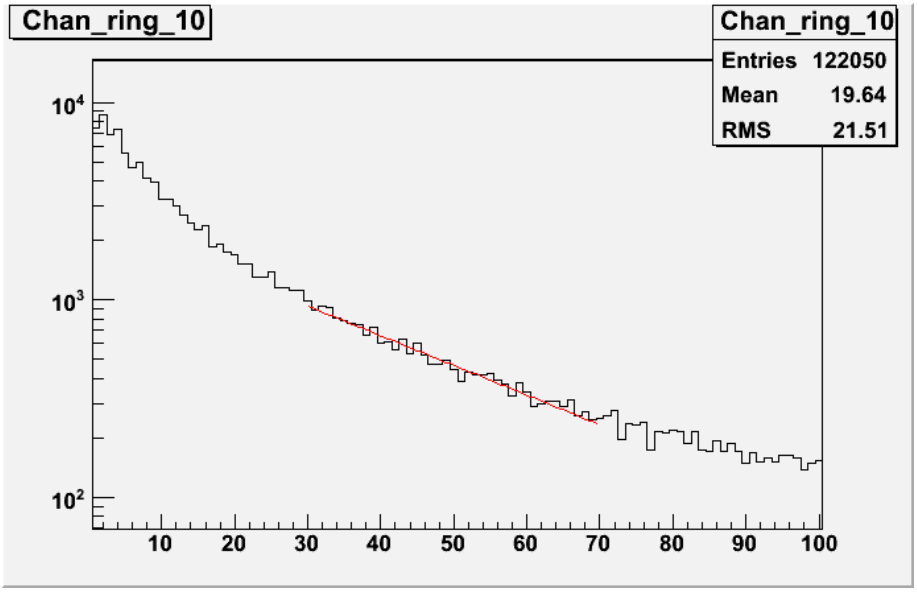

Figure 3.23: Au+Au 2007 MinBias: The ADC_{BPRS} distribution of all BPRS channels within Ring 10. The exponential function fit (faint red line at $30 \leq \mathrm{ADC}_{BPRS} \leq 70$) to which each BPRS channel within Ring 10 will be calibrated.

most closely matching the average slope of Ring 10. Figure 3.24 shows the 'uncorrected' ADC_{BPRS} for Channel 1190, which will be undergo a 'correction' to its spectrum. Once the slopes are calculated, corrections to the ADC distribution may be done following the procedure of $\mathrm{ADC}'_{BPRS_{Channel}} = \mathrm{C} * \mathrm{ADC}_{BPRS_{Channel}}$, where C is determined by the slope of individual channel $\mathrm{ADC}_{BPRS_{Channel}}$ divided by the average $\mathrm{ADC}_{BPRS_{Ring}}$ slope from a Ring. This slope-adjusting procedure is performed for each of the functional BPRS channels. Figure 3.25 shows the slope fit results for the 'uncorrected' ADC_{BPRS} spectrum for all BPRS channels within Ring 10. Each of these BPRS channels then undergo a 'correction' to its spectrum, ideally bringing each of the BPRS channel slopes within a Ring to approximately the same value as the average value of that Ring's slope. Figure 3.26 shows the slope fit results for the 'corrected' ADC_{BPRS} spectrum for all BPRS channels within Ring 10. The

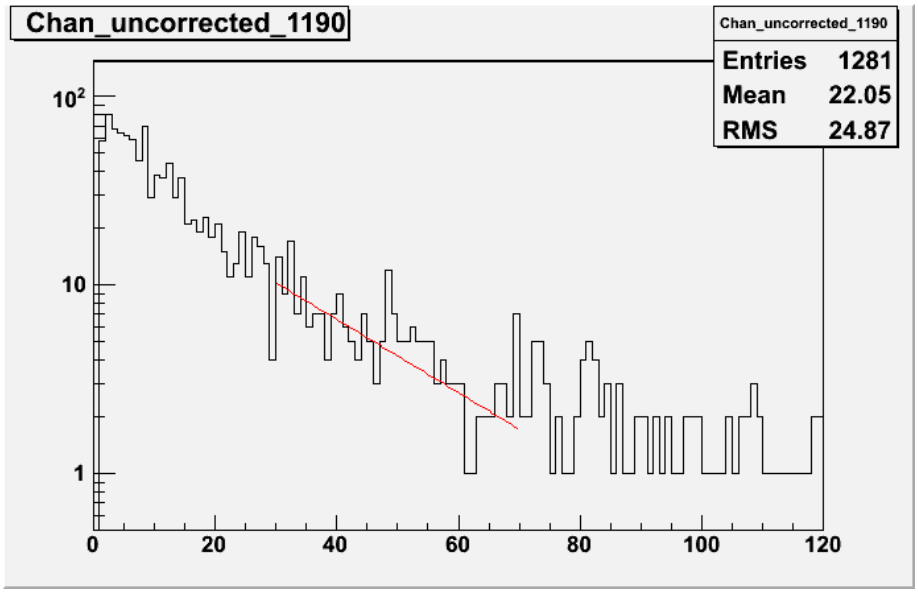

Figure 3.24: Au+Au 2007 MinBias: The ADC_{BPRS} spectrum of BPRS channel 1190 within Ring 10. The exponential function fit (faint red line at $30 \leq \mathrm{ADC}_{BPRS} \leq 70$) to the ADC_{BPRS} spectrum.

distribution of channel slopes in Ring 10 is now visibly tighter and it it feasible to consider the alignment of these slopes as sufficient to move on to the next stage of the calibration. It is necessary to adjust these 'new' slopes of each ring to a reference ring slope; the choice to adjust the 'new' ring slopes to the reference slope of Ring 10. Figure 3.27 shows the slope fit results for the individual rings before the rings are calibrated relative to the slope of Ring 10. Figure 3.28 shows the results of the Slope Method calibration: the slope fit results for the individual rings after the rings are calibrated relative to the slope of Ring 10. The 'slope method' was used to arrive at the final distribution of Ring slopes calibrated relative to Ring 10. The Ring slopes are now visibly tighter and it is accepted that the alignment of these slopes is sufficient to use for investigating the implications when using BPRS electron identification in heavy-flavor analyses. The finals results of the Ring slopes that have

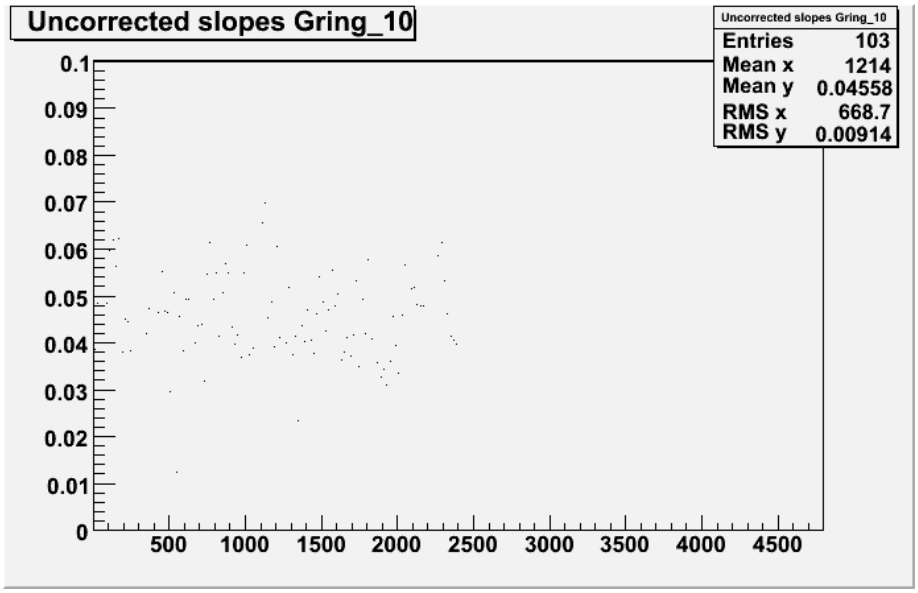

Figure 3.25: Au+Au 2007 MinBias: The uncorrected ADC_{BPRS} spectrum slopes of all BPRS channels within Ring 10.

been calibrated relative to Ring 10 using the 'area method' are shown. Figure 3.29 shows the final results of the Area Method calibration: results from the slope fits for the individual rings after the rings were calibrated relative to the slope of Ring 10. The results of the area method are consistent with the slope method.

In conclusion: The use of electron identification with a harsh BPRS cut was markedly better at hadron rejection than the sole use of the SMD and p/E methods alone. With a relative calibration of the BPRS it is possible to move towards implementing the calibrated BPRS results into electron-based analyses.

3.5 Heavy Flavor in Au+Au

Clean electron identification and the rejection of hadronic background is generally an regarded as an important 'handle', as it relates to electron-based analyses. How-

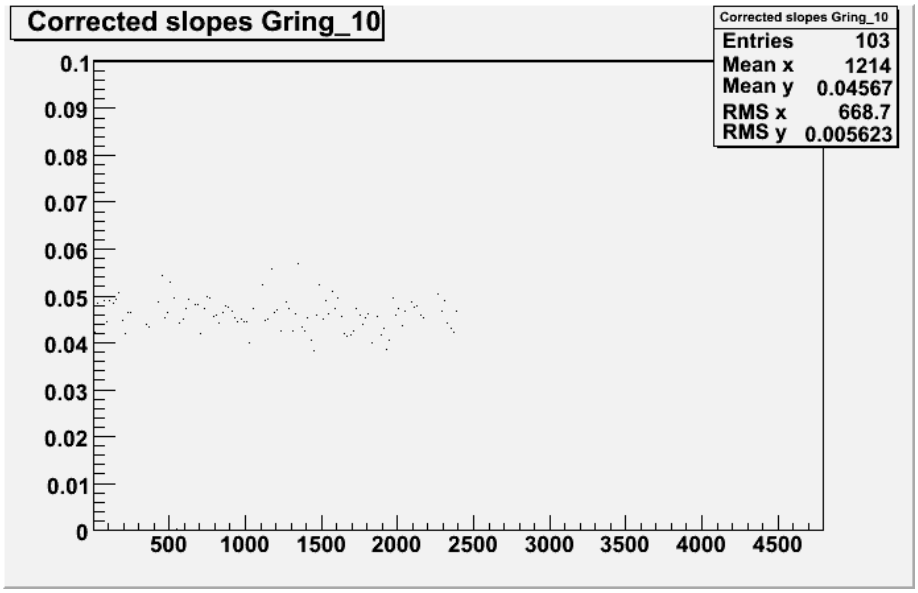

Figure 3.26: Au+Au 2007 MinBias: The corrected ADC_{BPRS} spectrum slopes of all BPRS channels within Ring 10.

ever, while electron identification is not absolutely essential during an invariant mass analysis (e.g. $\Upsilon \rightarrow e^+e^-$), a high-multiplicity environment can facilitate the need for having additional electron identification methods/tools in place. As a measuring stick for the robustness of electron identification (hadron rejection) using the BPRS in STAR, the high-multiplicity environment created by Au+Au collisions at $\sqrt{s_{NN}}$ = 200 GeV can provide a critical test case scenario for the practicality of using the BPRS in heavy flavor analyses at STAR.

3.5.1 BPRS and Υ in Au+Au

The relative calibration for the Υ invariant mass reconstruction used Υ 'triggered' data. Triggered events are inherently 'biased', however, it was the only data set available at the time, which may slightly bias the relative calibration. With this possible bias noted, an attempt at cleaning up the reconstructed invariant Υ

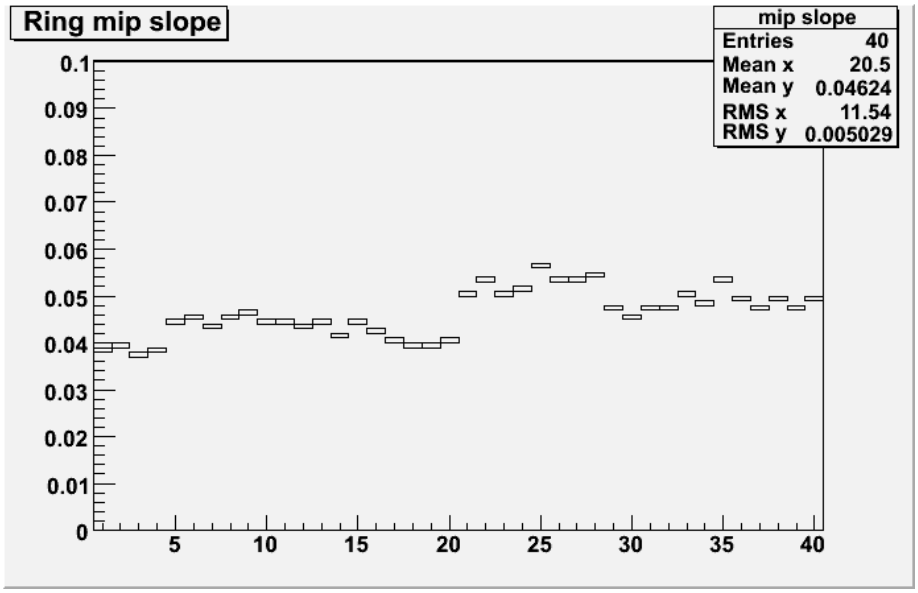

Figure 3.27: Au+Au 2007 MinBias: The ADC_{BPRS} spectrum slopes of all Rings before calibrating to the reference slope of Ring 10.

mass signal using calibrated BPRS was performed. The analysis performs a mass reconstruction over an event sample of ≈ 4.9 million triggered Υ events.

The candidate e^+e^- pairs are sorted into signal pairs (e^+e^-) and background pairs (e^+e^+ and e^-e^-). The methods of electron identification for the invariant mass study include the TPC (3.4 x $10^{-6} \leq$ dE/dx $\leq$ 5.0 x $^{-6}$ keV/cm), TPC tracks which project onto the BEMC (p/E $<$ 2 GeV/c), and the $\mathrm{BPRS}_{ADC} > 65$ electron cut, as was defined in the conclusion of the rough calibrations Section 3.3.

The use of an SMD shower profile cut is not used in this analysis, as it provided little added advantage for electron discrimination in the high-multiplicity environment. The candidate 'signal' e^+e^- pairs will be made within the 'same event' while background e^+e^- pairs will be formed 'across events' (also called 'mixed-events'). The background distribution will have a 'smoother' shape via access to increased

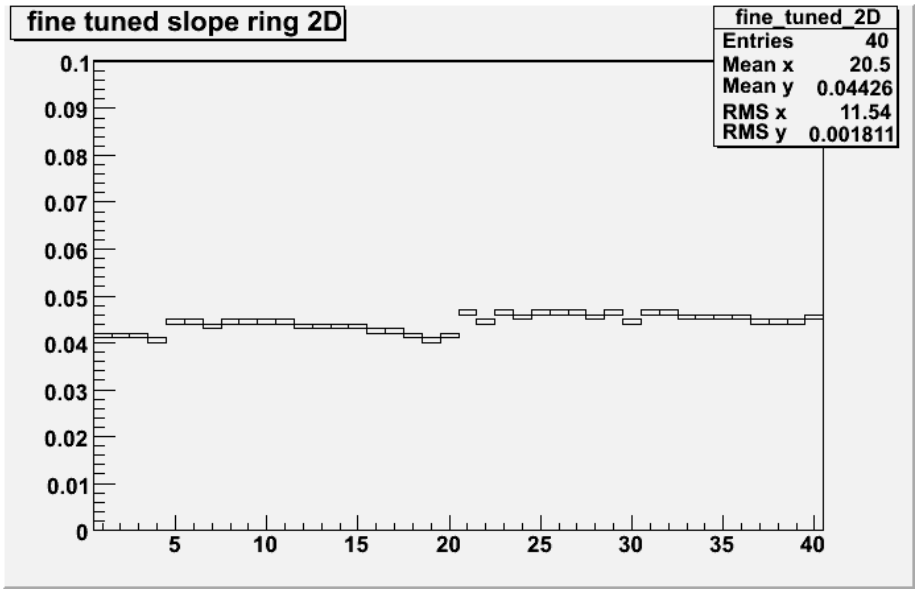

Figure 3.28: Au+Au 2007 MinBias: The ADC_{BPRS} spectrum slopes of all Rings after calibrating (slope method) to the reference slope of Ring 10.

statistics (reduced errors), but 'jet correlations' are thought to be inherent with this method and further investigation would be required. Figure 3.30 shows the invariant mass distribution for unlike-sign e^+e^- pairs (black distribution) and the mixed-event background e^+e^- pairs (red distribution), using dE/dx and p/E electron identification only. Qualitatively it can be seen that the signal to background (S/B) region in the vicinity of the Υ mass region has a value of S/B $\approx$ 2/1. Additional electron identification via the use of a $\mathrm{BPRS}_{ADC} > 65$ cut can be used to possibly enhance the S/B ratio in the mass distribution. Figure 3.31 shows the invariant mass distribution for unlike-sign e^+e^- pairs (black distribution) and mixed-event background e^+e^- pairs (red distribution), using the electron identification of dE/dx, p/E, and in addition, the BPRS. Again, it can be qualitatively seen that the S/B region in the vicinity of the Υ mass region using dE/dx, p/E, and now in addition, the BPRS

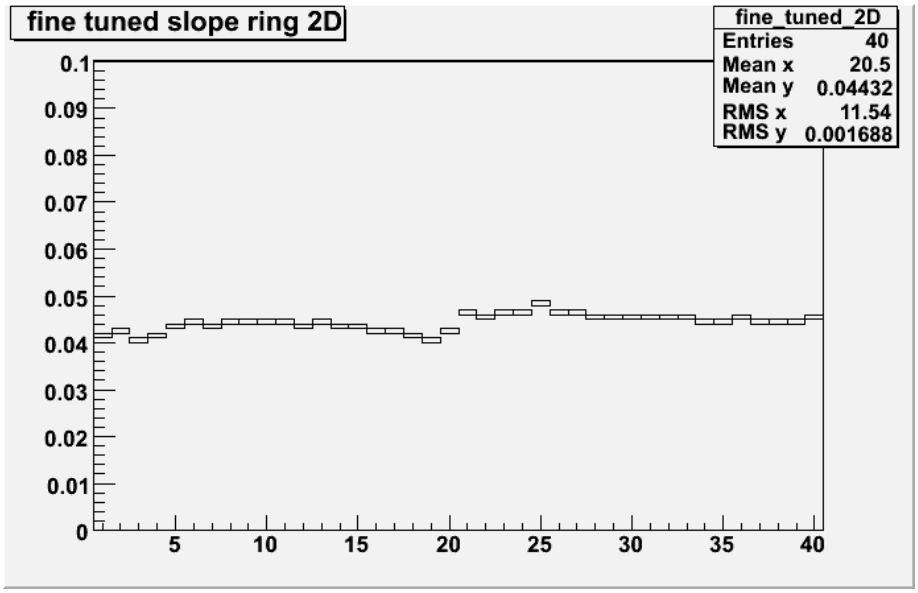

Figure 3.29: Au+Au 2007 MinBias: The ADC_{BPRS} spectrum slopes of all Rings after calibrating (area method) to the reference slope of Ring 10.

also results in a ratio of S/B $\approx$ 2/1. While the the use of BPRS as an electron identification tool in Au+Au collision should be effective in principle, the reduction in the yield is not conducive to an already statistically low measurement.

It is concluded that, while the relative BPRS calibration does appear to be of potential help, the measurement of Υ in Au+Au suffers statistically and prevents concrete conclusions from being made. The use of Run-7 Au+Au for J/ψ reconstruction with the proper BPRS calibration provides the next test for the use of the BPRS as an electron identification tool, shown in the next section.

3.5.2 BPRS and J/ψ in Au+Au

The effect of a calibrated BPRS cut on the reconstructed invariant J/ψ mass peak in the Run-7 data set[4] is scrutinized. It is important to note that the J/ψ peak

[4]There was not a triggered stream, but future runs will use a High Level Trigger (HLT) in STAR.

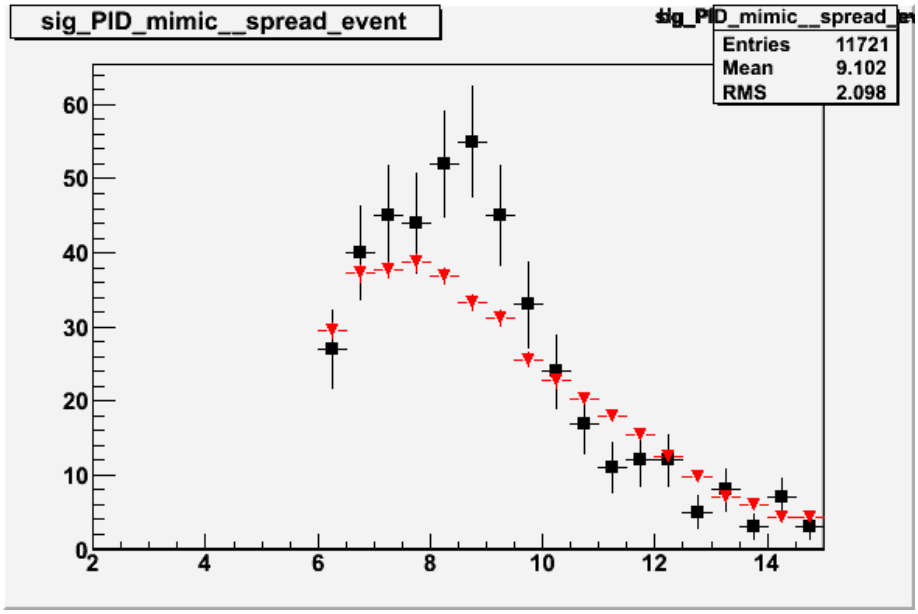

Figure 3.30: Au+Au 2007 Upsilon triggered events: The invariant mass spectrum for unlike (black) and mixed-event background (red) pairings without BPRS electron identification.

presented here is in fact not the full statistical sample available[5].

The J/ψ reconstruction is performed via the constraints: primary tracks must use $N_{FitPoints} > 25$, $N_{FitPoints}/N_{MaxPoints} > 0.55$, $|\eta| < 1$, with both tracks come from the same vertex within a distance of closest approach (DCA) < 1.0 cm and having $p_T > 1.2$ GeV/c. The electrons must also pass electron identification p/E < 2 GeV/c and the Bichsel-constraints of $|n\sigma_e| < 2$, $|n\sigma_k| > 2$, $|n\sigma_p| > 2$, $n\sigma_\pi$ < -3 or $n\sigma_\pi > 2.5$. The energy condition of the towers must satisfy $E_{cluster} > 0$, with the center tower of the 3x3 cluster having the highest energy deposition. Figure 3.32 shows the invariant mass spectrum for unlike-sign (black) and like-sign pairs (red) when no BPRS electron identification is used. The J/ψ unlike-sign (black) mass peak is vaguely visible

[5]Only production 2007 MinBias triggers 20003 and 20013, totaling approximately 30 million events are used

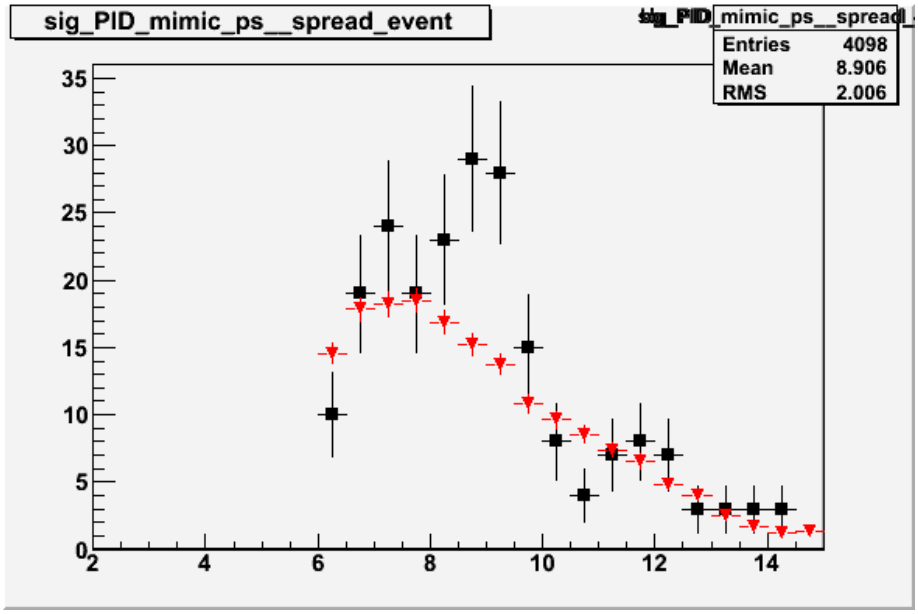

Figure 3.31: Au+Au 2007 Upsilon triggered events: The invariant mass spectrum for unlike (black) and like-sign (red) pairings with BPRS electron identification.

in the known mass-window, sitting on top of a very large background (red). The reconstructed J/ψ peak sits on a high level of observed background, requiring the use of a combinatorial background subtraction method using like-sign pairs. Figure 3.33 shows the subtracted invariant mass spectrum, where the combinatorial background was normalized by the geometrical mean, following the prescription: N = N_{+-} - $2\sqrt{N_{++}N_{--}}$. The J/ψ mass peak is visible, but the statistical fluctuations make it difficult to claim anything substantive. However, the underlying reason for looking at the J/ψ mass peak however is to test the functionality of the BPRS electron identification in the high-multiplicity environment of Au+Au collisions. Figure 3.34 shows the same invariant mass spectrum for unlike-sign (black) and like-sign pairs (red) when the BPRS electron identification is used. Again, the J/ψ unlike-sign (black) mass peak is visible in the known mass window and sitting on top of very large

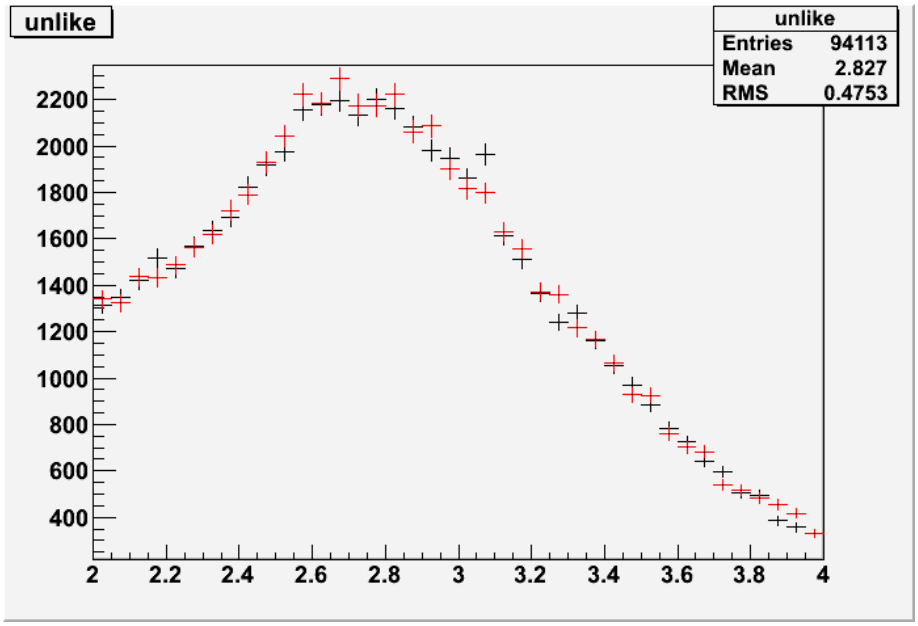

Figure 3.32: Au+Au 2007 Minimum Bias events: The invariant mass spectrum for unlike (black) and like-sign (red) pairings without BPRS electron identification.

backgrounds (red). The same combinatorial background subtraction method using like-sign pairs is performed and a subtracted invariant mass spectrum is generated. Figure 3.35 shows the subtracted invariant mass spectrum for the case of electron identification using the BPRS. The BPRS's effect on the J/ψ mass peak is visible, though, with a statistically depleted spectrum and the level of fluctuations present, it is not sufficient to form any type of concrete conclusion. What can be qualitatively stated is that the J/ψ mass peak is not completely destroyed by the BPRS cut, but that the BPRS does not appear to give us a significant gain in the S/B region in its current configuration.

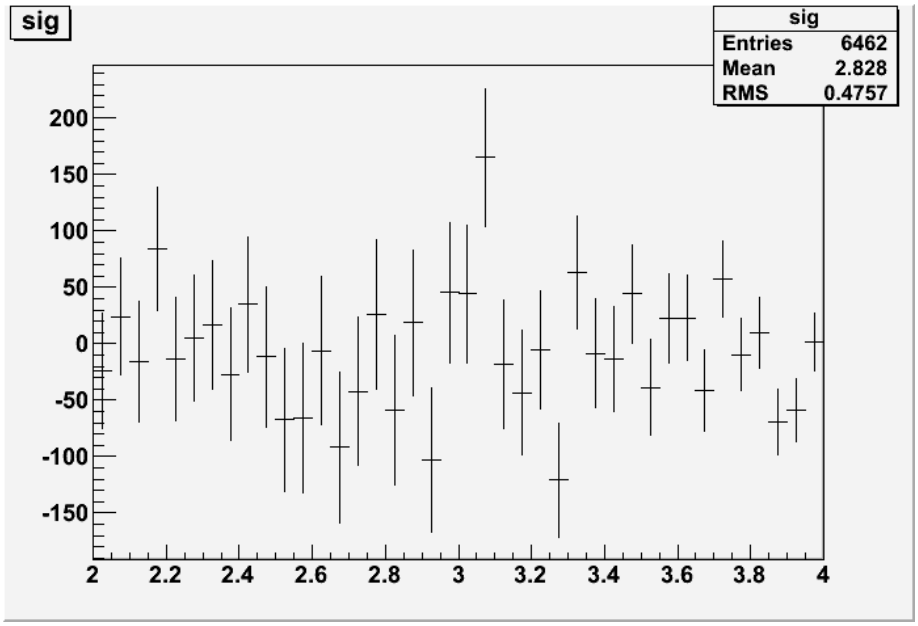

Figure 3.33: Au+Au 2007 Minimum Bias events: The subtracted invariant mass spectrum for J/ψ without BPRS electron identification.

3.6 Preshower Conclusion

Three separate electron-based analyses using the electron identification capabilities of the Barrel Preshower detector have been presented. The strongest and most convincing case was the initial study presented in Section 3.3, utilizing a roughly calibrated BPRS using 'harsh' ADC > 65 cuts that were safely into and beyond the electron-rich rein of the ADC spectrum versus the other means of electron identification available in STAR - dE/dx, SMD, p/E, and BPRS. It was concluded from that analysis that the BPRS held the most potential when it came to the rejection of hadronic backgrounds and electron identification. The next use of the BPRS incorporated the roughly calibrated (harsh ADC > 65 cut) BPRS detector with the Au+Au Upsilon triggered data (Section 3.2). Reconstructing the $\Upsilon \rightarrow e^+e^-$ it was found that

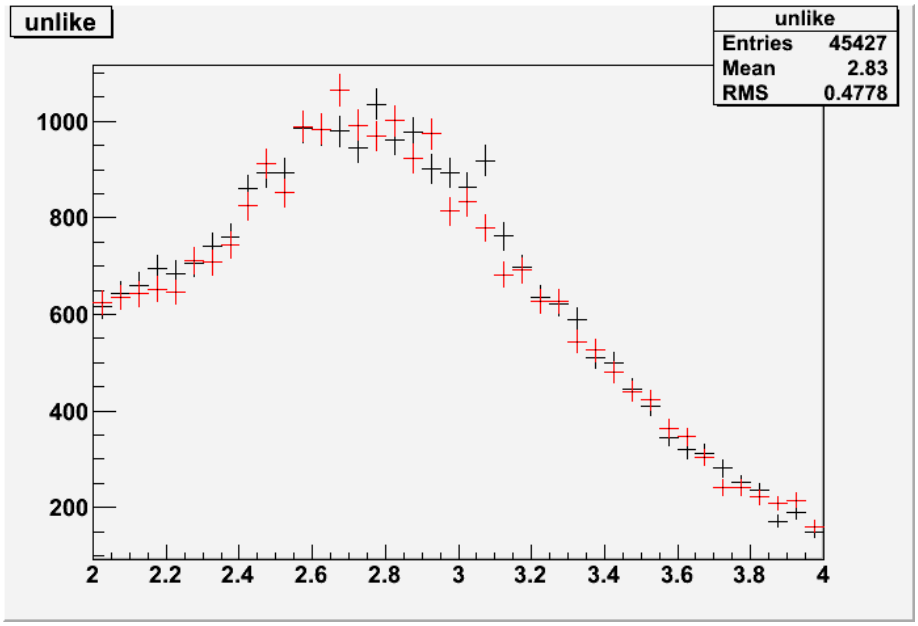

Figure 3.34: Au+Au 2007 Minimum Bias events: The invariant mass spectrum for unlike (black) and like-sign (red) pairings with BPRS electron identification.

in an already statistically-starved measurement did not stand to benefit from use of the BPRS, especially considering the current state of the functional/working fraction of the BPRS in this data set. While the rough BPRS calibration has been shown to be of potential help in electron identification, the use of the BPRS in measurements on Υ in Au+Au suffers statistically and the S/B before and after BPRS remains approximately equivalent, thus no decisive conclusions may be drawn. Lastly, an analysis was initiated using the refined calibration of the BPRS in Au+Au data (Section 3.4) for J/ψ reconstruction. Again, while the proof-of-principle for electron identification does exist, the analysis again succumbs to the lack of statistical significance of the reconstructed J/ψ sample. The J/ψ signal to background is again neither increased nor decreased, making it impossible to make a more definitive statement than saying that it has the potential to be play an important role in electron identification in

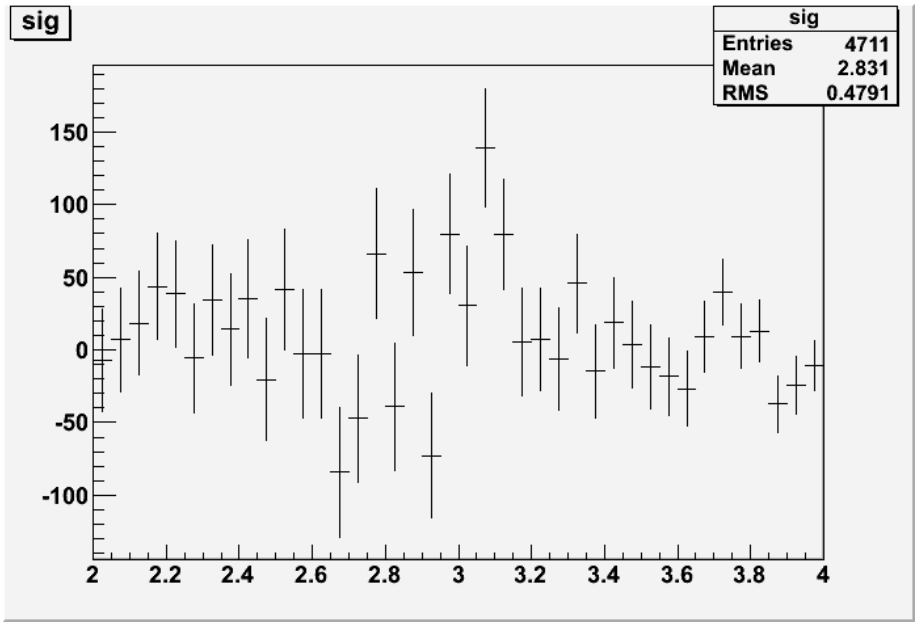

Figure 3.35: Au+Au 2007 Minimum Bias events: The subtracted invariant mass spectrum for J/ψ with BPRS electron identification.

STAR.

This was the first attempt at using the BPRS in STAR, and while the results in Υ and J/ψ reconstruction using the electron identification of the BPRS is not convincingly useful, it should be pointed out that the BPRS will be more effective in later runs, as much more of the detector is operational - approximately 90+% BPRS channels are known to be operational for Run-8 (2008) and hopefully Run-10 (2010). The power of the BPRS could be in Run-10 Au+Au collisions.

4. DATA ANALYSIS AND RESULTS

This chapter is dedicated to a detailed description of Upsilon (Υ) reconstruction, the study of the Υ(nS) [n = 1, 2, 3] line-shape, and the measurements of the production-related observables proposed in Section 1.12. The high signal to background ratio (S/B) in Υ at STAR makes it practical to investigate the Υ production mechanism.

The spin-alignment (polarization) measurement of the Υ is defined by the observable associated with e^+ daughter coming from the $\Upsilon \rightarrow e^+e^-$ decay, in the center-of-mass frame. Appropriate Lorentz boosts will allow for the calculation of the cos(θ) value of the e^+ daughter in the Υ center-of-mass frame. The raw cos(θ) distribution will be corrected (see Section(4.6. 4.6.1)) and fit with a polynomial of second-order, and then compared to the values of the polarization parameter (α) predicted by CSM and COM production.

The Υ + h correlation measurement looks for a presence of hadronic activity directly around[1] the reconstructed Υ. The activity (or lack thereof) is the key measure from which a statement about the nature of the gluon radiation emitted off of the colored, heavy ($b\overline{b}$) quark-pair during production may be postulated. The azimuthal correlations between the Υ and charged hadrons (in data) will then be calculated and compared to simulations based on the PYTHIA[2] framework. The PYTHIA simulation[3] is used in an attempt to decompose the observed correlation shape (in data) into the contributions arising from the predicted gluon activity during CSM and COM production.

[1] Measured in space coordinates around the Υ.
[2] All discussion on PYTHIA refer to the PYTHIA 8.1 C++ rewrite [63].
[3] Future measurements may possibly study a 'tuned' event generator, 'MADonia' [51].

4.1 Upsilon Reconstruction via e^+e^-

The STAR detector historically limits lepton-based analyses to the electron only, and thereby analyses involving Υ reconstruction are restricted to the di-electron (e^+e^-) decay channel. While the STAR experiment is pursuing the working implementation of a muon-capable detector, the Muon Telescope Detector (MTD), at the time of the collection of the data used in this thesis, the $\Upsilon \rightarrow \mu^+\mu^-$ reconstruction was not[4] possible. Hence, muons are not used in any aspect of the Υ analyses which are presented here, but future STAR runs will certainly make use of $\Upsilon \rightarrow \mu^+\mu^-$ (di-muon decay channel). Working under the constraint of reconstructing the Υ with a single mode (and relatively small branching fraction) places increased emphasis on the need for an efficient 'selection' of those events in which an Υ may have likely been created.

4.2 Event Selection

The positions of the vertices used for event reconstruction will lie along the $\pm$z-position in the STAR coordinate-system. The vertex positions of all candidate events[5] will satisfy a primary vertex z-coordinate position (V_z), which is located within some distance of the predefined STAR interaction-point ($V_z = 0$ [cm]). As such, accurately locating the positions of vertices is essential to any reconstruction analysis, whether being primary-vertices or secondary-vertices. The environment created by high bunch crossing-rates and high multiplicity of colliding species at $\sqrt{s} = 200$ GeV only exacerbates the necessity for accurate vertex finding. Rigorous STAR vertex-finding algorithms [57] are in place during data collection at STAR, and the critical information from those vertex-finding algorithms are made available

[4]The MTD was not fully operational during the taking of Run-8 and Run-9 data.
[5]$\Upsilon \rightarrow e^+e^-$ are formed from this set.

to the analyst. Choice of vertices in an event are typically made using the vertex-associated quantities known as 'index' and 'rank'. Rank and index parameters are the constraints implemented in determining the quality of a vertex during vertex selection in any given analysis. Only Rank = 0 and Index = 0 vertices are kept when performing this analysis. Standard procedure in STAR is to keep Υ reconstruction vertex positions at $|V_z| \leq 40$ [cm], and this analysis does not deviate from this standard. Figure 4.1 shows the $|V_z|$ distribution for each reconstructed Υ candidate over the full TPC range in $\pm$z. In this Υ analysis, all vertices must lie within $|V_z| \leq 40$ [cm] of the STAR interaction-point.

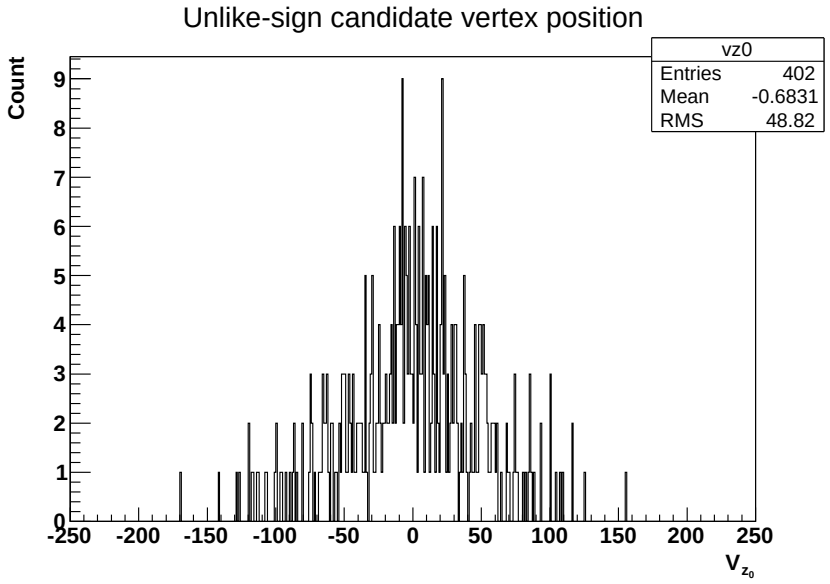

Figure 4.1: Primary vertex location (V_z [cm]) in Run-9 along $\pm$z for $\Upsilon \rightarrow e^+e^-$ candidates in STAR.

While the large acceptance of STAR does allow accommodate large data collection

of the particles created during the relativistic collisions, it is not entirely sufficient to rely on the large acceptance of they STAR detector alone (see Chapter 2). The capability for Υ detection at STAR is enhanced by employing a dedicated Υ - triggering algorithm[6], described in the following sections. The Υ-trigger in STAR is a tiered, bi-level, 'high tower' setup dedicated to making quick selections on events that have the signature of a massive two-body Υ decay. The large invariant mass of the Υ lends itself to designing the algorithm to impose a topological/geometrical criteria based on the large opening-angle of its (heavy) two-body decay. The data used in this analysis is selected using both Level-0 (L0) and Level-2 (L2) triggers. The bi-level component structure of the Υ-trigger at STAR is independently referred to as the L0 and L2 triggers, and are briefly discussed in the next sections.

4.2.1 L0 trigger

The L0 trigger is a fast hardware-level decision, designed to execute an 'acceptance decision' on the timescale of RHIC bunch crossings. The L0 trigger is a 'high-tower' (HT) trigger that checks for the condition that at least one BEMC tower has an ADC value above a pre-defined threshold, where the precise threshold value varies from run to run. Table 4.1 summarizes the L0 threshold values used in STAR. If the L0 HT threshold is satisfied during an event, then the L0 trigger passes the event to the L2 tier, where the L2 trigger is then initiated.

4.2.2 L2 trigger

The L2 trigger is a software-level decision, designed to find towers with an energy that are similar to the L0 threshold energy. The L2 decision is based on the result of a fast search for an energy deposit (see Table 4.1 for threshold energies) in the calorimeter towers - if a tower is found, then it is uses the tower as a 'seed' to

[6]PSN0511: Extending the Physics Reach of STAR: Prospects for the Measurement of Quarkonia.

Table 4.1: Upsilon L0 and L2 trigger in STAR.

Run- (Year)	**System**	**Trigger ID**	**L0**	**L2**
Run-6 (2006)	p+p 200 GeV	117602	HT > 12	$E_1 > 4.0$ GeV $E_2 > 2.5$ GeV $6 < M < 15$ GeV/c^2 $\cos\theta < 0.5$
Run-6 (2006)	p+p 200 GeV	137603	HT > 16	$E_1 > 4.0$ GeV $E_2 > 2.5$ GeV $6 < M < 15$ GeV/c^2 $\cos\theta < 0.5$
Run-7 (2007)	Au+Au 200 GeV	200601	HT > 18	$E_1 > 4.0$ GeV $E_2 > 2.5$ GeV $6 < M < 20$ GeV/c^2 $\cos\theta < 0.0$
Run-7 (2007)	Au+Au 200 GeV	200602	HT > 18	$E_1 > 4.0$ GeV $E_2 > 2.5$ GeV $6 < M < 20$ GeV/c^2 $\cos\theta < 0.0$
Run-8 (2008)	d+Au 200 GeV	210601	HT > 18	$E_1 > 4.5$ GeV $E_2 > 3.0$ GeV $6.5 < M < 25$ GeV/c^2 $\cos\theta < 0.0$
Run-9 (2009)	p+p 200 GeV	240641	HT > 18	$E_1 > 4.5$ GeV $E_2 > 3.0$ GeV $5 < M < 20$ GeV/c^2 $\cos\theta < 0.0$

form L2 clusters. The definition of a L2 cluster is a group of 3 towers, composed of the seed tower plus the 2 surrounding towers having the highest energy. The L2 algorithm takes these pairs of clusters and calculates the invariant mass, under the approximation $M \simeq \sqrt{2E_1E_2(1-cos(\theta_{12}))}$, where E_i (i = 1,2) is the cluster energy and θ_{12} is defined as the angle formed by the two approximately straight lines, extending from the vertex to the position of the cluster. Upon calculating the

invariant mass, a check against a predefined upper- and lower-limit mass acceptance is performed (see Table 4.1). The approximation of a straight line is valid under the known electron/positron from large energy Υ decay, the decay kinematics of the Υ daughters, and the STAR magnetic field strength. The primary vertex from the decay is then defined as the intersecting point in the STAR coordinate-system to which the known positions of the L2 clusters extrapolate, under the straight line approximation. The L2 decision is required to pass one final condition - a topological check. The topological check requires that the angle between L0 and L2 lays within a pre-specified azimuthal range; the angular separation between L0 and L2 towers (cluster) must be at least $\pi/6$, which corresponds to a minimum $cos(\theta_{12})$ opening angle (see Table 4.1). As previously mentioned, these large opening angles at sufficiently high transverse momentum are indicative of a heavy, two-body decay and the L0-L2 triggering algorithm can be optimized to take advantage of the large geometrical acceptance and for speed (relative to the RHIC bunch crossing-rates). Table 4.2 provides additional information for the run numbers and total integrated luminosities.

Table 4.2: Data: Run, collision system, Trigger ID, run number, and integrated luminosity.

Run-	**System**	**Trigger ID**	**Run numbers**	**Luminosity**
Run-6	p+p 200 GeV	117602	7090046-7129065	3.61692 pb^{-1}
Run-6	p+p 200 GeV	137603	7133052-7156028	5.61695 pb^{-1}
Run-7	Au+Au 200 GeV	200601	8103029-8113068	73.66 μb^{-1}
Run-7	Au+Au 200 GeV	200602	8113102-8177038	502.12 μb^{-1}
Run-8	d+Au 200 GeV	210601	8346052-9027087	32.66 nb^{-1}
Run-9	p+p 200 GeV	240641	10117085-10180030	21.563 pb^{-1}

4.3 Track Selection

Tracks are defined by rigorous reconstruction algorithms used during the STAR 'offline production' phase of the experiment, as defined by ITTF[7]. The TPC hits allow for the associated, time-ordered helices to be calculated. The choice in the number of 'fit points' required during the helix-fit is one of the parameters that specifies the overall quality of a reconstructed track. The helix-fit corresponds to a physical trajectory of a charged track and allows for the quantification of the physical characteristics (e.g. $\vec{p}$, dE/dx, charge, etc.). As a default for accepting quality tracks in this analysis, all reconstructed tracks used during the reconstruction of the event are 'good TPC-tracks[8]' as defined by ITTF, and were taken from the sample of tracks that STAR classifies as 'global' tracks. The definition of a global track may be understood by sub-dividing tracks into two major classifications: 1) global tracks and 2) primary tracks, and it is important to differentiate between global and primary tracks from the onset of this analysis. In particular, to impose an extra condition on any given global track can be the requirement to have an extra 'anchor point' be used during the helix-fitting procedure. In other words, the helix assigned to a primary track is forced to go through an extra fit-point during the helix fitting procedure. The location of the extra fit-point used is defined as the primary vertex of that track. If this extra vertex-fitting constraint is imposed, then the track is defined as a 'primary' track. Both primary and global tracks are used in the analyses, and the appropriate level of differentiation is used depending on the type of track (primary or global) used during the relevant analysis.

The daughter electron tracks from any candidate Υ are required to be primary tracks (projecting back to a primary vertex position). By definition, the primary

[7]STAR Integrated Tracker Task Force.
[8]ITTF denotes this as a track with flag = 301.

track helix must extrapolate back to the location of its primary vertex, and during the 'pairing' of these primary tracks (candidates identified as e^+ and e^- or $e^+e^+ + e^-e^-$), the condition is that each member of any given pair must extrapolate back to the same primary vertex as the other member (track) belonging to that pair. This 'distance of closest approach' (DCA) between the Υ daughters stipulates that the daughter tracks are coming from the primary decay vertex of the Υ. The identification of electrons used for Υ reconstruction is developed in the following sections.

4.3.1 Electron Selection

Electron-based analyses (e.g. $\Upsilon \rightarrow e^+e^-$ reconstruction) rely on strong electron identification. Recall the main selection platform for identifying electrons is twofold: 1) the Time Projection Chamber (TPC) and 2) the Barrel Electro-Magnetic Calorimeter (BEMC[9]). In the Υ reconstruction phase of this analysis, the particle identification tools within the STAR TPC platform are further tailored to select electron-rich ($e^{\pm}$) samples of charged tracks. The next section provides a description of the electron criteria used for Υ reconstruction.

4.3.1.1 Identification: dE/dx

The quality of a dE/dx calculation from the TPC information is contingent upon the number of fit points used during the reconstruction of a 'good track.' The Υ reconstruction presented here uses, as a prerequisite, only those primary tracks with a number of fit points (TPC hits) greater than 20. I.e. the assigned dE/dx value for the track will only be allowed into the analysis if the $N_{hits}^{TPC} > 20$ condition is satisfied. Electron candidates ($e^{\pm}$) used during Υ reconstruction must fall within an

[9]The BEMC can be used to trigger (L0 and L2) on events that are possibly more interesting, from the perspective of the Heavy Flavor working group at STAR.

electron-rich dE/dx sector (upper- and lower-bounds in dE/dx): 3.0 x 10^{-6} $\leq$ dE/dx $\leq$ 5.0 x $^{-6}$ keV/cm.

The tracks that passed the loose cut of 3.0 x 10^{-6} $\leq$ dE/dx $\leq$ 5.0 x $^{-6}$ keV/cm were then used to form pairs[10] - pairs that were then used during the reconstruction of the Υ candidates ('candidate pairing'). The resulting sample of candidate pairs formed is only the initial step in reconstructing the invariant mass of an Υ candidate. The next step is to refine the reconstruction, attempting to minimize false Υ reconstructions (candidate electron pairs which are inadvertently formed, due presence of hadrons having dE/dx values in the electron dE/dx region). Figure 4.2 shows the dE/dx vs. p_T for each of the unlike-sign electron candidate pairs ($e^{\pm}$) used for the Υ reconstruction, using the 'loose' dE/dx cut. Figure 4.3 shows the dE/dx vs.

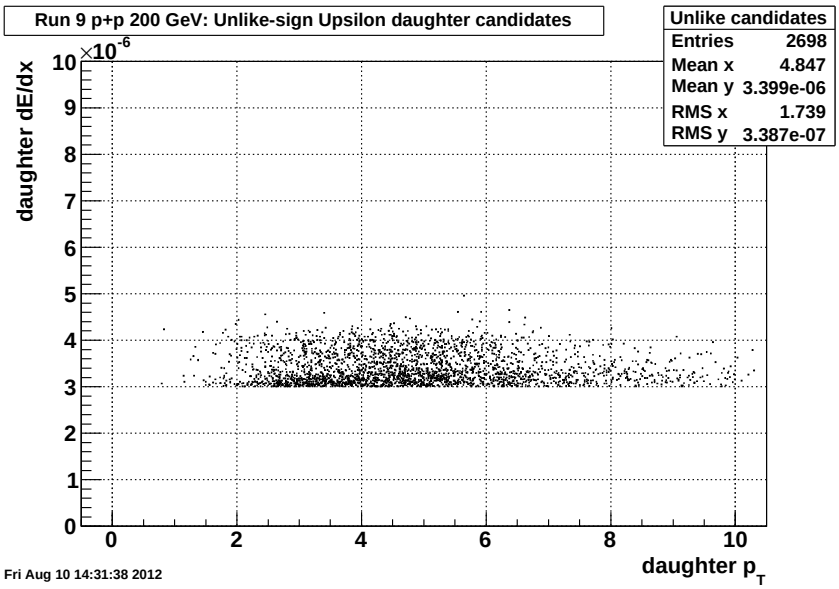

Figure 4.2: dE/dx vs. p_T distribution in Run-9 for unlike-sign e^+e^- daughter candidates.

[10]Pairs are defined as charged pairs coming in four types: + -, - +, + +, - -.

p_T for each of the like-sign electron candidate pairs (e^{++} or e^{--}) used for the Υ reconstruction, using the 'loose' dE/dx cut.

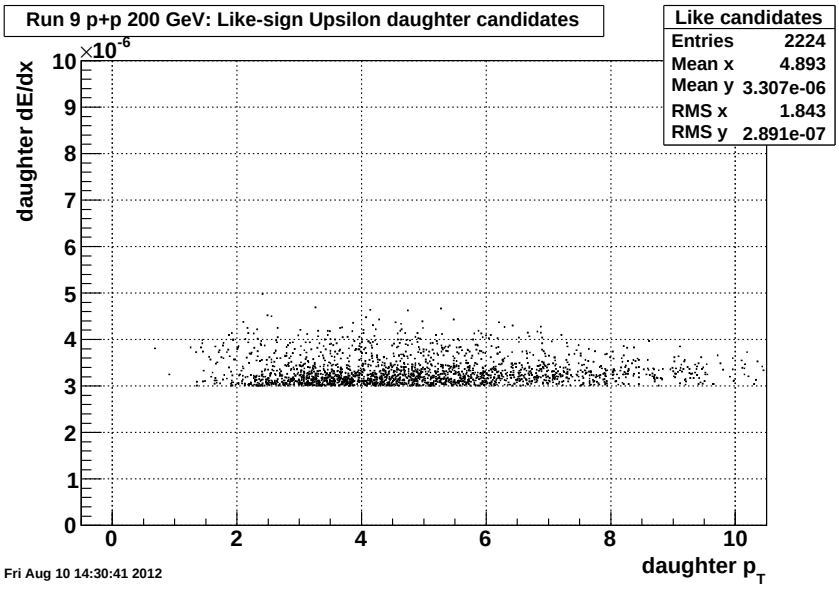

Figure 4.3: dE/dx vs. p_T distribution in Run-9 for like-sign daughter candidates.

Tighter dE/dx constraints and additional electron identification methods were considered. In particular, the electron daughter candidates are further constrained to lie within a tightened sector of the dE/dx distribution: 3.4 x 10^{-6} $\leq$ dE/dx $\leq$ 4.7 x $^{-6}$ keV/cm. Figure 4.4 shows the dE/dx vs. p_T for all unlike-sign pairs of electron candidates ($e^{\pm}$) that were used for Υ reconstruction, after the application of a 'tight' dE/dx cut. It is relevant to note that the like-sign pairs of electron candidates (e^{++} or e^{--}) will be used to subtract the contribution from random electron pairs (r.e.p.) from the unlike-sign reconstructed Υ distribution. Figure 4.5 shows the dE/dx vs. p_T of these like-sign pairs. Table 4.3 catalogues the dE/dx cuts

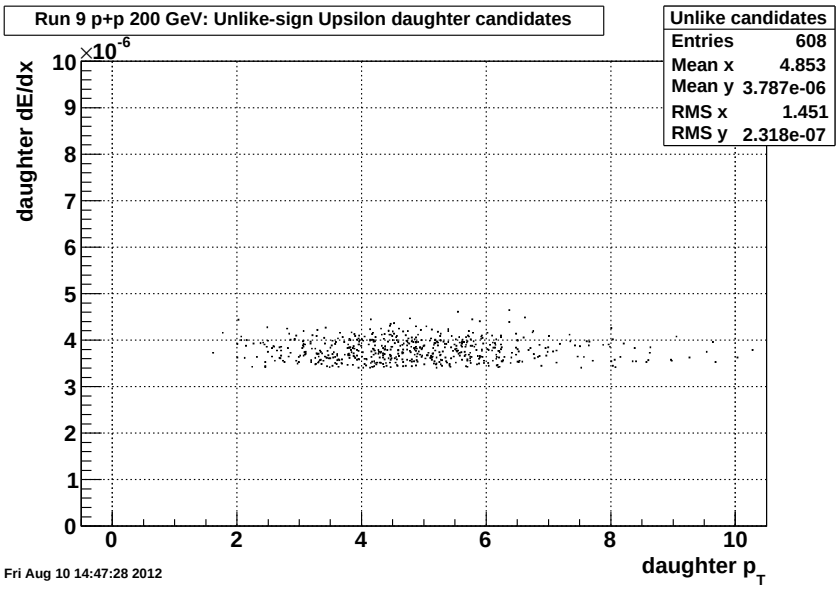

Figure 4.4: 'Tight' dE/dx vs. p_T distribution in Run-9 for unlike-sign e^+e^- daughter candidates.

used in electron selection during the Υ reconstruction in Run-8 and Run-9. The next section discusses an additional electron identification method that is used increase the likelihood that the track sample is electron-rich.

4.3.1.2 Identification: p/E

The 'loose' selection of the dE/dx region (likely composed of electron candidates, but inherently subject to hadron contamination) have their helices projected onto the BEMC, whereupon the energy deposition in the BEMC tower(s) is measured. The projection of the track (electron candidate) is then compared to the TPC-measured momentum value by the forming of the ratio p^{TPC}/E^{tower}. The choice of electron selection via p^{TPC}/E^{tower} is considered accordingly[11].

Using the reconstructed Υ candidates from electron pairs that fell within the

[11] Ch. 2 Experimental Apparatus.

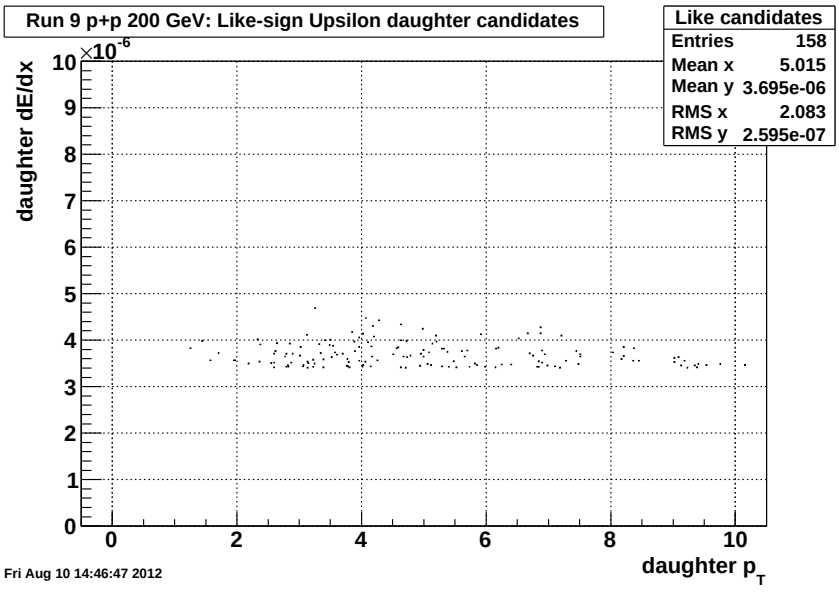

Figure 4.5: 'Tight' dE/dx vs. p_T distribution in Run-9 for like-sign daughter candidates.

'tight' subset of the dE/dx region, the energy from those projected tracks was measured and the p^{TPC}/E^{tower} distribution was observed. Figure 4.6 shows the p^{TPC}/E^{tower} distribution of the unlike-sign pairs that have passed the tight dE/dx constraint.. The discussion from a previous Chapter/Section on the behavior of p^{TPC}/E^{tower} distributions for hadron-like vs. electron-like particles, a cut of $0.7 < p^{TPC}/E^{tower} < 1.7$ is quickly implemented. Figure 4.7 shows the p^{TPC}/E^{tower} distribution of the unlike-sign pairs after the cut of $0.7 < p^{TPC}/E^{tower} < 1.7$ is applied. Table 4.3 catalogues the p^{TPC}/E^{tower} cut used in electron selection during Υ reconstruction.

Table 4.3: Selection cuts for $e^{\pm}$ tracks during Υ reconstruction.

Electron Candidate Identification	**Cut value**	**Units**
Loose dE/dx cut	[3.0,5.0]	[keV/cm]
Tight dE/dx cut	[3.4,4.7]	[keV/cm]
Loose p/E cut	(2.0,5.0]	[1/c]
Tight p/E cut	(0.7,1.7)	[1/c]
'OR' BSMD cut	$\eta_{\#strips} > 1$ or $\phi_{\#strips} > 1$	
'AND' BSMD cut	$\eta_{\#strips} > 1$ and $\phi_{\#strips} > 1$	

4.4 Upsilon Selection

The requirements placed on the identification of electrons used for Υ reconstruction was developed in the previous sections. With all vertex selections and particle identifications, the invariant mass spectrum for unlike-sign and like-sign events is presented. Figure 4.8 hows the calculated invariant mass distribution for unlike-sign and like-sign pairs in Run-9 p+p data. Figure 4.9 shows the calculated invariant mass distribution for unlike-sign and like-sign pairs in Run-8 d+Au data. The like-sign pairs were used in conjunction with the unlike-sign pairs to extract the random electron pair background contribution from the Υ invariant mass spectrum via N = N_{+-} - $2\sqrt{N_{++}N_{--}}$. A point of interest in the mass spectrum will be the choosing of a mass-window (8-10.5 GeV/c in Run-8 d+Au, and 8-11.5 GeV/c in Run-9 p+p), used during the production-related measurements[12]. The production related measurements are restricted to a 'narrow' mass region, which serves to maximize the purity of the reconstructed sample. In each of the mass figures, the entries between the blue vertical bars denote this S/B region. This region used in measuring the Υ

[12]This is justified, because each of the production based measurements are independent of the total production cross-section.

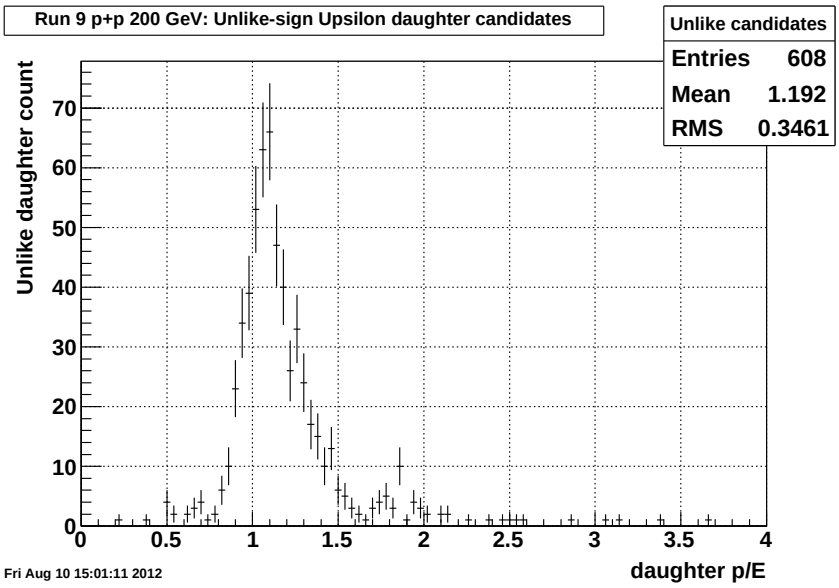

Figure 4.6: p/E distribution in Run-9 for unlike-sign e^+e^- daughter candidates.

production related yields a S/B = 247/43 $\approx$ 5.74 $\pm$ 0.95 in Run-9 p+p data, and a S/B = 142/28 $\approx$ 5.07 $\pm$ 1.05 in Run-8 d+Au data. These S/B regions will later be used to study the observables related to Υ production.

It is noted that very little background is observed, even without the use of a combinatorial background subtraction using the like-sign pairs. The combinatorial background is normalized by the geometrical mean, via: N = N_{+-} - $2\sqrt{N_{++}N_{--}}$, where the yield may be extracted by an integration of the invariant mass distribution of Υ(1S+2S+3S), after the subtraction of the normalized like-sign pair distribution. Figure 4.10 shows the combinatorial background subtracted Υ signal in Run-9 p+p data.

Similarly, use of the like-sign pairs to subtract the contributions from combinatorial background in the unlike-sign p_T-distribution was performed. The figures represent the transverse momenta spectrum of the full mass spectrum, as it relates

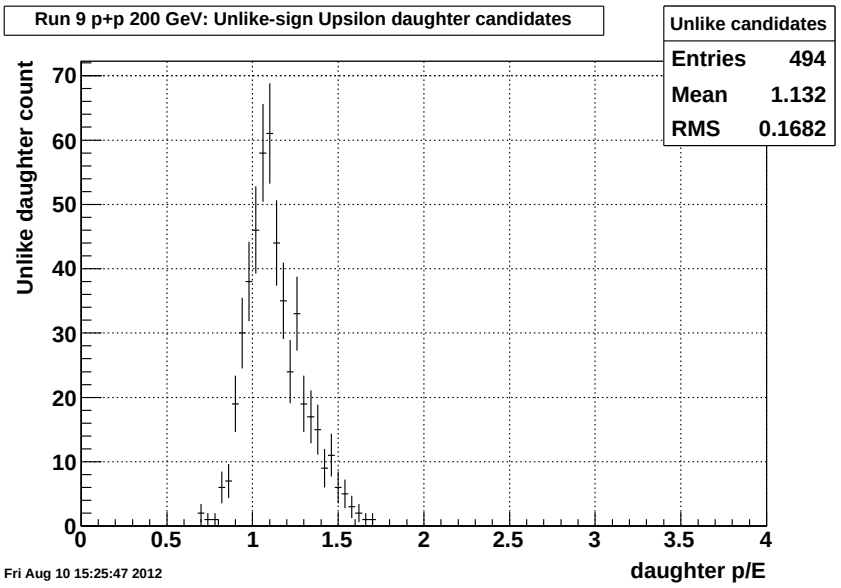

Figure 4.7: p/E distribution in Run-9 for unlike-sign e^+e^- daughter candidates.

to evaluating the Υ(1S+2S+3S) line-shape, but also the p_T-distribution of those candidates which fall within the 'mass-window' used to study the production-related measurements. Figure 4.11 shows the p_T-distribution for unlike-sign pairs (black) and like-sign pairs (red-fill) that lie within the mass-window of 8-11.5 GeV/c, in Run-9 p+p data. Figure 4.12 shows the p_T distributions for unlike-sign pairs (black) and like-sign pairs (red-fill) that lie within the mass-window of 8-10.5 GeV/c, in Run-8 d+Au data.

Figure 4.13 shows a 2x2 panel in Run-9 p+p data, with the upper-panels showing the unlike- and like-sign p_T-distributions, and the lower-panels showing the combinatorial background subtracted p_T-spectra. The left-column is the p_T-distribution for the pairings within the blue vertical bars (8-11.5 GeV/c), and the right-column is the p_T-distribution for the full range of mass pairings.

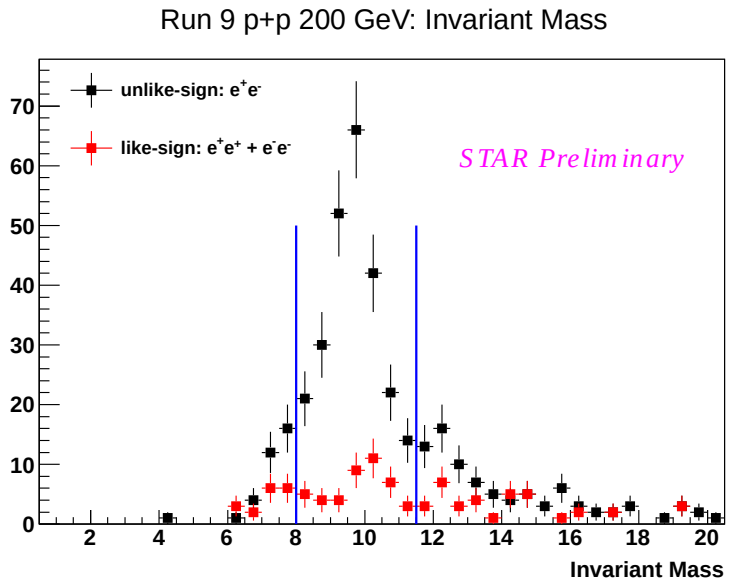

Figure 4.8: Invariant mass ($M_{inv.}$ $[GeV/c^2]$) distribution in Run-9 for unlike-sign (black) and like-sign (red) $\Upsilon \rightarrow e^+e^-$ candidate pairs in STAR. The blue vertical bars bound the region (8-11.5 GeV/c), where a S/B $\approx 5.74 \pm 0.95$ is observed.

4.4.0.3 Identification: BSMD

The use of electron identification with the STAR Barrel Shower Maximum Detector (BSMD) was also studied in the Υ reconstruction phase of the analysis. The shower profile for each of the daughter electron candidate pairs (e^+ and e^-) is plotted in Figure 4.14 as the number of η-strips ($\eta_{\#strips}$) vs. the number of ϕ-strips ($\phi_{\#strips}$) for three different BSMD configurations ('NULL', 'OR', and 'AND'). The same shower-profiling methodology will also apply to the like-sign candidate pairs (e^+ and e^+, or e^- and e^-), and so the like-sign SMD response is also included in the BSMD analysis-figures.

The default ('NULL') case is to observe the response of the SMD strips for the unlike-sign pairs used in the Υ reconstruction. These unlike-sign candidates in the

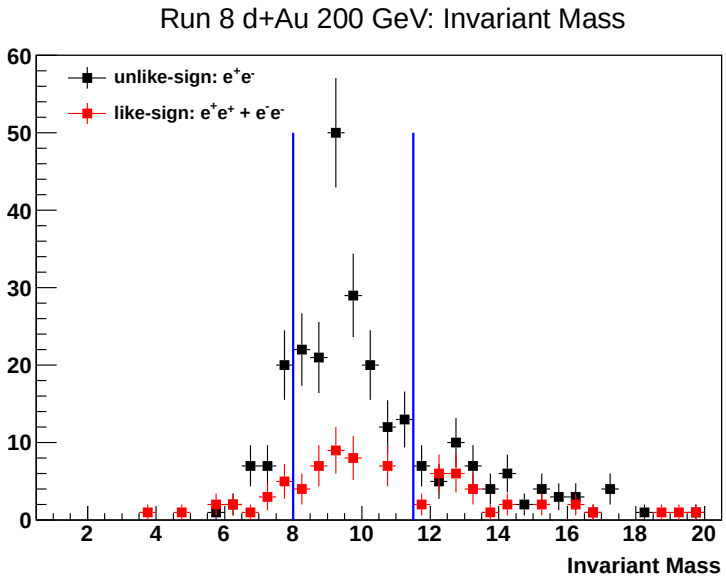

Figure 4.9: Invariant mass ($M_{inv.}$ $[GeV/c^2]$) distribution in Run-8 for unlike-sign (black) and like-sign (red) $\Upsilon \rightarrow e^+e^-$ candidate pairs in STAR. The blue vertical bars bound the region (8-10.5 GeV/c), where the S/B $\approx 5.07 \pm 1.05$.

NULL case are those candidates that passed the dE/dx ad p/E electron identification cuts. The two remaining BSMD configurations ('OR' and 'AND') will ideally facilitate an increase in hadron-rejection, and each case will be applied separately. The resulting BSMD shower profile was inspected and the overall effectiveness of the BSMD is gauged by comparing the S/B of the Υ mass spectrum within a mass-window of 8-11.5 GeV/c^2. Figure 4.14 shows the BSMD η- ϕ-response for the unlike-sign pairs which are used in the Υ reconstruction, as well as the BSMD η- ϕ-response for like-sign pairs, both in the 'NULL' case. Figure 4.8 shows the calculated invariant mass distribution for unlike-sign and like-sign pairs in Run-9 p+p data, for the NULL case (S/B = 247/43 $\approx 5.74 \pm 0.95$.).

In the first ('OR') case, if the electron-positron pair is to be used in the Υ reconstruction, then the electron and positron candidates must independently satisfy the

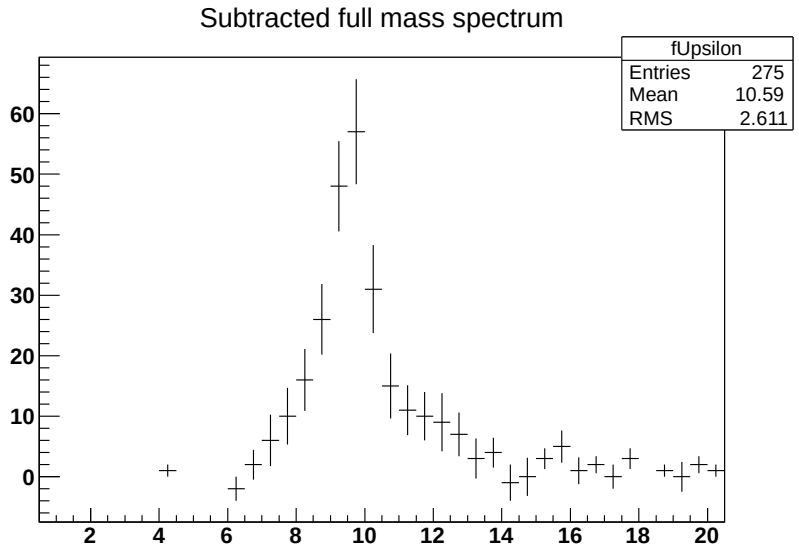

Figure 4.10: $M_{inv.}$ $[GeV/c^2]$ signal corrected for r.e.p. contributions using the combinatorial background subtraction method in Run-9 for $\Upsilon \rightarrow e^+e^-$ candidates in STAR.

condition $\eta_{\#strips} > 1$ or $\phi_{\#strips} > 1$. If either one of the candidate daughters does not independently pass either the $\eta_{\#strips} > 1$ or $\phi_{\#strips} > 1$ condition, then the pair is rejected and the invariant mass of the candidate is not calculated. Figure 4.15 shows the BSMD η- ϕ-response for the 'OR' condition for unlike-sign and like-sign pairs in the invariant mass spectrum (in the 8-11.5 GeV/c^2 mass-window), and the bulk of the individual daughters fall in the region where $\eta_{\#strips} > 1$ and $\phi_{\#strips} > 1$. Figure 4.16 shows the calculated invariant mass distribution for unlike-sign and like-sign pairs in Run-9 p+p data, for the 'OR' case (S/B = 220/41 $\approx$ 5.37 $\pm$ 0.91).

In the second ('AND') case, if the electron-positron pair is to be used in the Υ reconstruction, then the electron and positron candidates must independently satisfy the condition $\eta_{\#strips} > 1$ and $\phi_{\#strips} > 1$. If either one of the candidate daughters does not independently pass both the $\eta_{\#strips} > 1$ and $\phi_{\#strips} > 1$ conditions,

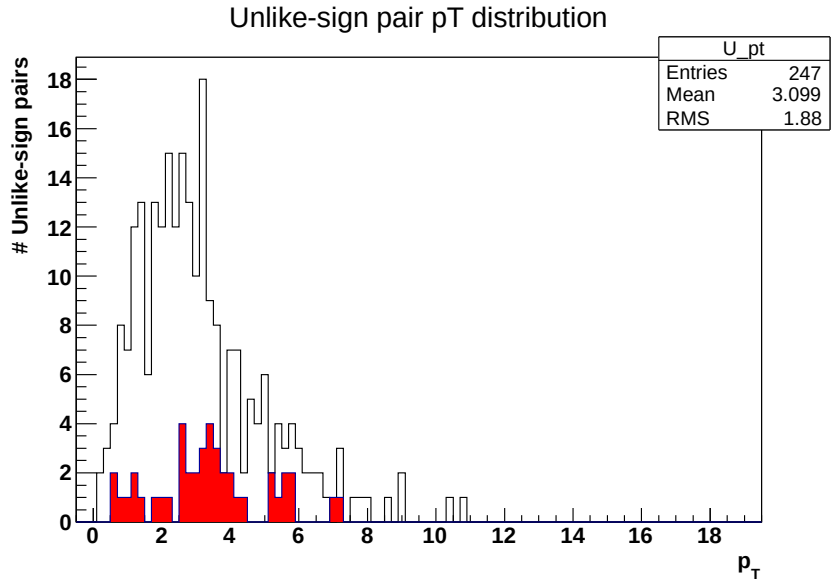

Figure 4.11: Transverse momentum (p_T [GeV/c]) of $\Upsilon \rightarrow e^+e^-$ candidates in Run-9 for unlike-sign (black) and like-sign (red) in STAR.

then the pair is rejected and the invariant mass of the candidate is not calculated. Figure 4.17 shows the SMD distribution for the 'AND' condition. Figure 4.18 shows the calculated invariant mass distribution for unlike-sign and like-sign pairs in Run-9 p+p data, for the 'AND' case (S/B = 115/18 $\approx$ 6.39 $\pm$ 1.62).

The value of the S/B ratio is chosen as the decisive *measuringstick* of the relative effectiveness of the BSMD cut on the preexisting electron identification cuts already in place, when reconstructing the Υ foreground and background. It is concluded from the S/B study, that the overall benefit of imposing a BSMD cut when reconstructing in the p+p data is minimal and therefore the BSMD cut does more to deplete the Υ sample than it does to purify, and thus the use of BSMD cuts during Υ reconstruction will not be implemented.

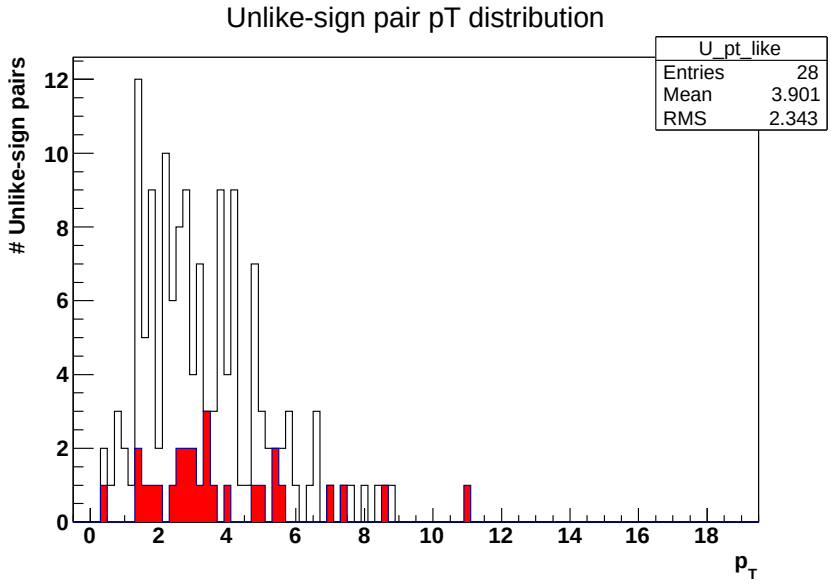

Figure 4.12: Transverse momentum (p_T [GeV/c]) of $\Upsilon \rightarrow e^+e^-$ candidates in Run-8 for unlike-sign (black) and like-sign (red) in STAR.

4.4.0.4 Identification: BPRS

The use of the Barrel Preshower (BPRS) for electron identification was previously discussed in Chapter 3. As it relates to this analysis, the electron identification has developed into a Υ reconstruction with a high S/B ratio. A calibrated BPRS detector is available in the Run-9 p+p 200 GeV data set, however, prior to this section it was concluded that any further application of electron identification acted more in the capacity of a liability to the statistical sample of reconstructed Υ's than it was as an asset to the S/B ratio in Υ reconstruction. Therefore, the S/B ratio in Run-8 (d+Au 200 GeV) and Run-9 data sets does not necessitate the use of the BPRS detector in Run-8 and Run-9, and it is not used for electron identification during the Υ reconstruction in this thesis.

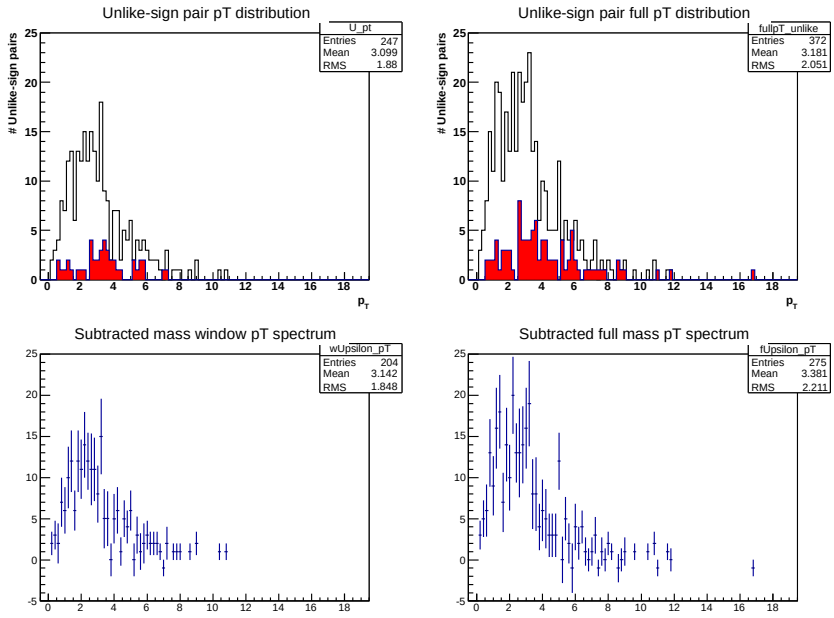

Figure 4.13: Transverse momentum (p_T [GeV/c]) of $\Upsilon \rightarrow e^+e^-$ candidates in Run-9 for unlike-sign (black) and like-sign (red) in STAR. The upper-left panel is candidate pairs in the 8-11.5 GeV/c mass-window. The lower-left panel is the p_T-distribution for 8-11.5 GeV/c, corrected for r.e.p. contributions using the combinatorial background subtraction method. The upper-right panel is candidate pairs for the full mass distribution. The lower-right panel is the p_T-distribution for the full mass spectrum, corrected for r.e.p. contributions, again, using the combinatorial background subtraction method.

4.4.0.5 Identification: TOF

A detector upgrade to help with charged particle identification in STAR, is the planned installation of a Time of Flight (TOF) system. The TOF system is still undergoing commissioning and on the verge of completion - currently TOF is available in Run-9 p+p $\sqrt{s}$ = 200 GeV data. However, because the reconstruction of Υ is sufficiently strong (high S/B), and because the correlation analysis does not require any identification into specific types of hadronic species, the TOF is not used.

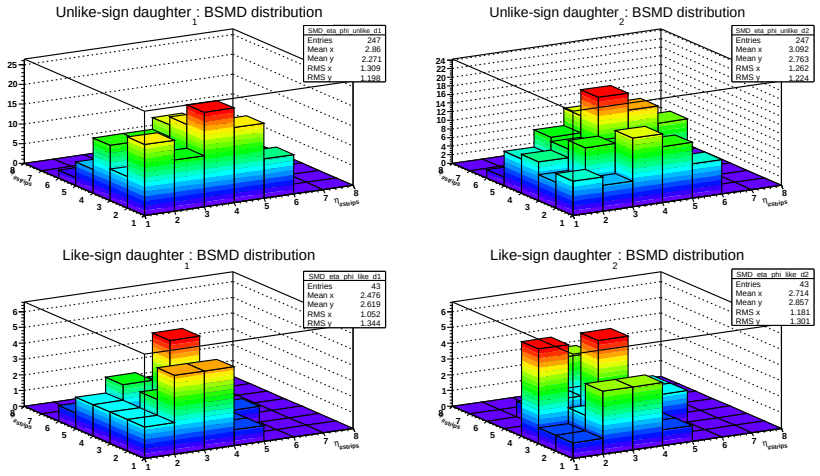

Figure 4.14: Number of strips in ϕ ($\phi_{\#strips}$) vs. number of strips in η ($\eta_{\#strips}$) hit in the BSMD for $\Upsilon \rightarrow e^+e^-$ daughter candidates.

4.5 Upsilon(nS) States and Embedding

An Υ(1S+2S+3S) mass-analysis separates a mass spectrum into the constituent Υ(1S), Υ(2S), and Υ(3S) states. The full Υ invariant mass spectra observed in Run-8 (Figure 4.9) and Run-9 (Figure 4.8) allows for the separation of the Υ signal into the Υ(1S+2S+3S) states. This thesis focuses on the decomposition of the Υ signal in the Run-9 data, via the use of embedded data[13]. Separating the Υ signal into the individual states requires use of the mass line-shape of each state from the embedded data, which includes the effects of detector resolution, radiation, and the underlying event.

4.5.1 Separation of Υ(nS) States and Line-shape

Recall the Υ signal in Run-9 p+p data using a like-sign combinatorial background subtraction resulted in the Figure 4.10. The Embedding group at STAR produced an

[13]Embedding introduces known Monte Carlo tracks, where the kinematics and particle type is known exactly, into a realistic environment seen in the analysis - a real data event.

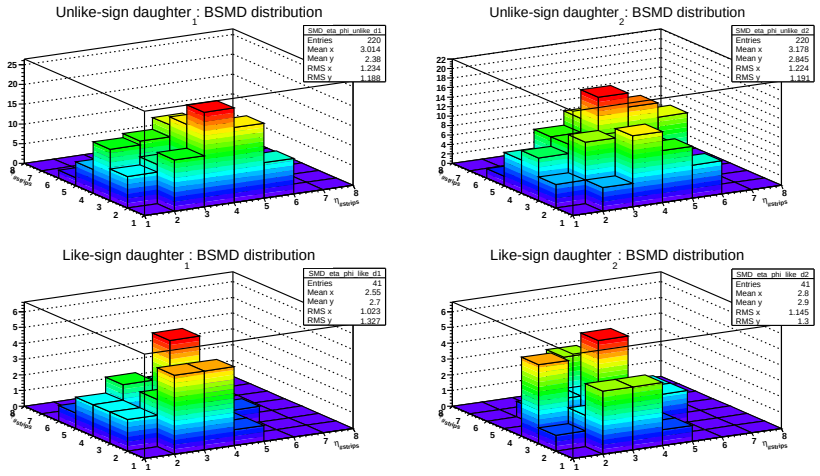

Figure 4.15: Number of strips in ϕ ($\phi_{\#strips}$) vs. number of strips in η ($\eta_{\#strips}$) hit in the BSMD with the condition that $\eta_{\#strips} > 1$ or $\phi_{\#strips} > 1$ for $\Upsilon \rightarrow e^+e^-$ daughter candidates.

Υ-embedded data set, composed of approximately 100K total Υ(1S+2S+3S) events embedded[14] into the Run-9 p+p data set. Resolving the Υ(nS) line-shape from embedding requires the reconstruction of the embedded Υ(nS) states, and then a fit to each of the states to extract their mean and sigma values.

All the same analysis cuts applied to the real data are also applied to the embedded data. Likewise, the trigger conditions imposed on the real data must be imposed on the embedded data. As such, the use of an ADC cut (adccut$_{trig}$) with a cluster energy cut (Ecut$_{trig}$) mimics the trigger-conditions on the daughter electrons in data. In particular, an ADC and cluster energy with a required 'seed energy' threshold cut is used to 'mimic' the behavior of the online Υ-trigger at STAR, by requiring a tower with a value of ADC > 18 be identified. If the ADC > 18 condition is met, then the particle is required to deposit enough energy to form a seed-tower, by depositing

[14]Embedded $\approx$ 33K each of Υ(1S), Υ(2S), Υ(3S).

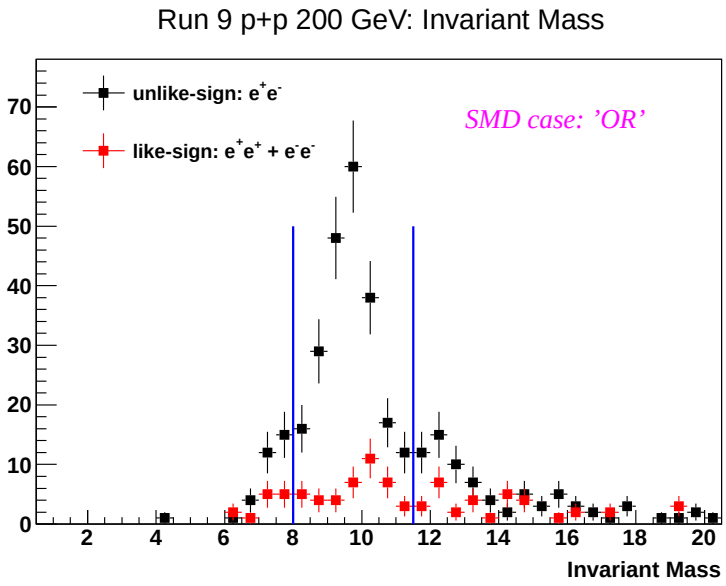

Figure 4.16: Invariant mass ($M_{inv.}$ $[GeV/c^2]$) distribution in Run-9 for unlike-sign (black) and like-sign (red) $\Upsilon \rightarrow e^+e^-$ candidate pairs in STAR, using the 'OR' BSMD-CONDITION. The blue vertical bars denote the region (8-11.5 GeV/c), where the S/B $\approx 5.37 \pm 0.91$.

an energy greater than 4.0 GeV. If the seed-tower of energy greater than 4.0 GeV is found, then the other daughter is also required to deposit a seed-energy greater than 1.2 GeV. If both seed-tower conditions are met, then a cluster of the seed tower plus the two adjacent surrounding towers with the highest energy is formed. If the sum of each cluster is greater than 4.5 GeV and 3.0 GeV, respectively, then the embedded event is accepted having satisfied the trigger conditions.

However, a simple fit using the line-shape from embedding only will not be sufficient to completely fit the results found in data. Accounting for the contributions from Drell-Yan background pairs (and $b\overline{b} \rightarrow e^+e^-$ continuum) in the invariant mass spectrum is also needed. To fit the Υ signal observed in data, use of a Drell-Yan parameterization valid at $|y| < 0.5$ (mid-rapidity) [25] in STAR is used.

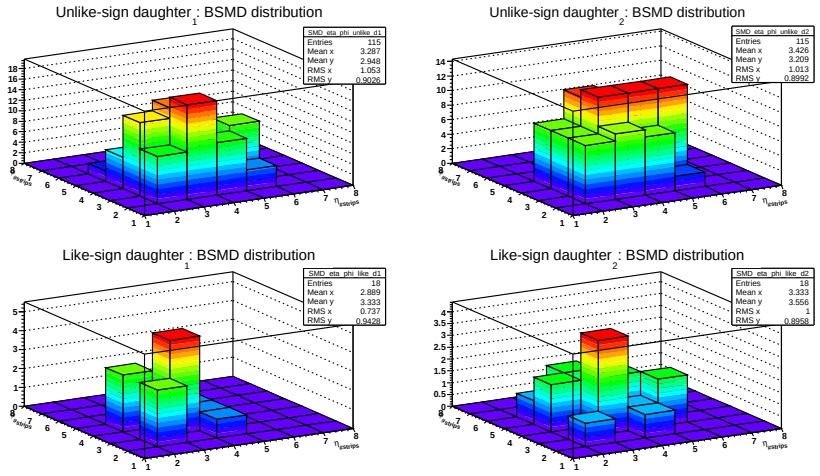

Figure 4.17: Number of strips in ϕ ($\phi_{\#strips}$) vs. number of strips in η ($\eta_{\#strips}$) hit in the BSMD with the condition that $\eta_{\#strips} > 1$ and $\phi_{\#strips} > 1$ for $\Upsilon \rightarrow e^+e^-$ daughter candidates.

4.5.1.1 Estimating the Drell-Yan Contribution

To estimate the Drell-Yan contribution the data is parameterized by the function [25]

$$DY = \frac{A}{(1+\frac{m}{m_0})^n} \times \frac{erf([\frac{m-8.07}{\sigma}]+1)}{2} \tag{4.1}$$

where $m_0 = 2.70$, $n = 4.59$, and $\sigma = 1.75$. With this equation and the three Υ line-shapes from embedding, two different fitting procedures to account for the contributions were used.

The 'floating-parameterization' method: the relative contributions from the 1S, 2S, and 3S states are allowed to float such that a best-fit is found. Figure 4.20 shows the line-shape fit to the combinatorial background subtracted Υ signal in Run-9 p+p data using this method.

The 'fixed-parameterization' method: the ratios known from previous measure-

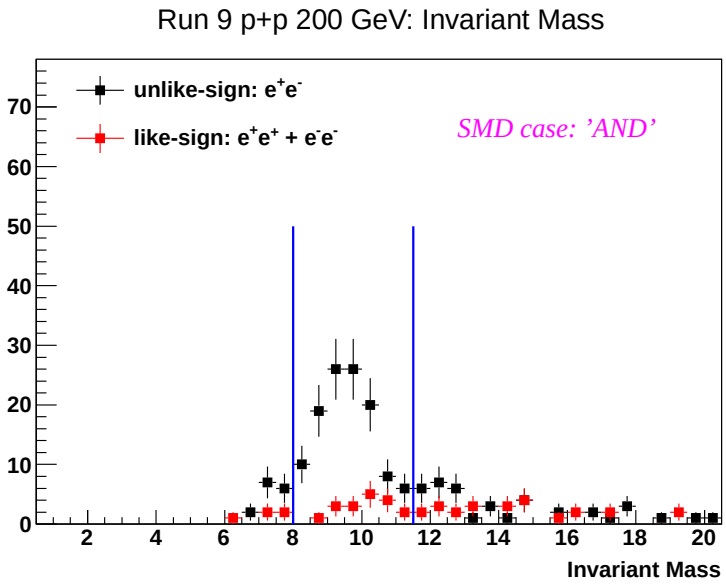

Figure 4.18: Invariant mass ($M_{inv.}$ $[GeV/c^2]$) distribution in Run-9 for unlike-sign (black) and like-sign (red) $\Upsilon \rightarrow e^+e^-$ candidate pairs in STAR, using the 'AND' BSMD-CONDITION. The blue vertical bars denote the region (8-11.5 GeV/c), where the S/B $\approx 6.39 \pm 1.62$.

ments and pQCD calculations are used.

$$\frac{\sigma(1S) \times B(1S)}{\sigma(2S) \times B(2S)} = \frac{6.6 \times 2.38}{2.18 \times 1.91} = 3.77 \tag{4.2}$$

$$\frac{\sigma(1S) \times B(1S)}{\sigma(3S) \times B(3S)} = \frac{6.6 \times 2.38}{2.18 \times 1.32} = 5.46 \tag{4.3}$$

These values are also tabulated in Table 4.4. Figure 4.21 shows the line-shape fit to the combinatorial background subtracted Υ signal in Run-9 p+p data, using this method.

Results from the two different fitting conditions and the contributing nS components are summarized in Table 4.5. The strength of the Drell-Yan is similar with

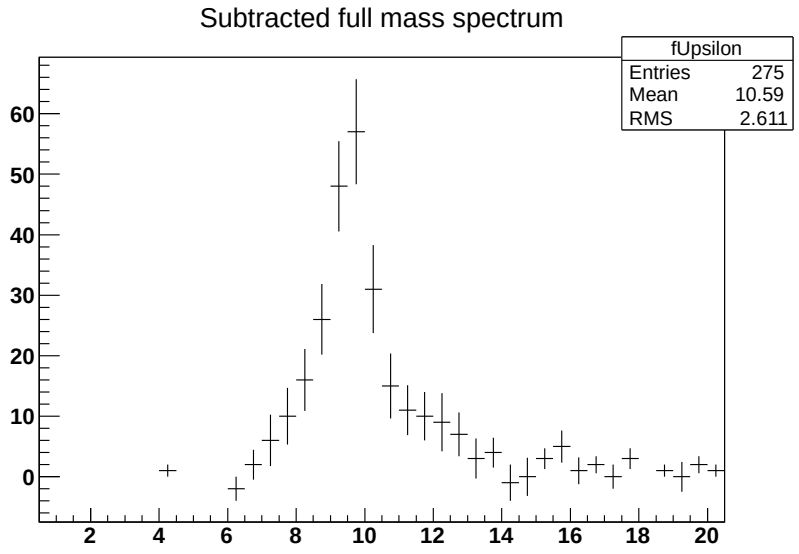

Figure 4.19: $M_{inv.}$ $[GeV/c^2]$ signal corrected for r.e.p. contributions using the combinatorial background subtraction method in Run-9 for $\Upsilon \rightarrow e^+e^-$ candidates in STAR.

both fits. For the 'fixed-parameterization' fit the Drell-Yan parameter is 4823 $\pm$ 1131.2; while for the 'floating-parameterization' fit the Drell-Yan parameter is 4795 $\pm$ 1166.9, with the Υ(1S)/Υ(2S) = 2.2 $\pm$ 1.5 and Υ(1S)/Υ(3S) = 26 $\pm$ 130. These ratios are in agreement with the values used in Eqn. (4.2) and Eqn. (4.3). Figure 4.21 suggests that some separation of states , at least the 1S from the 2S+3S states, may be possible by making mass cuts of m $<$ 9.5 GeV and m $<$ 10 GeV.

As shown, there is a non-negligible yield coming from the Drell-Yan background under the Υ invariant mass distribution. The Drell-Yan background is of particular importance here because its presence will directly affect the Υ spin-alignment ('polarization') measurement. The Drell-Yan contributions in the 'mass-window' are summarized in Table 4.6. The Drell-Yan polarization has previously been measured at E866 [24] and was found to be highly polarized. A discussion on 'background

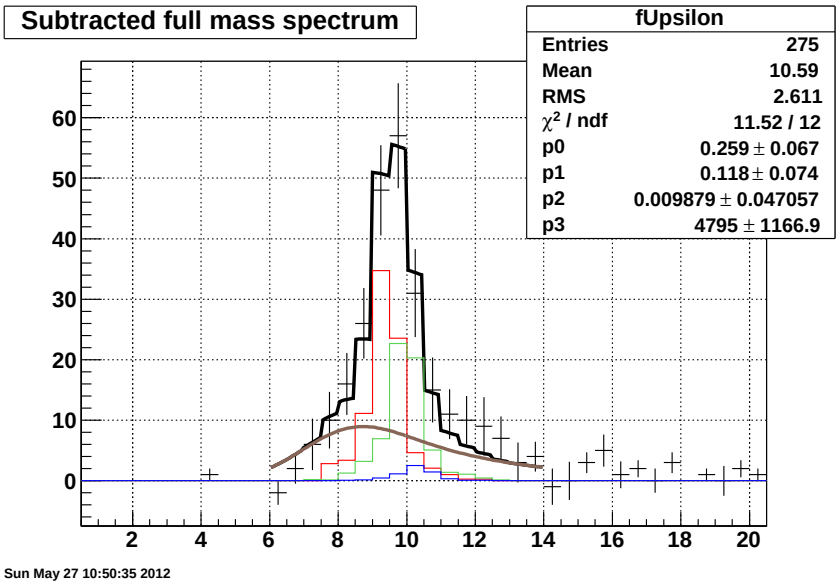

Figure 4.20: $M_{inv.}$ $[GeV/c^2]$ signal in Run-9 for $\Upsilon \rightarrow e^+e^-$ candidates in STAR, using the 'floating-parameterization.' The signal is fit with a line-shape using the reconstructed embedded Upsilon(1S) shown in red (color online), Upsilon(2S) shown in green (color online), Upsilon(3S) shown in blue (color online), and the Drell-Yan background shown in brown (color online). The total fit is shown as the solid, black line.

polarization' is found in Section 4.6.3.

4.6 Production-Related observable: Upsilon Spin-Alignment

The Υ spin-alignment ('polarization') measurement, measures the angular distribution of the positron in the sample of reconstructed Υ candidates. Recall that Figure 1.12 shows the scenario for a measurement of the two-body Υ decay (left panel), and theoretically expected $\cos(\theta)$ distributions with corresponding α values (right panel).

The form of the differential cross-section requires a calculation of $\cos(\theta)$, where the measured angle θ represents the geometrical angle between the direction of the

Table 4.4: Υ branching ratios from the Particle Data Group [16] and cross-sections from a NLO calculation.

Υ state	Branching ratio	Cross-section (nb)
Υ(1S)	2.38 $\pm$ 0.11	6.60
Υ(2S)	1.91 $\pm$ 0.16	2.18
Υ(3S)	2.18 $\pm$ 0.21	1.32

Table 4.5: Υ(nS) contribution ratios.

Υ(nS) relative fraction	$\mathbf{DY}_{floating-parameterization}$	$\mathbf{DY}_{fixed-parameterization}$
Υ(1S)/Υ(2S)	2.2 $\pm$ 1.5	4795 $\pm$ 1166.9
Υ(1S)/Υ(3S)	26 $\pm$ 130	4823 $\pm$ 1131.2

momentum of the e^+, measured in the Υ rest frame with respect to the Υ direction of motion - i.e. the 'polarization axis.' The form of the differential cross-section is given as:

$$\frac{d\sigma}{d(cos\theta)} \propto 1 + \alpha \cos^2\theta + (higher - orders - in - \alpha). \tag{4.4}$$

The resulting polarization will be determined by a best fit, where the parameter value α = -1, 0, +1 reflects longitudinal, zero, or transverse polarization, respectively.

In order to satisfy the Eqn. (4.4), the 'boosting' of the di-electron daughters used to reconstruct the Υ (Laboratory frame) to the Center of Mass (CM) frame is performed. The Lorentz boosting procedure was checked by noting that the conservation of momentum between daughter particles from a two-body decay in the CM frame

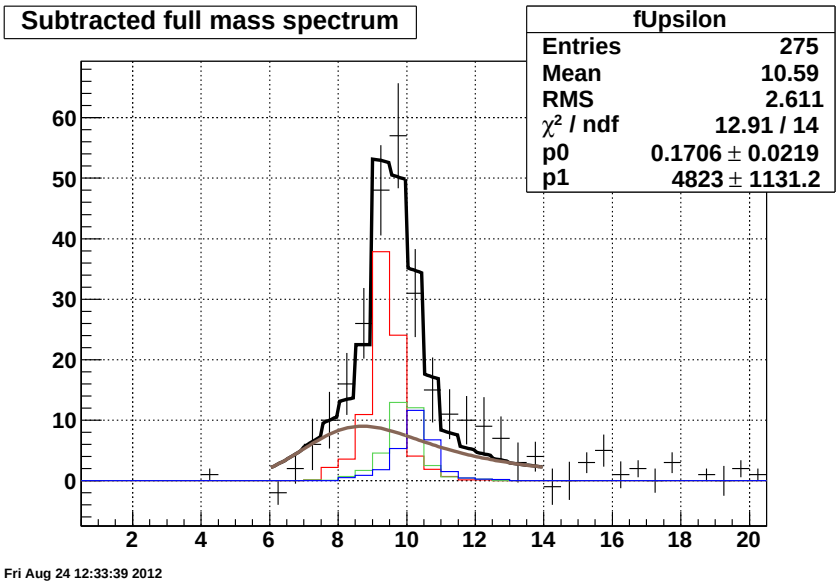

Figure 4.21: $M_{inv.}$ $[GeV/c^2]$ signal in Run-9 for $\Upsilon \rightarrow e^+e^-$ candidates in STAR, using the 'fixed-parameterization.' The signal is fit with a line-shape using the reconstructed embedded Upsilon(1S) shown in red (color online), Upsilon(2S) shown in green (color online), Upsilon(3S) shown in blue (color online), and the Drell-Yan background shown in brown (color online). The total fit is shown as the solid, black line.

should be zero. Figure 4.22 indicates that the sum of the momentum components (p_x, p_y, and p_z) for the daughter particles satisfies the back-to-back topology of a system that undergoes a two-body decay while at rest.

The raw[15] $\cos(\theta)$ distribution for reconstructed Υ candidates in Run-9 p+p data is then calculated[16]. Figure 4.23 shows the raw calculated $\cos(\theta)$ distribution in Run-9 p+p data. Figure 4.24 shows the raw calculated $\cos(\theta)$ distribution (top-panel) along with the corresponding rapidity ($|y| < 1.0$) values (bottom-panel), for the $\Upsilon \rightarrow e^+e^-$ candidates in Run-9 p+p data.

Measuring the Υ spin-alignment at 'mid-rapidity' ($|y| < 0.5$) confines the spin-

[15]The $\cos(\theta)$ distribution that has not been corrected for STAR acceptances.
[16]The mass-window constraint is assumed throughout the Spin-alignment analysis.

Table 4.6: The number of Υ and Drell-Yan per bin, within the 8-11.5 GeV/c^2 'mass-window.'

$\#_{DY}$	$\#_{counts_{mass-window}}$	$\#_{counts_{mass-window}}/\#_{DY}$
8 ± 2.8	16 ± 4.0	0.50 ± 0.22
9 ± 3.0	26 ± 5.1	0.35 ± 0.13
8 ± 2.8	48 ± 6.9	0.17 ± 0.06
7 ± 2.6	57 ± 7.5	0.12 ± 0.05
7 ± 2.6	31 ± 5.6	0.23 ± 0.09
6 ± 2.4	15 ± 3.9	0.40 ± 0.19
6 ± 2.4	11 ± 3.3	0.55 ± 0.27

alignment measurement to a region of the STAR detector where there is ideal (larger and more uniform acceptance) coverage, as opposed STAR coverage at higher rapidity[17]. However, a mid-rapidity does reduce the statistical sample by approximately 30%, and may not be absolutely necessary. Figure 4.25 shows the raw calculated $\cos(\theta)$ distribution after the $|y| < 0.5$ cut was applied (top-panel) along with the corresponding rapidity values of $|y| < 0.5$ (bottom-panel), for the Υ candidates in Run-9 p+p data. The next section discusses the Υ acceptance in STAR and calculation of the acceptance correction.

4.6.1 Upsilon and Acceptance

The raw calculated $\cos(\theta)$ distribution is dependent upon the STAR detector's acceptance and the spin-alignment analysis must be corrected for this. The acceptance correction requires the use of STAR Υ embedded data. The same Υ embedding sample that was used for the line-shape analysis is also the primary method[18] in determining the acceptance correction to be applied to the raw $\cos(\theta)$ distribution from

[17]Recall the discussion on rapidity (y) and pseudo-rapidity (η), from Chapter 2.

[18]Recall that PYTHIA was used to weight the p_T- and y-distributions, thrown flat in embedding.

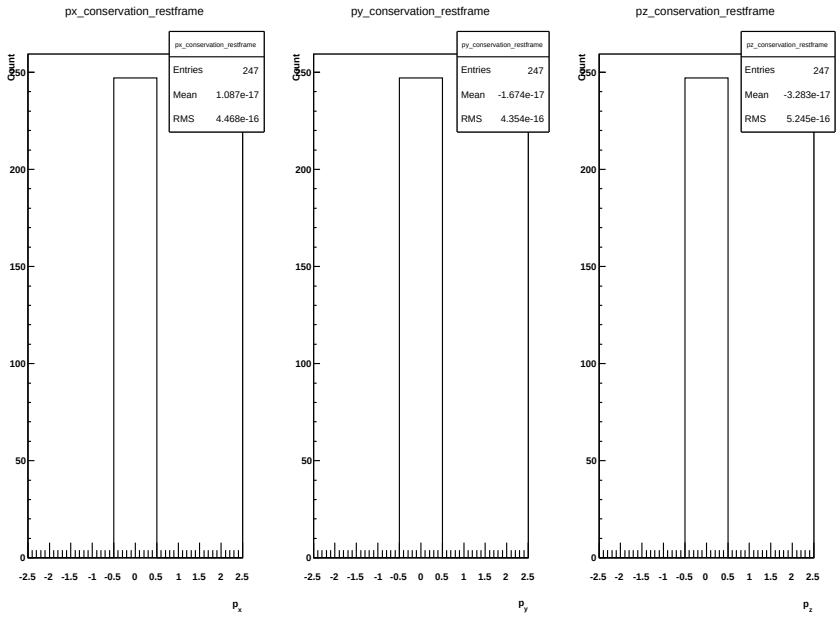

Figure 4.22: Momentum conservation of the two-body decay system ($\Upsilon \rightarrow e^+e^-$ candidates) in Run-9, in the STAR CM frame: Σp_x (left-panel), Σp_x (center-panel), Σp_z (right-panel).

data.

4.6.1.1 Upsilon and PYTHIA

Recall that the acceptance correction (determined from the embedding) is dependent on the PYTHIA simulation as an input for weighting the flat p_T- and y-distributions in embedding. As such, there may be a direct dependence on the input p_T and rapidity (y) spectra used to weight the flat distributions in the embedding. With respect to the choice of PYTHIA input there is a 'default' version of PYTHIA implemented during this analysis, but there is also a Heavy Flavor version of PYTHIA available at STAR, namely, the 'STAR-HF Tune[19]'. For different config-

[19]STAR proected access only: http://www.star.bnl.gov/protected/heavy/ullrich/pythia8/

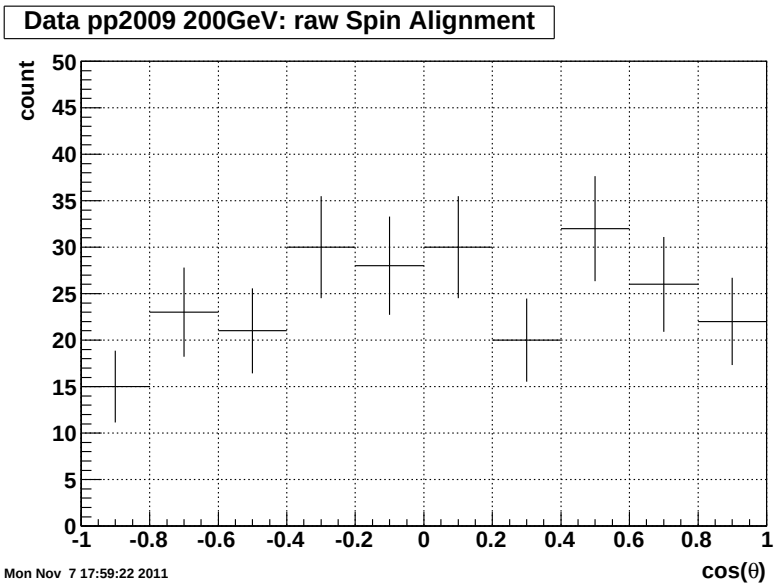

Figure 4.23: Raw cos(θ) distribution for Υ candidates in Run-9 p+p data.

urations of PYTHIA the prediction for the Υ p_T distribution can change. Figure 4.26 shows the Υ p_T distribution for each of the two different PYTHIA inputs. There is a clear difference between the p_T distributions in Figure 4.26. The STAR-HF Tune version (black-triangles) is much harder in p_T than the 'default' version. However, which version of PYTHIA is correct to use in this analysis will depend on how the shape of the efficiency corrected p_T distribution in data looks relative to the two different PYTHIA p_T distributions. Figure 4.27 shows the efficiency as a function of p_T for the 'default' (blue-bins) relative to the STAR-HF tune (red-triangles). There is no significant difference between each of the efficiency distributions in Figure 4.27. The efficiency using the STAR-HF Tune version (red-triangles) is more or less the same as that of the 'default' version. With the similarity in efficiency between the two PYTHIA configurations noted, the p_T distribution in data is efficiency corrected, then compared to the two different p_T distributions in PYTHIA. Figure 4.28 shows

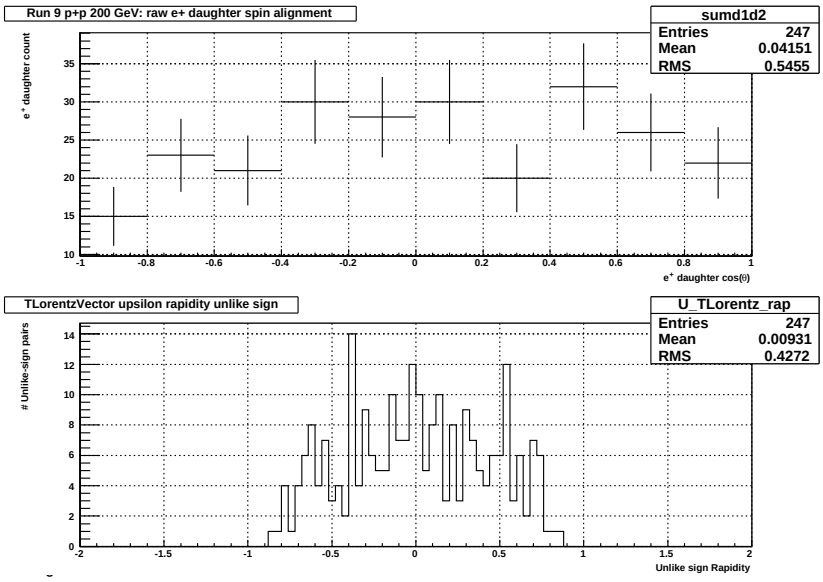

Figure 4.24: Raw cos(θ) distribution. (top-panel) and the $|y| < 1.0$ rapidity distribution (bottom-panel), for Υ candidates in Run-9 p+p data.

the efficiency corrected Υ p_T (unlike-sign candidates) in data, normalized to the scale of the number of Υ in PYTHIA. The Υ p_T for each of the PYTHIA configurations (default and STAR-HF Tune) are shown. It is clear that the data agree is more in agreement with the 'default' version and not the STAR-HF Tune, but at approximately $p_T > 3.5$ GeV/c, the data also undershoots the default PYTHIA prediction. Ultimately, the decision to choose the 'default' version of PYTHIA for calculating the acceptance correction and to not use the STAR-HF Tune was made, because the STAR-HF Tune p_T spectrum overall is much harder than what was seen in data.

4.6.2 Upsilon Acceptance-Correction

Using the polarization parameter (α) from Eqn. (4.4), a second-order polynomial fit ($1 + \alpha^2$) allows the polarization (α) to be extracted in the form of the coefficient from the polynomial fit. The 'raw' polarization may be determined by applying the

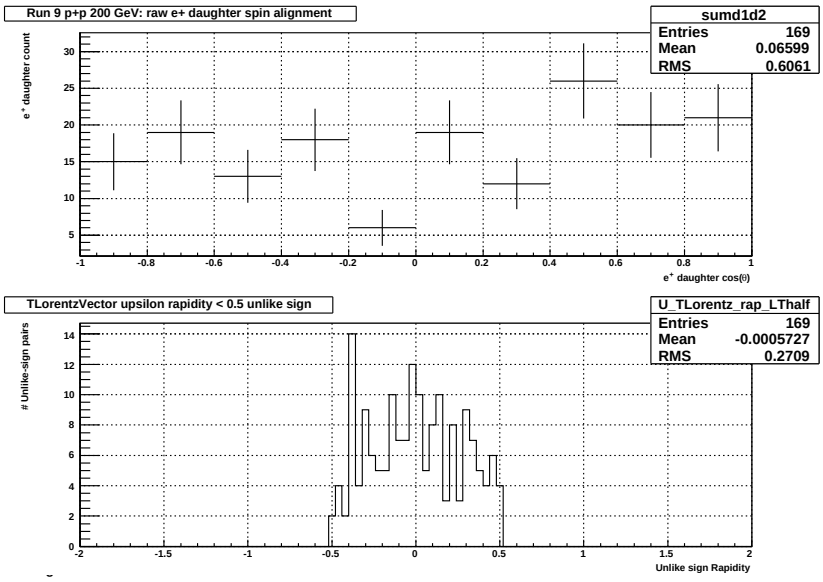

Figure 4.25: $\Upsilon \rightarrow e^+e^-$ raw cos(θ) distribution (top-panel) and the $|y| < 0.5$ rapidity distribution (bottom-panel), in STAR Run-9 p+p data

fit to Figure 4.23 ($|y| < 1.0$). Figure 4.29 shows the second-order fit to the raw cos(θ) distribution, giving a raw polarization value of α_{raw} = -0.3991 $\pm$ 0.1566.

Again, the embedded Υ must satisfy the same analysis cuts as the real data, as well as the trigger conditions. All if the trigger conditions, including ADC and energy cuts ('case11') are imposed on the embedded data. See Section(4.5. 4.5.1) for a description of these cuts. As a comparison, the trigger can be mimicked with momentum cuts ('case7') replacing the ADC and energy cuts. This is useful to understand the effects of the ADC and energy cuts alone. This can be seen in Figure 4.32. Since the difference in the correction for case7 vs. case11 is so large at the edges of cos(θ), it is useful to study the dependence of the correction on the input p_T distribution used for weighting.

In Figure 4.26, it can be seen that a harder Υ-p_T distribution will lead to a

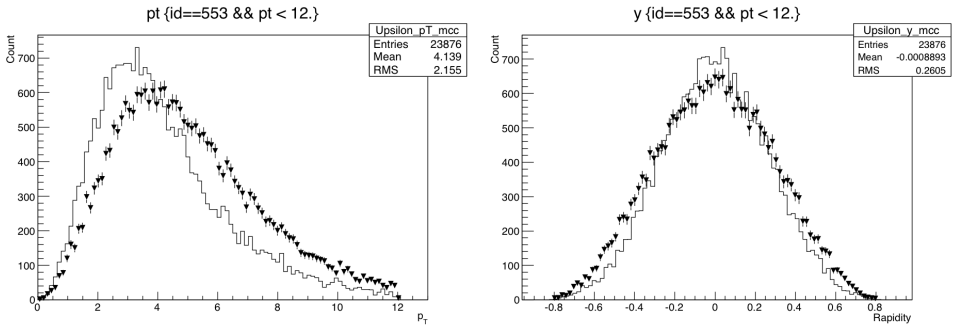

Figure 4.26: Υ p_T (left-panel) and y (right-panel) in PYTHIA: solid black-line is the 'default' version, while the STAR-HF Tune is the black-triangle.

higher probability that Υ's at higher p_T will lead to maximum 'boosts' for the decay daughters in the direction of the Υ (near the edges of $\cos(\theta)$) in the Lab frame, consequently throwing the one or both of the daughters out of the trigger-acceptance.

The proper way of imposing the STAR Υ-trigger conditions is to use the 'case11' configuration. In principle, the ADC and energy configuration outlined above is sufficiently close to the ADC and energy configuration used for the STAR online Υ-trigger, and is acceptable to use for calculating the acceptance correction. However, it was shown[20] that a comparison of the ADC distributions of the electrons from single electron, Υ, and J/ψ embeddings (Run-9 p+p) shows that the ADC from single electron embedding agrees with the J/ψ, but not the electrons from the Υ. The conclusion was that the ADC values in the Υ embedding was slightly off, perhaps the result of embedding calibration issues. Figure 4.30 shows the non-agreement between the ADC spectra of the electrons from Υ, J/ψ, and single electron embedding. To study the problem the U.C. Davis group fit each distribution to a 'crystal ball' [18], quantifying the discrepancy around the mean of the ADC to be about 11 ADC counts,

[20]U.C. Davis: Kurt Hill, STAR Analysis Meeting 4/16/2012.

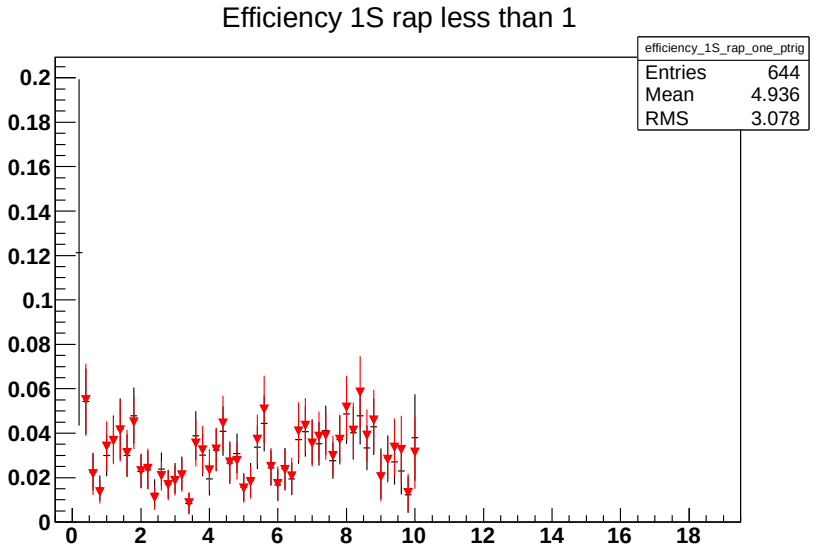

Figure 4.27: Υ efficiency as a function of p_T using embedding and PYTHIA: the 'default' version (black-bins), relative to the STAR-HF Tune (red-triangle).

and also quantified a discrepancy in the cluster energy between the single electron and electrons in Upsilon embedding to about 0.16 GeV. After the ADC values and cluster energies are each shifted/corrected, the Υ embedding agrees with single e^- and J/ψ embedding, resulting in a 'quick fix' to the Υ embedding. Figure 4.31 shows the Υ embedding vs. U.C. Davis simulation for the ADC spectrum (left-panel) and the cluster energy (right-panel). Applying the U.C. Davis prescribed fix to the ADC and cluster energy, the acceptance corrections are calculated.

The acceptance correction for case11 was applied to the raw cos(θ) distribution in data (Figure 4.23). Figure 4.33 shows the second-order fit to the acceptance corrected cos(θ) distribution in data with ($|y| < 1.0$) for 'case11.' The default fitting method used by ROOT is the χ^2-method, and each of the fitting results presented were based on the χ^2-method. In the case of low statistics such as the Υ polarization

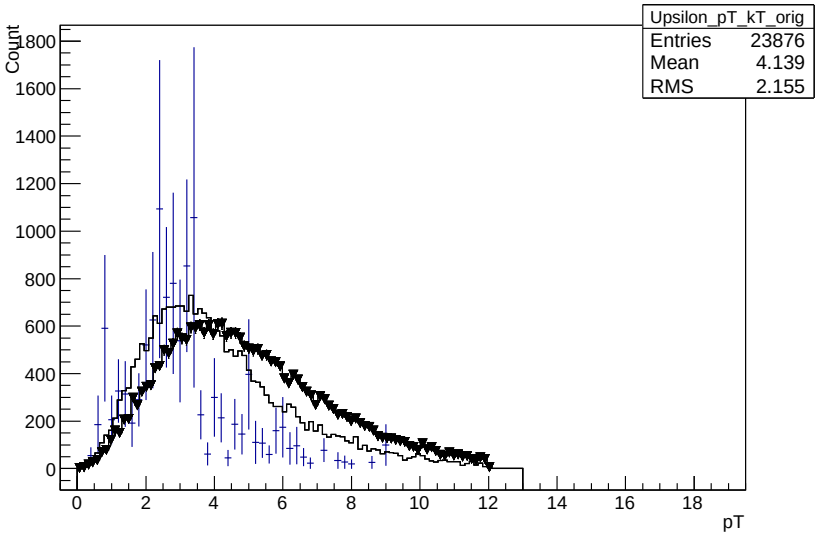

Figure 4.28: Υ efficiency corrected p_T distribution in data relative to PYTHIA: efficiency corrected data (blue-bins), normalized to the PYTHIA 'default' (solid black-line) and the STAR-HF Tune configurations (black-triangles).

measurement presented in this thesis, it is justified to use a log likelihood method. Figure 4.34 shows the log likelihood second-order fit to the acceptance corrected $\cos(\theta)$ distribution in data with ($|y| < 1.0$) for 'case11.'

The spin-alignment (polarization) measurement in STAR presented was performed over the full p_T-spectrum. The polarization measurement can be further separated into p_T-bins, where the Υ's polarization may be measured for each p_T-bin. Separating the Υ p_T-spectrum into four separate regions allows for each region to yield a fit value for Υ polarization that given p_T range. Figure 4.35 shows the Υ p_T-distribution at full- and mid-rapidity ($|y| < 0.5$). However, since the polarization measurement is over the rapidity range $|y| < 1.0$, the Υ p_T-distribution for all $|y| < 1.0$ were binned into four separate regions, catalogued in Table 4.7. Each p_T-region has its own unique acceptance-shape, and therefore the acceptance had to

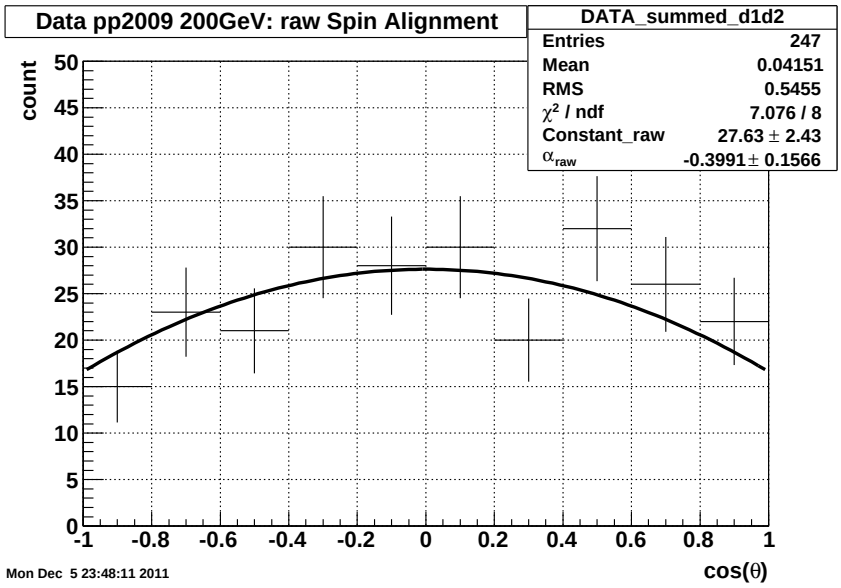

Figure 4.29: Raw $\cos(\theta)$ distribution corresponding to all rapidity ($|y| < 1.0$) values in Run-9 for $\Upsilon \to e^+e^-$ candidates, with a second-order polynomial fit. The resulting raw polarization value is α_{raw} = -0.3991 $\pm$ 0.1566.

be calculated for each of the four regions (for case11). Figure 4.36 shows the acceptance correction as a function of $\cos(\theta)$ at $|y| < 1.0$ values for 'case11.' Figure 4.37 shows the acceptance corrected $\cos(\theta)$ at $|y| < 1.0$ values for all four p_T regions for 'case11' fit with the χ^2-method. Figure 4.38 shows the acceptance corrected $\cos(\theta)$ at $|y| < 1.0$ values for all four p_T regions for 'case11' fit with the log likelihood method. Discussion of the measured polarization as it relates to the CSM and COM is discussed in the next chapter.

4.6.3 Background Polarization: Combinatoric, Hadronic, and Drell-Yan

Recall from Section 4.4 (Figure 4.8) that the calculated invariant mass distribution for unlike-sign and like-sign pairs in the region bound by the blue vertical bars contained very little background. However, these background sources need to be

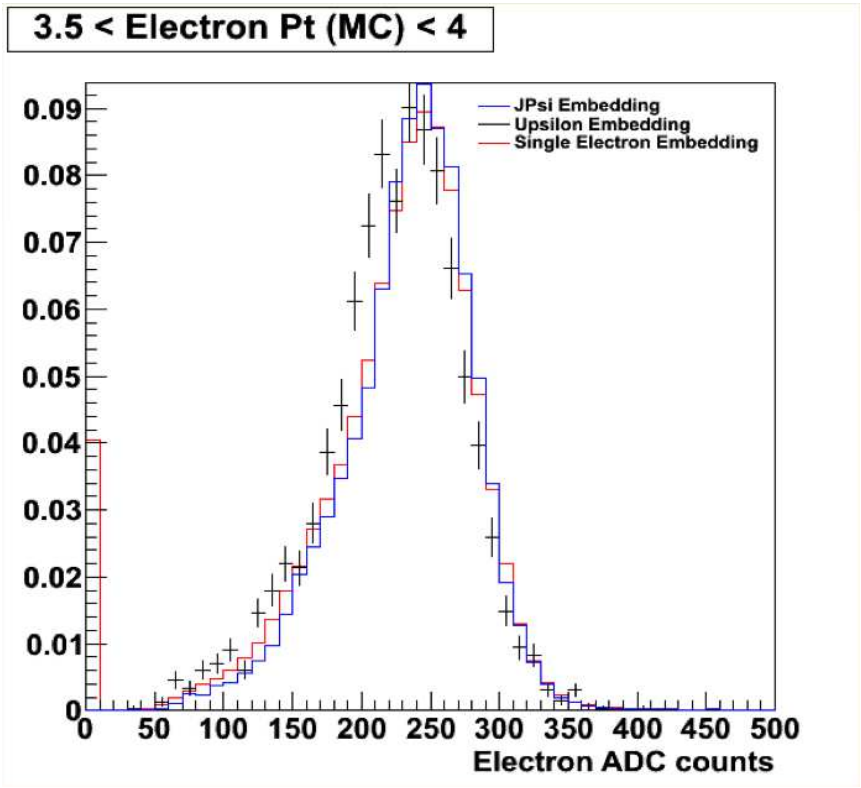

Figure 4.30: ADC distributions of the electrons from single electron, Υ, and J/ψ Run-9 p+p embeddings (U.C. Davis: Kurt Hill, STAR Analysis Meeting 4/16/2012.).

addressed as they may contribute to the overall polarization measured. There are three contributions to the Υ's background-polarization considered: 1) combinatorial 2) hadronic, and 3) Drell-Yan.

4.6.3.1 Combinatorial Background Polarization

To a good approximation the use of a non-subtracted combinatorial-background $\cos(\theta)$ distribution is justified if the $\cos(\theta)$ distribution of the combinatorial background is not polarized (i.e. flat). The combinatorial contribution to the measured polarization was determined by using the like-sign pairs $\cos(\theta)$ distribution. The $\cos(\theta)$ distribution is calculated for each of the like-sign pairs within each of the

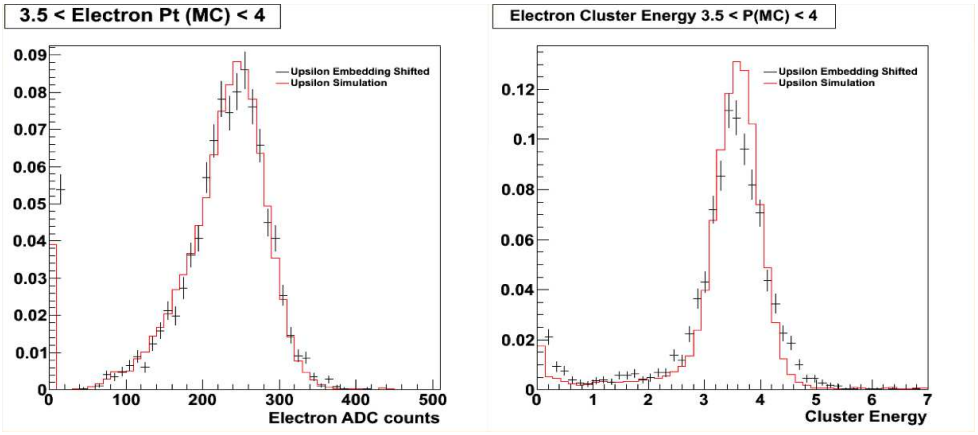

Figure 4.31: Corrected ADC (left-panel) and cluster energy (right-panel) distributions of the electrons from Υ Run-9 p+p (black-bin) embedding and Υ from (red-line) simulation (U.C. Davis: Kurt Hill, STAR Analysis Meeting 4/16/2012.).

Table 4.7: Υ p_T-region.

Abbreviation	**p_T-region**	**Unlike-sign count**	**Like-sign count**
ALL	$p_T > 0$ GeV/c	247	43
R1	$0 < p_T \leq 2$ GeV/c	74	9
R2	$2 < p_T \leq 4$ GeV/c	112	22
R3	$4 < p_T \leq 6$ GeV/c	42	10
R4	$p_T > 6$ GeV/c	19	2

rapidity limits mentioned above. Figure 4.39 shows the result of a first-order polynomial fit to the raw calculated like-sign pairs $\cos(\theta)$ distribution for all accepted ($|y| < 1.0$) rapidity values (left-panel) and the like-sign pairs within $|y| < 0.5$ (right-panel), in Run-9 p+p data. The fit to the like-sign $\cos(\theta)$ results in a χ^2/d.o.f. = 1.2 for $|y| < 1.0$, and χ^2/d.o.f. = 0.40 for $|y| < 0.5$. There is no significant polarization is observed in Figure 4.39 and as a consequence, the 'flat' $\cos(\theta)$ distribution for the

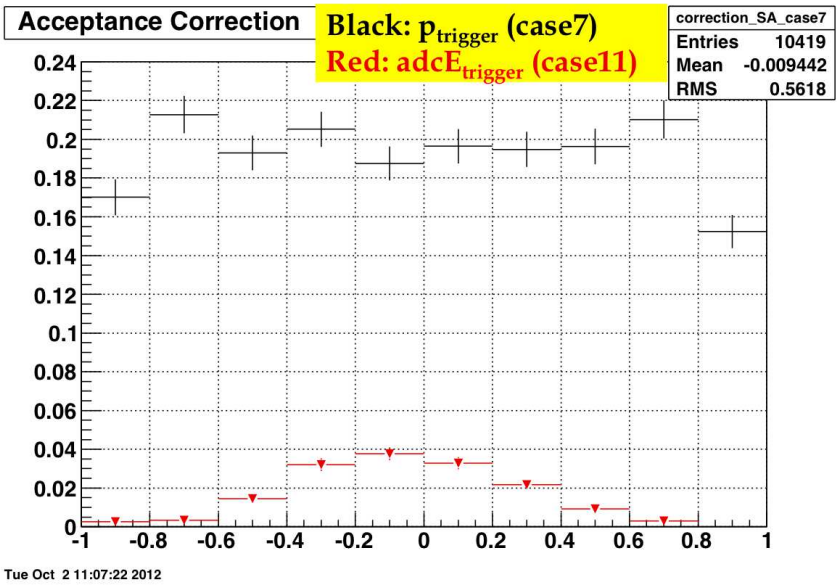

Figure 4.32: Υ embedded into real Run-9 p+p data: acceptance corrections as a function of $\cos(\theta)$ at $|y| < 1.0$, for case7 (black-bin), and case11 (red-triangle).

like-sign pairs will only scale the measured unlike-sign $\cos(\theta)$ distribution upward by a constant factor, which does not influence the curvature (shape) of the unlike-sign $\cos(\theta)$ distribution and hence, does not skew the resulting Υ polarization value measured.

4.6.3.2 Hadronic Background Polarization

Recall that the production related measurements were to be restricted to the 'narrow' mass-window (invariant mass region 8-11.5 GeV/c) in order to maximize the purity of the reconstructed Υ candidate sample. Decreasing the contribution of hadronic background polarization from the total measured polarization may be explored by strengthening hadron-rejection cuts, such as the use of a BSMD cut. From Section 4.4.0.3 there were two BSMD configurations studied - the 'OR' and

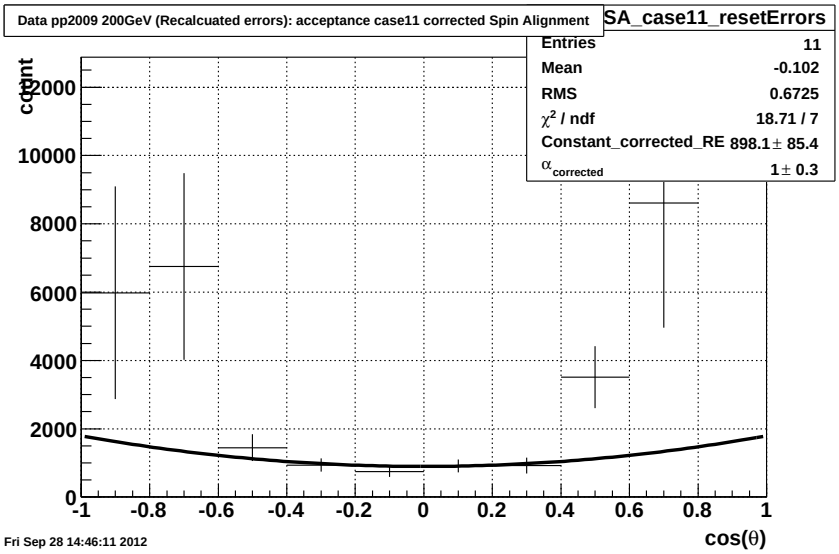

Figure 4.33: Acceptance corrected cos(θ) distribution (case11) in Run-9 data for $|y|$ < 1.0 values, with a second-order polynomial fit. The resulting polarization value is $\alpha^{case11}_{corrected} = 1 \pm 0.3$.

'AND' cases, which were compared to the baseline 'NULL' case[21]. Recall that the 'NULL' case was measured to have a S/B = 247/43 $\approx 5.74 \pm 0.95$, in Run-9 p+p data. Figure 4.8 shows the calculated invariant mass distribution for unlike-sign and like-sign pairs in Run-9 p+p data. Figure 4.16 showed the calculated invariant mass distribution (in the region 8-11.5 GeV/c) for unlike-sign and like-sign pairs in Run-9 p+p data, for the 'OR' case, where a S/B = 220/41 $\approx 5.37 \pm 0.91$ was measured. Figure 4.18 showed the calculated invariant mass distribution (in the region 8-11.5 GeV/c) for unlike-sign and like-sign pairs in Run-9 p+p data, for the 'AND' case, where a S/B = 115/18 $\approx 6.39 \pm 1.62$ was measured.

Measuring the Υ polarization using the 'NULL' (baseline) case is the representative of all Υ candidates within the 'mass-window' having $|y| < 1.0$. The baseline S/B

[21]No BSMD cut used.

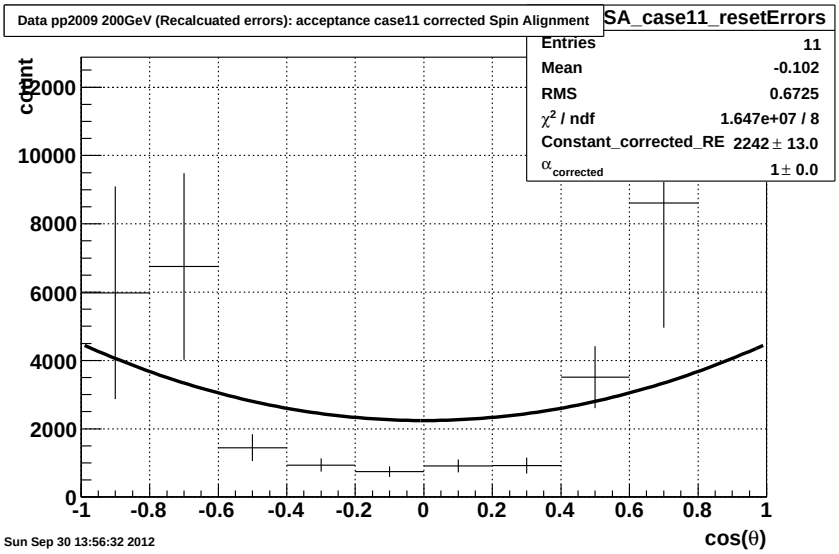

Figure 4.34: Acceptance corrected cos(θ) distribution (case11) in Run-9 data for $|y|$ < 1.0 values, with a second-order polynomial fit, using the log likelihood method. The resulting polarization value is ${}^{|y|<1.0}\alpha^{case11}_{corrected} = 1 \pm 0$.

= 247/43 $\approx$ 5.74 $\pm$ 0.95 is reasonably high, and the use of BSMD cuts ('OR' and 'AND') do marginally change the S/B signals. In the case of the 'OR' cut the S/B decreases, and in the case of the 'AND' it increases, but within the uncertainties they are all consistent with each other. This indicates that there is no significant hadronic background rejected by such an additional cut. Since the cut is, in principle, very effective at rejecting hadronic background (as discussed in Section 4.4.0.3), one can conclude that there is no significant hadronic background in the Υ candidates.

4.6.3.3 Drell-Yan Background Polarization

Experiment E866 determined that the Drell-Yan process is highly polarized [24]. WIth respect to the analysis in this thesis, the $\alpha_{DY} = 1.0 \pm 0.05$ for 1.8 GeV/c $\leq$ p_T $\leq$ 4.0 GeV/c result can be taken from experiment E866 [24] as a back-of-the-envelope indication of what the Drell-Yan polarization effect is on the Υ polarization. The Υ

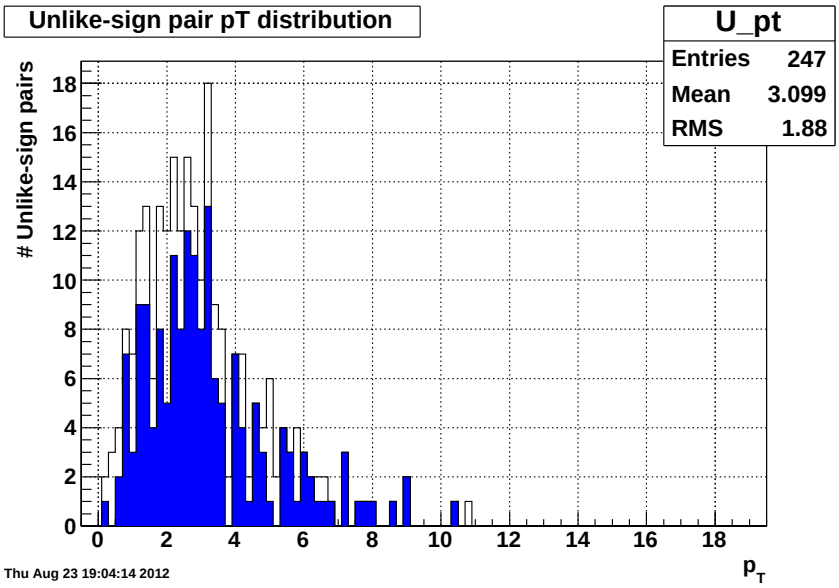

Figure 4.35: Υ transverse momenta in Run-9 data for full-rapidity (black-line) and mid-rapidity $|y| < 0.5$ (blue-fill).

polarization was partially due to a contribution of 25% ± 4% Drell-Yan background polarization signal. Using the measured result as $\alpha^{case11}_{corrected} = 1 \pm 0.3$ and subtracting out the properly normalized Drell-Yan contribution of $\alpha_{DY} = 1.0 \pm 0.05$ results in an $\alpha_{DY subtracted} = 1 \pm 0.3$.

4.7 Production-Related Observable: Upsilon + h correlations

The Υ + h correlation measures the hadronic activity directly around the reconstructed Υ. The relation of the hadronic activity to the origin of the gluon radiation emitted off the $b\bar{b}$ during production is sought. The azimuthal correlations between the Υ and charged hadrons is calculated and compared to simulations. The simulations framework rests on the PYTHIA event generator[22]. The goal of the analysis is

[22]Future work may be supplemented by an additional event generator, called 'MADonia [51].'

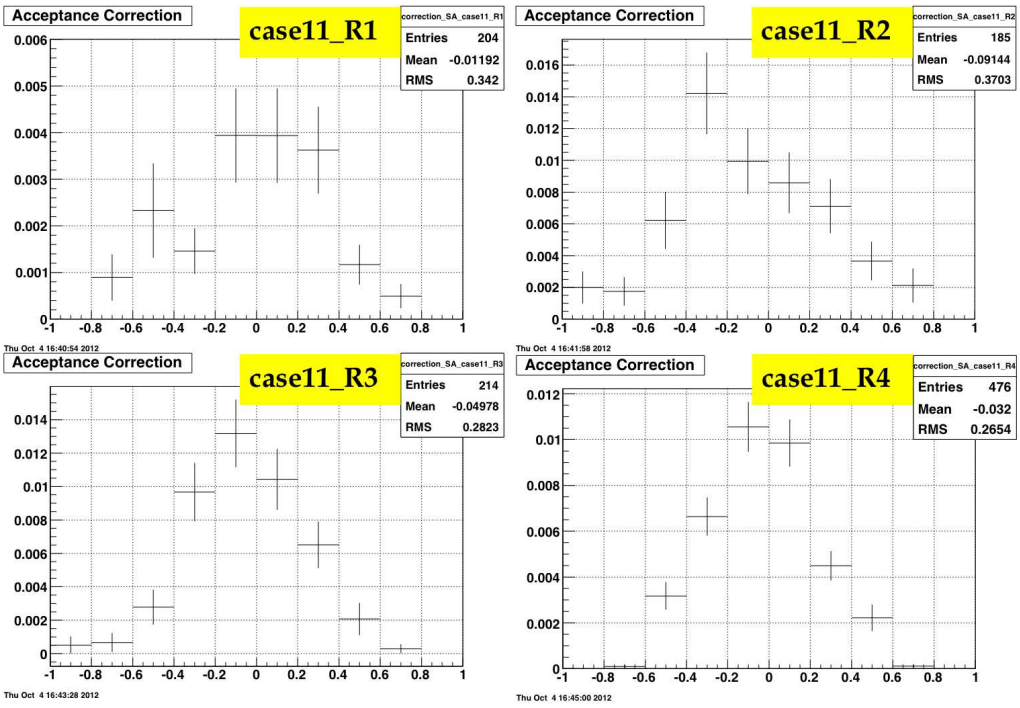

Figure 4.36: Acceptance corrections as a function of cos(θ) in Run-9 at $|y| < 1.0$, for case11. Region 1 (upper-left panel), Region 2 (upper-right panel), Region 3 (lower-left panel), and Region 4 (lower-right panel).

to decompose the observed correlation shape into the respective contributions coming from the gluon activity associated with CSM and COM production.

4.7.1 The Azimuthal Correlation Function: $\Delta\Phi$

Construction of the azimuthal correlation function by placing a further restriction on the selection of Υ candidates. Only the Υ candidates which reconstruct to within an invariant mass-window between 8.0-10.5 GeV/c^2 (Run-8 d+Au data) and 8.0-11.5 GeV/c^2 (Run-9 p+p data) are used for the azimuthal correlation analysis. The mass-window was constrained to increase (purify) the S/B ratio of the reconstructed Υ-candidate sample. Restricting the Υ candidates to be within this mass-window

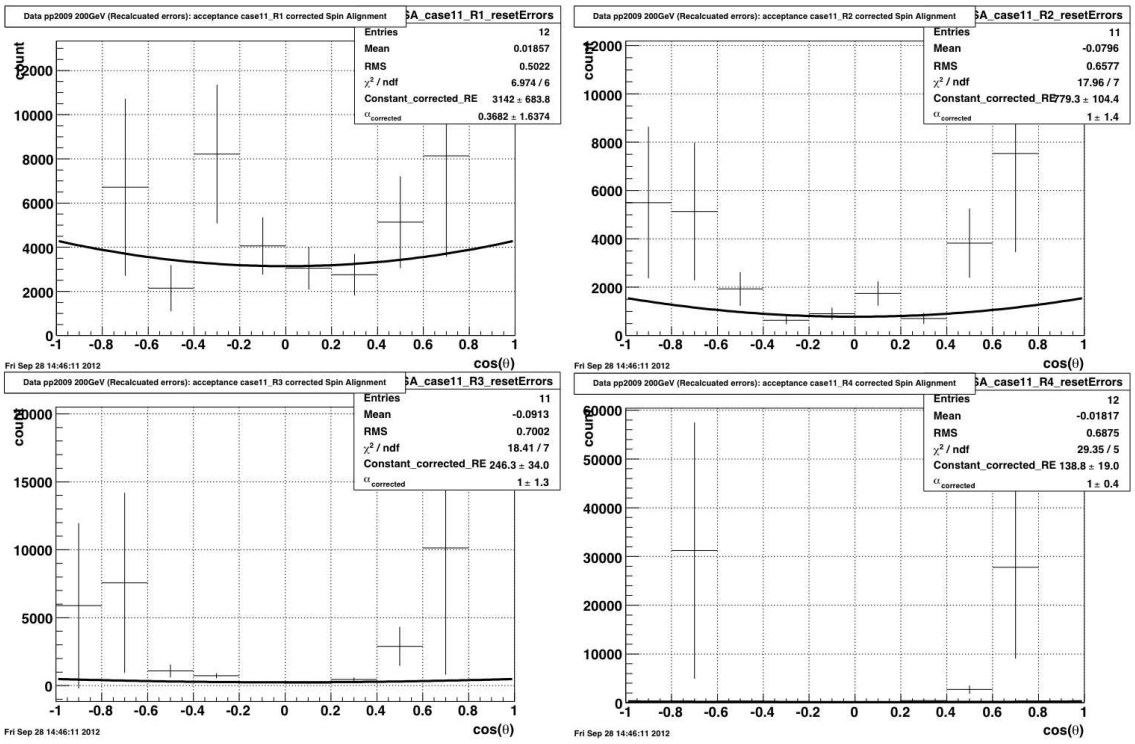

Figure 4.37: Acceptance corrected $\cos(\theta)$ distribution (case11) in Run-9 data for $|y| < 1.0$. Region 1 (upper-left panel) $\alpha^{case11}_{corrected} = 0.3682 \pm 1.6374$, Region 2 (upper-right panel) $\alpha^{case11}_{corrected} = 1 \pm 1.4$, Region 3 (lower-left panel) $\alpha^{case11}_{corrected} = 1 \pm 1.3$, and Region 4 (lower-right panel) $\alpha^{case11}_{corrected} = 1 \pm 0.4$.

does further reduce an already statistically low sample of reconstructed Υ's, but the competition between purity and statistics favors keeping the mass-window condition in place[23] during the azimuthal correlation measurement. The distribution of correlated particles is normalized by the number of triggered particles (i.e. charged hadrons per Υ trigger); because this is not intended to be a cross-section analysis, the absolute Υ yield is not relevant within the current analysis. The cuts imposed on the Υ during the azimuthal correlation are shown in Table 4.8.

The tracks that belong to an event in which an Υ candidate has been recon-

[23]The mass-window constraint is assumed throughout the $\Delta\Phi$-correlation.

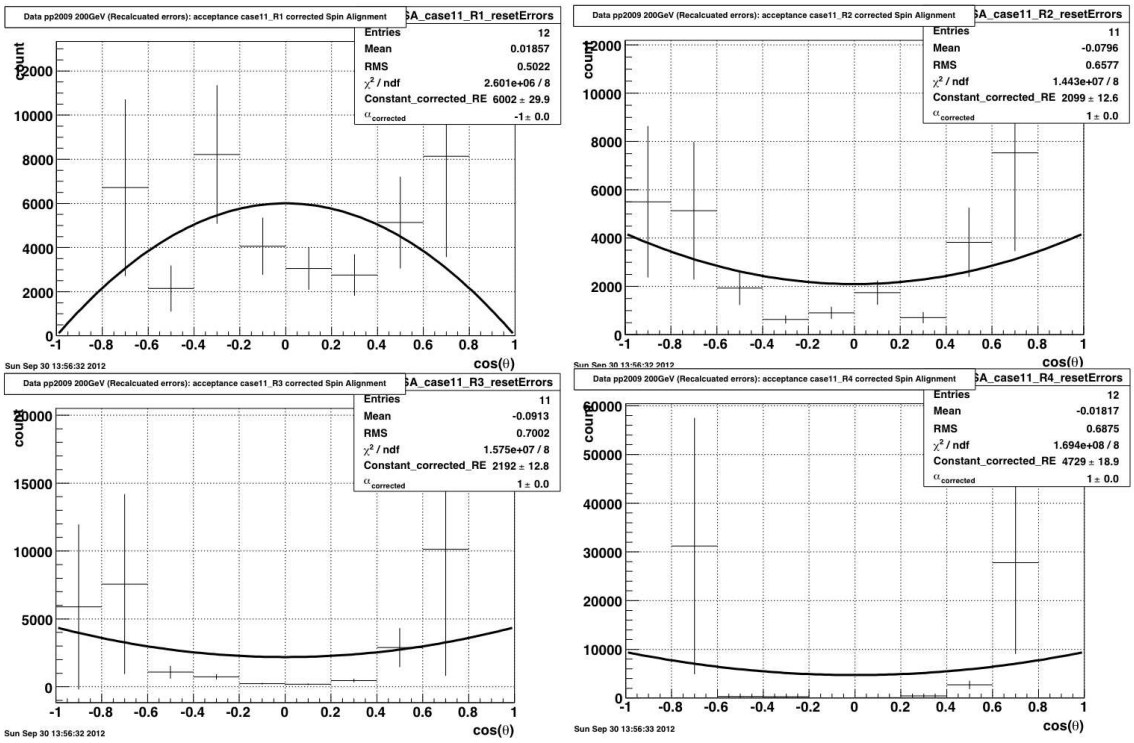

Figure 4.38: Acceptance corrected cos(θ) distribution (case11) in Run-9 data for $|y| < 1.0$. Region 1 (upper-left panel) $\alpha^{case11}_{corrected}$ = -1 $\pm$ 0, Region 2 (upper-right panel) $\alpha^{case11}_{corrected} = 1 \pm 0$, Region 3 (lower-left panel) $\alpha^{case11}_{corrected} = 1 \pm 0$, and Region 4 (lower-right panel) $\alpha^{case11}_{corrected} = 1 \pm 0$

structed are called associated tracks. The associated tracks are the charged particles that both traverse and are detected by the TPC[24]. No particle identification on the charged tracks (presumed to be predominately hadrons) is made, but selection cuts that further constrain the pool of associated charged tracks are used. To avoid making an auto-correlation of the daughter e^+e^- tracks coming from the Υ candidates to the associated charged hadron sample, comparison of the track identification number (track ID), unique for each track belonging to that event, is checked and then rejected if the associated tracks track ID matches with either of the Υ daughter track

[24]Hadronic tracks are also required to be satisfy TPC track flag = 301.

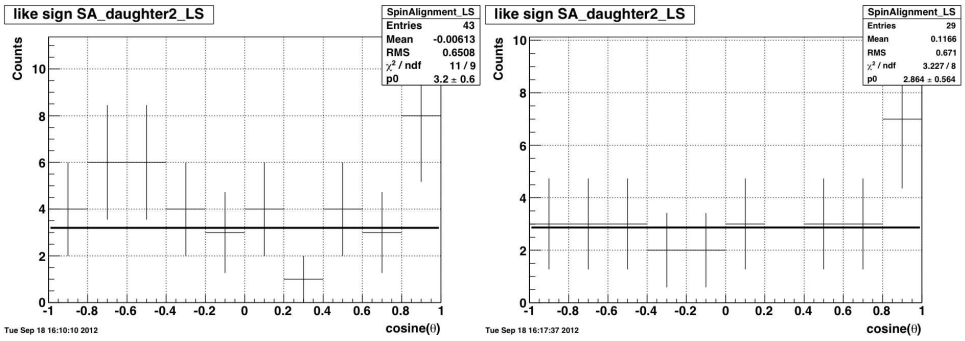

Figure 4.39: Like-sign raw $\cos(\theta)$ distribution for all accepted y values (left-panel) and the like-sign pairs within $|y| < 0.5$ (right-panel), in STAR Run-9 p+p data

Table 4.8: Υ $\Delta\Phi$ - correlation analysis cuts.

Collision-system	**Cut Parameter**	**Cut value**
p+p	$Mass_{inv.}$ (e^+e^-)	[8.0,11.5] GeV/c^2
d+Au	$Mass_{inv.}$ (e^+e^-)	[8.0,10.5] GeV/c^2

IDs.

The 'baseline' cut configuration on track selection was the initial (and typically standard) application of track quality cuts used in STAR analyses. The specific type of analysis determines the final constraints, or the combination of cuts imposed on the tracks. The investigation into the Υ + hadron correlation analysis[25] follows the track selection shown in Table 4.9.

The unidentified charged hadrons (explicit hadron identification is not required) which pass the associated particles selection cuts are then available for use to construct the correlation function. The reconstructed invariant mass of the Υ candidates

[25]Also denoted as Υ + h

Table 4.9: Baseline configuration: associated hadron (primary) track cuts.

Cut Parameter	**Cut value**
$TPC_{trackflag}$	301
# fit points	> 20
# fit points / # fit points$_{possible}$	> 0.52
abs(η)	< 1.0
DCA$_{global}$	< 3.0
p_T	> 0.5 GeV/c

and its association to each of the charged hadronic tracks coming from the same Υ event are then used to calculate the azimuthal correlation function, $\Delta\Phi$. The Φ angle assigned to individual tracks in the measurement is the track's azimuthal angle, originating from the primary vertex. The $\Delta\Phi$ is measured by calculating the difference in the Φ angle of the Υ with the Φ angle for each of the charged hadron candidates in the same event.

$$\Delta\Phi \equiv \Delta\Phi_h - \Delta\Phi_\Upsilon. \tag{4.5}$$

The result of the calculated $\Delta\Phi$ for each charged track is then mapped onto a domain of $\Delta\Phi_{full}$ = [-1.58,4.72] plotted against the number of charged hadrons per Υ trigger. I.e. $\Delta\Phi$ vs. $\frac{1}{N^{\Upsilon}_{trigger}}\frac{dN_{charged}}{d(\Delta\Phi)}$. This completes the definition of the azimuthal correlation. Recall that Figure 1.13 gives the rough depiction of the physical picture, which may defined quantitatively. The 'full correlation' is defined as

$$-1.58 \leq \Delta\Phi_{full} \leq 4.72. \tag{4.6}$$

The 'near-side' and the 'away-side' are particular regions of interest with the mea-

surement, and these domains are separated into the near-side

$$\Delta\Phi_{near-side} \equiv |\Delta\Phi| < 1.6, \tag{4.7}$$

and the away-side

$$\Delta\Phi_{away-side} \equiv |\Delta\Phi - 3.141| < 1.6. \tag{4.8}$$

4.8 Foreground and Background

It is clear from data that the reconstructed Υ invariant mass peaks in both the d+Au and p+p collisions have a high S/B ratio. However, there does remain a background presence in the unlike-sign e^+e^- pairs coming from random e^+e^- pairings not associated with a true Υ decay. The like-sign technique will reproduce the random e^+e^- pairings component of the combinatorial background (N = N_{+-} - $2\sqrt{N_{++}N_{--}}$) in the invariant mass distribution, but another step must be considered in order to properly correct for the presence of background in the total Υ + hadron correlation. The correlations between misidentified Υ's and charged hadrons should be different than those from real Υ and charged hadron events.

To obtain the true foreground component of the Υ + hadron correlation function the azimuthal correlation between like-sign e^+e^+ + e^-e^- pairs and charged hadrons must also be measured. I.e. the azimuthal correlation is represented by the total sum of two components: (Υ + hadron)$_{TotalCorrelation}$ = (Υ + hadron)$_{ForegroundCorrelation}$ + (Υ + hadron)$_{BackgroundCorrelation}$. This requires a correction to the total Υ + hadron correlation function using a subtraction correction of the background contributions that are arise from like-sign pairs and charged hadrons. A detailed derivation of the resulting background correction and the resulting true foreground component of Υ + hadron is provided in Appendix A.

4.9 Pile-up Tracks In the Correlation Function

It is well understood that to properly determine useful physical quantities in the collision of any system, an accurate location of the primary vertex is required. The precise reconstruction of a primary vertex is necessitated by the direct correspondence of the collision(s) that fire(s) any given trigger(s) to what was a physically measurable event (e.g. an Υ triggered event). At RHIC, the bunch crossing-rates and high luminosities coupled with the electronic limitations of differing sub-detector read-out times in STAR (e.g. $t_{TPCreadout} < t_{BEMCreadout}$). This limitation in readout time results in tracks from multiple collisions being recorded and read out by the TPC, for each of the triggered events. The presence of this effect is called 'pile-up', and it is inevitably recorded and processed in the data stream for each triggered STAR event. Detailed studies have shown that the average number of pile-up vertices is proportional to the instantaneous luminosity [57]. In order to properly analyze the results and to determine the integrated luminosities in data for particular trigger configurations in STAR, the known presence of pile-up must be addressed. There are three types of pile-up to be concerned with; vertices that come from collisions within the same bunch crossing, vertices that come from collisions in the earlier (pre-) or later (post-) bunch crossings. The subject of primary vertices (and primary tracks) is an in-depth one; it is not intended to explore the methods used to mitigate the pile-up issue in any considerable amount of detail, but rather to make plausible the expected presence of pile-up tracks in data, and to advance to the discussion into how pile-up is addressed and removed from the present analysis.

Recall from Section 4.7.1, that tracks originating from an event that have been reconstructed with an Υ candidate are called associated tracks. The associated tracks are the charged particles (predominantly hadrons), with no additional particle identi-

fication implemented. The hadronic tracks pointing back to the primary vertex location (within the allowed for DCA) of the reconstructed Υ may in fact not truly belong to the reconstructed Υ event. I.e. the tracks may be hadronic, but for the reasons inferred to in the preceding paragraph, they been falsely associated as belonging to the primary vertex location of the reconstructed Υ but actually belong to another vertex (pile-up vertex). The falsely associated tracks are called pile-up tracks, and these pile-up tracks belong to the nearby-vertices (vertices that are nearby the reconstructed Υ), or it is possible the track itself has been poorly reconstructed. Quantitatively, the associated tracks may be partitioned: $\text{associated}_{tracks} = \text{associated}_{trueprimarytracks} + \text{associated}_{pile-uptracks}$. The issue will be to exploit the available STAR tools and methods for systematically removing the $\text{associated}_{pile-uptracks}$ component, while not removing the true associated tracks within the correlation function - i.e. optimizing the cuts for pile-up removal.

4.10 Pile-up Track Rejection Methods

The sizable presence of pile-up vertices means that there is a need to remove the pile-up tracks. There are a few options that can be considered to do this, and the exact combinations of the cuts to implement is considered. The use of embedding is also need to determine which cut is the most effective at pile-up rejection. In embedding any loss due to a cut is an inefficiency only. In data, the loss due to a cut is the same is the same inefficiency plus background rejection. The following subsections detail the impact of these rejection methods on the associated track population, and which rejection method (or methods) optimizes the associated track sample. The pile-up rejection cuts are tabulated in Table 4.9, as well as the tables found within this section.

The 'baseline' was previously defined in Table 4.9, and the various ratios of these

Table 4.10: Associated charged hadron pile-up removal cuts.

Bundle#	**Bundle# definition**
bundle1	baseline
bundle2	baseline + ($\mathrm{DCA}_{global} < 1$)
bundle3	baseline + DCA_D
bundle4	baseline + DCA_D + ($\chi^2 < 6$)
bundle5	baseline + ($\mathrm{DCA}_{global} < 1$) + ($\chi^2 < 6$)
bundle6	baseline + ($\mathrm{DCA}_{global} < 1$) + DCA_D + ($\chi^2 < 6$)

bundles using the embedded charged pion (π^+) data was used to determine which combination of the pile-up rejection cuts optimized the rejection of track pile-up. The definition of the ratios of different bundles is shown in Table 4.11.

Table 4.11: Defining the ratios of various bundles.

Ratio	**Ratio definition**
α	$\frac{bundle2}{bundle1}$
β	$\frac{bundle3}{bundle1}$
γ	$\frac{bundle4}{bundle1}$
δ	$\frac{bundle5}{bundle1}$
ξ	$\frac{bundle4}{bundle3}$
η	$\frac{bundle5}{bundle2}$
ρ	$\frac{bundle6}{bundle1}$

The 'rejected fraction' is indicative of the fractional loses of the hadronic candidate tracks in data relative to the known π^+ tracks during the embedding reconstruction.

Table 4.12: Ratios and the rejected fraction of known π^+ tracks.

Ratio	**Data rejected fraction**	**Embedding rejected fraction**
α	$88 \pm 5\%$	$96 \pm 5\%$
β	$98 \pm 5\%$	$96 \pm 5\%$
γ	$74 \pm 5\%$	$83 \pm 5\%$
δ	$74 \pm 5\%$	$83 \pm 5\%$
ξ	$77 \pm 5\%$	$87 \pm 5\%$
η	$86 \pm 5\%$	$87 \pm 5\%$
ρ	$74 \pm 5\%$	$83 \pm 5\%$

4.10.1 Distance of Closest Approach (DCA)

The distance of closest approach (DCA) for a global track is a quantity that is available to cut on during event reconstruction in STAR. If the track is a primary track, then the DCA is < 3 [cm]. The type of tracks used during the association are primary tracks (recall that the hadronic track sample being used is defined as being associated with an Υ candidate). The associated tracks are a composite of both associated$_{trueprimarytracks}$ and associated$_{pile-uptracks}$. The reconstructed Υ candidate being associated with the hadronic tracks is located, by definition, at the primary vertex. A global (associated) track, as reconstructed by the TPC, is physically displaced from the location of the primary vertex (again, Υ candidate is the anchor point for the location of the primary vertex) and it is this distribution of the associated track's 'DCA' that is used to infer or reject the desired the pile-up present in the associated tracks. Figure 4.40 shows the associated tracks in the DCA < 3 [cm] region. It is clear that there is a statistically significant portion of tracks having a DCA < 1 [cm].

The effect of a DCA < 1 [cm] cut may be seen from the results in Table 4.12.

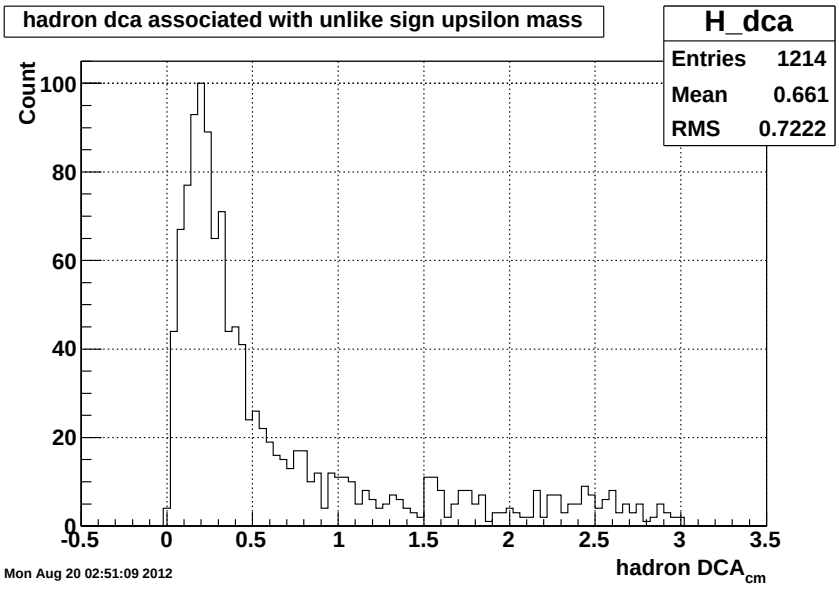

Figure 4.40: Associated hadron candidates: DCA [cm]. There are 954 associated hadrons at DCA < 1 [cm].

The value of α (provides a direct handle on the effect of a DCA cut in data relative to embedding. The DCA < 1 [cm] cut relative to the 'baseline cut' has a value of $\alpha_{data} \approx 0.87$ in data relative to the embedding value $\alpha_{embedding} \approx 0.96$.

4.10.2 Luminosity Dependence

The luminosity throughout any given run changes, and the luminosity therein (high or low) contributes directly to the level of pile-up present in the data collected. The splitting of the Υ-triggered data into 'high-luminosity' and 'low-luminosity' runs by defining a BBC coincidence cut-off rate[26] allows for a first-order study into a possible relationship between the presence of pile-up present in the Υ + hadron correlation function. Figure 4.41 shows the BBC coincidence rate for Run-9 p+p data low-luminosity min-bias data, where the division between low- and high-luminosity is

[26]Measured relative to a low-luminosity Minimum-Bias data set.

defined to be at 400 kHz. Figure 4.42 shows a red-line placed at the BBC coincidence

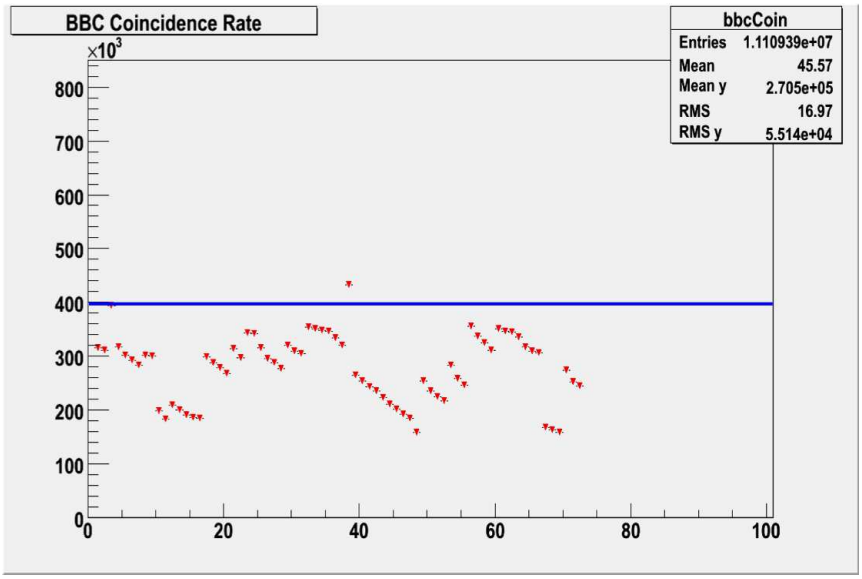

Figure 4.41: Low-luminosity MinBias coincidence rate in Run-9 p+p data: A BBC coincidence rate of 400 kHz is defined as the dividing line between low- and high-luminosity in Run-9 Υ-triggered data.

rate of 400 kHz, which is used on the Run-9 p+p Υ-triggered data to split of the data into high- and low-luminosity.

Figure 4.43 shows that the background corrected $\Delta\Phi$-correlation in data with the 'baseline + DCA $<$ 1 [cm]' cut applied (red-squares) relative to a split of the data into the low-luminosity 'baseline' cut (green-triangles)[27] $\Delta\Phi$-correlation in data.

Figure 4.44 shows that the background corrected $\Delta\Phi$-correlation in data with the 'baseline + DCA $<$ 1 [cm]' cut applied (red-squares) and the high-luminosity

[27]The mass-window has a S/B = 87/17 $\approx$ 5.12.

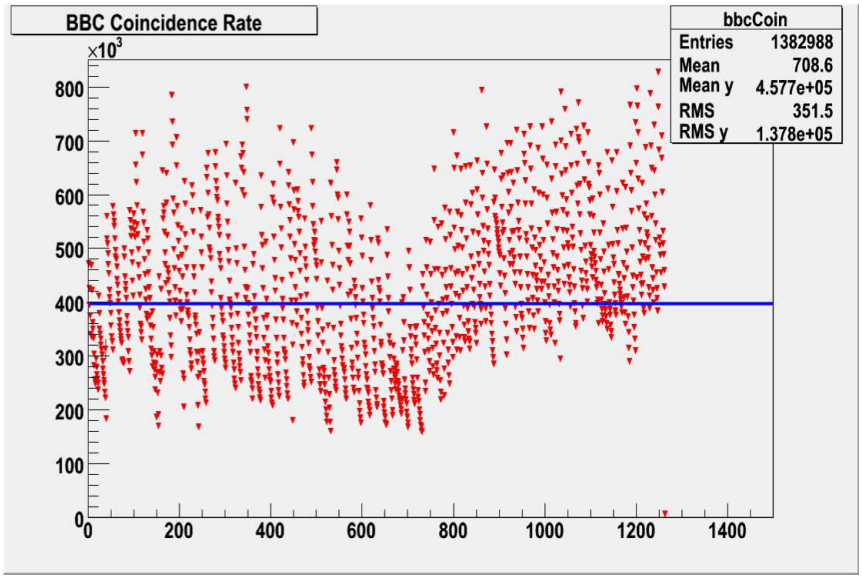

Figure 4.42: Run-9 Υ-triggered data. A BBC coincidence rate of 400 kHz separates the data into low- and high-luminosity.

'baseline' cut (green-triangles)[28] $\Delta\Phi$-correlation in data. In each Figure 4.43 and Figure 4.44, the $\Delta\Phi$-correlation prediction from a pile-up-free PYTHIA (blue-circles) is also shown. It can be seen that there is not a clear difference in the $\Delta\Phi$-correlation between low-luminosity and high-luminosity. The errors associated with the low- and high-luminosity $\Delta\Phi$-correlation are considerable.

4.10.3 Two-dimensional Distance of Closest Approach (DCA_D)

The distance of closest approach (DCA_D) for a global track is the 2-dimensional transverse version of the DCA, also available during event reconstruction in STAR. The 2-dimensional quantity is in the x-y dimensions of the STAR coordinate system, and it is known to be useful in the removal of pile-up in jet reconstruction analyses. The DCA_D cut is a p_T-dependent cut, and the pile-up tracks are rejected via the p_T-

[28]The mass-window has a S/B = 160/26 $\approx$ 6.15.

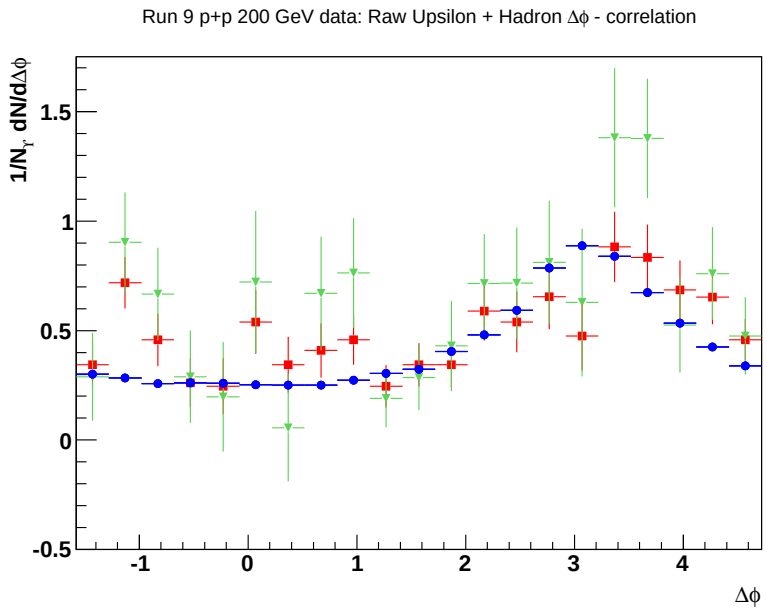

Figure 4.43: Low-luminosity $\Delta\Phi$-correlation in Run-9 p+p data: Background subtracted (red-square), Low-luminosity (green-triangle), and PYTHIA (blue-circle).

dependent contour-cuts[29], defined in Table 4.13. Figure 4.45 shows that the effect of the DCA_D is the removal of only a small fraction of associated tracks that populate the regions typically identified with pile-up.

The effect of the DCA_D cut may also be seen from the results in Table 4.12. The value of β (which can also be thought of as the ratio of ρ/δ) shows that the effect of a DCA_D cut in data vs. embedding. The ratio in data of $(\rho/\delta)_{data} = 0.74/0.74 \approx 1$ has approximately the same ratio in the embedding of $(\rho/\delta)_{embedding} = 0.83/0.83 \approx 1$. I.e. the $\chi^2 < 6$ cut has no additional effect on background rejection.

[29]Recall that Υ-associated hadrons already satisfy $\mathrm{p}_T > 0.5$ GeV/c.

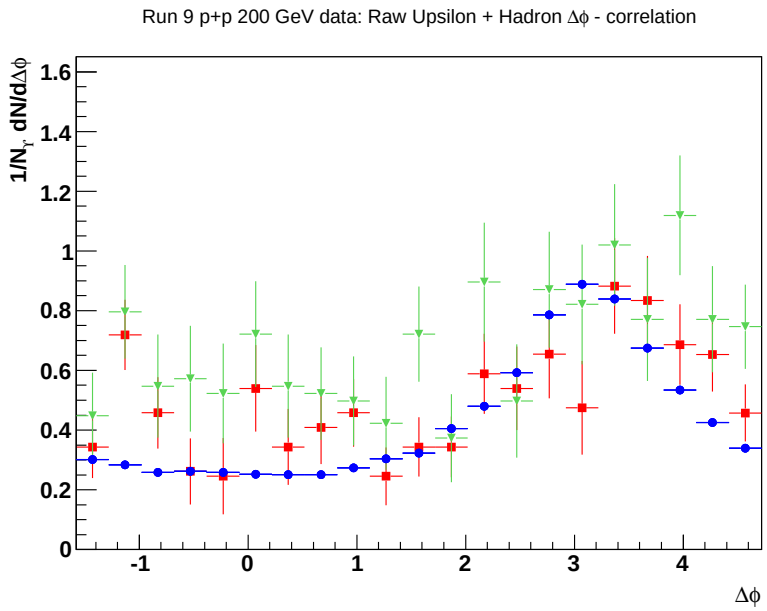

Figure 4.44: High-luminosity $\Delta\Phi$-correlation in Run-9 p+p data: Background subtracted (red-square), High-luminosity (green-triangle), and PYTHIA (blue-circle).

4.10.4 Helix Fit Quality (χ^2)

The number of TPC fit points and the helical fits was discussed previously. The χ^2 distribution is a measure of the difference in the helix fit quality to a track in the case for which the primary vertex is used, as opposed to the case when a primary vertex is not used. Figure 4.46 shows that the statistically significant portion of the associated tracks reside below a region $\chi^2 < 2$.

The effect of the $\chi^2 < 6$ cut may also be seen from the results in Table 4.12. The value of η (which can also be thought of as the ratio of δ/α) shows that the effect of a $\chi^2 < 6$ cut in data vs. embedding. The ratio in data of $(\delta/\alpha)_{data} = 0.74/0.87 \approx 0.85$ has approximately the same ratio in the embedding of $(\delta/\alpha)_{embedding} = 0.83/0.96 \approx 0.86$. I.e. the DCA_D cut does not provide additional background rejection.

Table 4.13: The p_T-dependent DCA_D cut

Cut p_T [GeV/c]	**Cut DCA_D [cm]**
$p_T < 0.5$	± 2
$p_T = 0.5$ to 1.0	'along the line'
$p_T > 1.0$	± 1

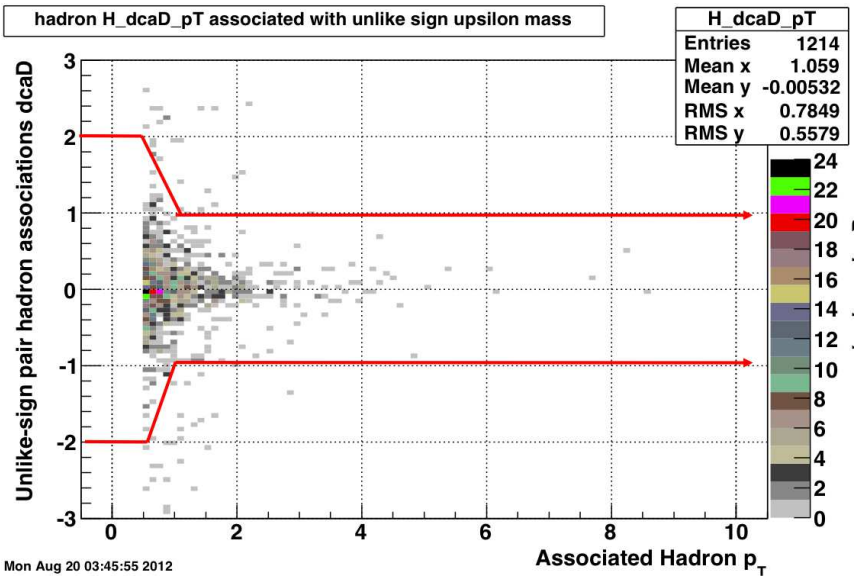

Figure 4.45: Associated hadron distribution in Run-9 p+p data: DCA_D [cm].

4.10.5 Optimizing Pile-up Rejection

In summary, a systematic comparison between the various pile-up rejection 'bundles' showed that the ratio α (DCA < 1 [cm]) tends to reject more in data than in embedding (88% *vs.* 96%), whereas the ratio β (DCA_D cut) rejected virtually the same percentage of hadronic tracks in data and embedding (98% *vs.* 96%), implying that DCA_D is not effective for rejecting the pile-up. The ratio ξ ($\chi^2 < 6$) rejects

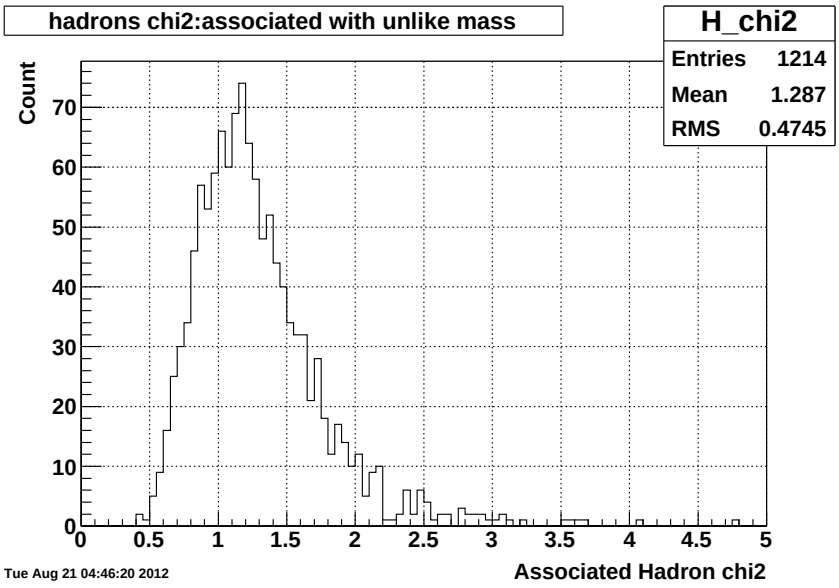

Figure 4.46: Associated hadron distribution in Run-9 p+p data: χ^2.

more in data than embedding, however it does not reject any additional pile-up after the application of a DCA < 1 [cm] cut. The ratio η (measure of $\chi^2 < 6$ + DCA $<$ 1 [cm] cut strength) shows the effect of $\chi^2 < 6$ is 86%, but no more is removed after applying the DCA < 1 [cm] cut. Therefore, the result is an inefficiency (close to 14% of the good tracks in data and embedding). The conclusion is that using a cut of DCA < 1 [cm] is the most optimal cut for removing pile-up, having the maximum rejection power with highest efficiency.

4.11 The Pile-up Rejected $\Delta\Phi$ - correlation

The reconstructed Υ's S/B in each of the collision-system (p+p and d+Au) was sufficient to suggest that a study of the production-related observables suggested in Chapter 1, however, it may not be so straightforward. In the case of d+Au collisions the level of the 'underlying-event' in d+Au collision will drown any signal in the $\Delta\Phi$

- correlation. To be more specific, in the d+Au collision data, the $\Delta\Phi$ - correlation is more susceptible to significant amounts of non-first-order (hard) partonic processes, or said differently, everything other than the first-order hard partonic processes. The non-first-order (non-hard) processes are called the 'underlying-event' and it is composed of many non-leading processes, such as multiple secondary hard scattering interactions, initial and final state radiation, beam remnants, and of course, pile-up. The magnitude of the underlying-event in d+Au collision washes out any opportunity for seeing a $\Delta\Phi$ - correlation that will bare any tale-tale signature of near-side hadronic activity due to the gluon radiation from CSM and COM production. Figure 4.47 shows the $\Delta\Phi$ - correlation shape (no phi-efficiency correction is applied) in d+Au data with the pile-up removal cut of DCA < 1 [cm] and corrections for combinatorial background contributions (red). The $\Delta\Phi$ - correlation in d+Au data[30] is compared to PYTHIA simulation (blue), where it becomes obvious that the $\Delta\Phi$ - correlation is insignificant relative to the dominating underlying-event.

In the p+p data, there should be a relative agreement between the underlying-event in data and PYTHIA[31], provided that the pile-up has been sufficiently removed. Figure 4.48 shows the $\Delta\Phi$ - correlation shape (no phi-efficiency correction is applied) in p+p data with the pile-up removal cut of DCA < 1 [cm] and corrections (see Appendix A) for combinatorial background contributions (red). The $\Delta\Phi$ - correlation in p+p data is compared to PYTHIA simulation (blue), where it becomes obvious that the $\Delta\Phi$ - correlation underlying event is in relative agreement with PYTHIA's predictions for a no contamination from pile-up scenario with an understood underlying-event.

It is worth looking at the $\Delta\Phi$ - correlation in p+p data relative to the $\Delta\Phi$ -

[30]No interpretation of the concave feature at $\Delta\Phi \approx 3.141$ was pursued.
[31]PYTHIA is inherently a p+p simulation package

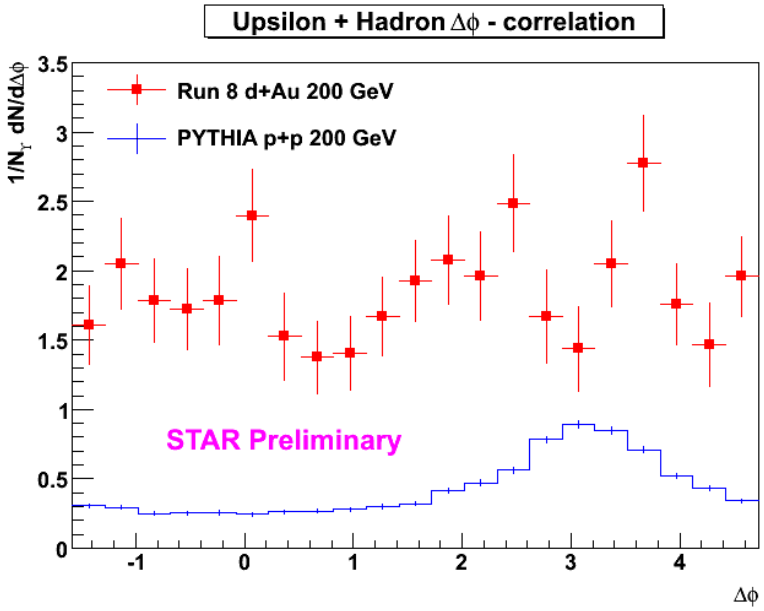

Figure 4.47: $\Delta\Phi$ - correlation: Υ + h at $\sqrt{s}$ = 200 GeV in Run-8 d+Au data.

correlation in d+Au data. Using the multiplicity (M) of the hadronic tracks as a loose measure of the centrality of a d+Au collision, a comparison between the level of the underlying event between d+Au and p+p can be studied. It is expected that the more peripheral d+Au collisions will look more like p+p collisions. While a cut on the hadronic track-multiplicity is not sufficient to completely remove the underlying event nor the remaining pile-up issues, the level of the underlying event in d+Au should scale down to within an order of magnitude, provided that the sufficient Υ statistics in d+Au exist. A rough cut on the hadronic track-multiplicity was chosen by plotting the average number of hadronic tracks for each event containing a reconstructed Υ candidate[32]. Figure 4.49 shows the average number of tracks per reconstructed Υ candidate, for each the d+Au and p+p collision system. A cut on

[32]Only the Υ candidates reconstructing to within an invariant mass-window of 8.0-10.5 GeV/c^2 (Run-8 d+Au data) and 8.0-11.5 GeV/c^2 (Run-9 p+p data) were considered.

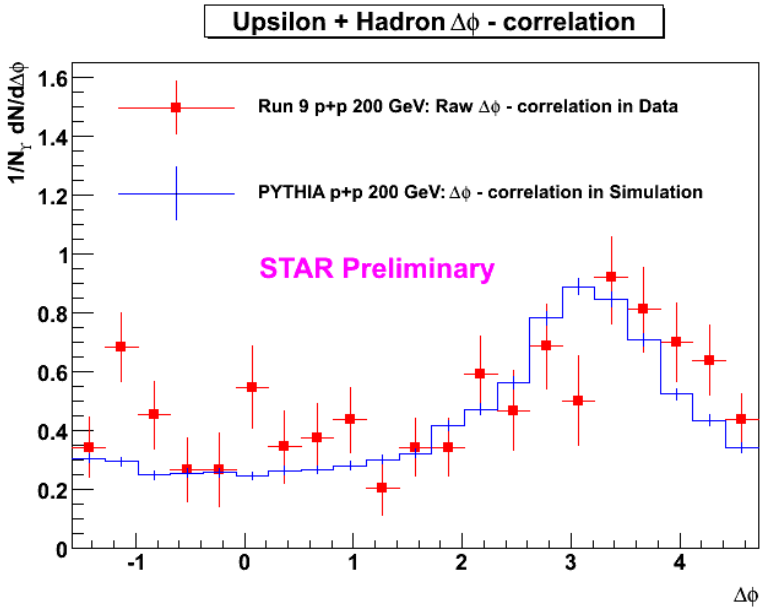

Figure 4.48: $\Delta\Phi$ - correlation: Υ + h at $\sqrt{s} = 200$ GeV in Run-9 p+p data.

the average number of tracks was chosen such that a low track-multiplicity event is defined to be M $<$ 10, and high track-multiplicity event is defined to be M $\geq$ 10.

Figure 4.50 shows the d+Au $\Delta\Phi$ - correlation compared to the p+p $\Delta\Phi$ - correlation for each of the track-multiplicity cuts. Figure 4.50 (top-panel) shows the $\Delta\Phi$ - correlation in d+Au for M $\geq$ 10, where the reconstructed Υ candidates within the invariant mass-window has S/B = 116/26 $\approx$ 4.46. Figure 4.50 (bottom-panel) shows the $\Delta\Phi$ - correlation in d+Au for M $<$ 10, where the reconstructed Υ candidates within the invariant mass-window has S/B = 26/2 $\approx$ 13. It is obvious that the statistical significance of the $\Delta\Phi$ - correlation in d+Au as a function of the track-multiplicity prohibits a quantitative statement from being made. Nonetheless, it is interesting to note that in principle there there does appear to be a qualitative agreement in the $\Delta\Phi$ - correlation system across the collision systems, as d+Au becomes

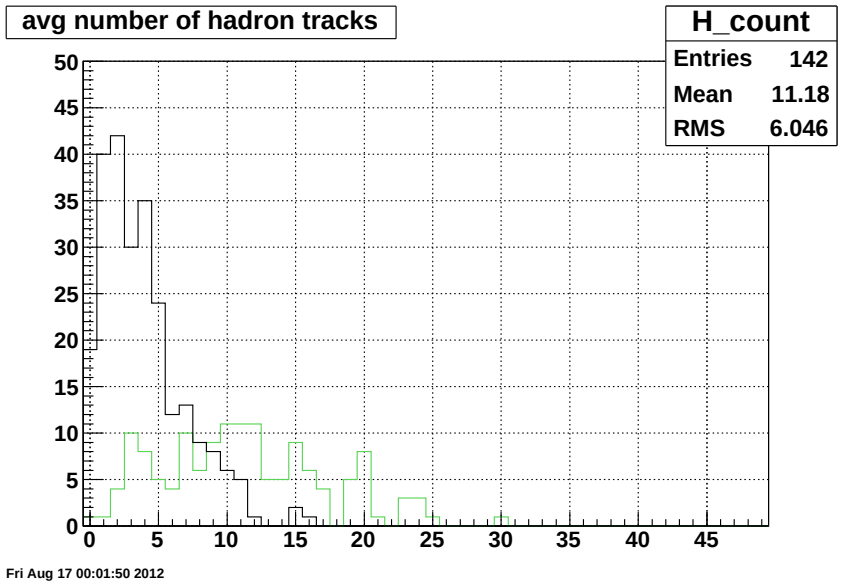

Figure 4.49: Track multiplicity: The average number of track for Run-8 d+Au (green - color online) and Run-9 p+p data (black - color online).

more peripheral.

The correlation has not yet been corrected for acceptance and track efficiencies. Attempts to decompose and discuss the observed correlation shape found in p+p data, into the predicted contributions from gluon activity in described by COM and CSM is not yet justified.

4.12 Charged Pion Embedding and Hadronic Track Corrections

The track reconstruction performance of the TPC is achieved with *reasonable* efficiency [7], however, the 'optimized' pile-up rejection cuts will lower the overall track reconstruction efficiency, and applying an efficiency correction to the data for the relative choice of pile-up rejection cuts will correct (increase) the final yield of pile-up free track population in the $\Delta\Phi$-correlation. Inferences, or attempts to

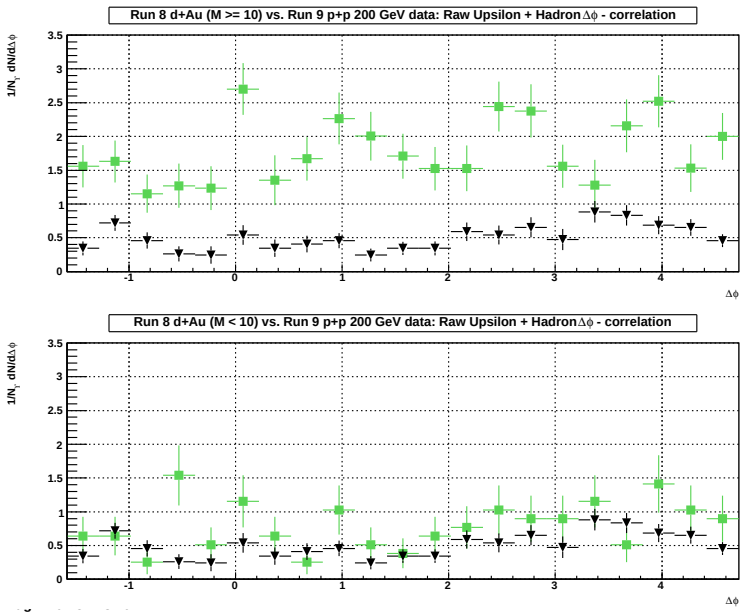

Figure 4.50: $\Delta\Phi$ - correlation and track-multiplicity: Run-8 d+Au (green-squares - color online) and Run-9 p+p data (black-triangles - color online). The $\Delta\Phi$ - correlation for d+Au track-multiplicity M $\geq$ 10 (top-panel) relative to the $\Delta\Phi$ - correlation in p+p. The $\Delta\Phi$ - correlation for track-multiplicity M $<$ 10 (bottom-panel) relative to the $\Delta\Phi$ - correlation in p+p.

draw conclusions with the shape of the $\Delta\Phi$-correlation are necessary before any attempt is made at model comparisons to the data. The standard STAR method for determining the reconstruction efficiency of tracks is done with STAR embedded data: the analysis utilizes STAR π^+ embedding at $\sqrt{s}$ = 200 GeV for 1) d+Au collisions and 2) p+p collisions.

4.12.1 Hadronic Track Acceptance Correction

The track reconstruction efficiency is p_T-dependent, however, angular nature of the $\Delta\Phi$-correlation is inherently dependent on the STAR ϕ-acceptance. The shape of the $\Delta\Phi$-correlation is susceptible to fluctuations directly correlated to ϕ-acceptance

inefficiencies. While the general assumption is that acceptance efficiency is rather isotropic in the ϕ-coordinate, the presence for any small fluctuations must be corrected for because the 'true' shape of the $\Delta\Phi$-correlation is dependent on the STAR ϕ-acceptance and fluctuations may negate or enhance any near-side correlation activity. Figure 4.51 shows the STAR embedded π^+ phi-correction that is used to weight the $\Delta\Phi$ - correlation in Figure 4.48. Figure 4.52 shows the $\Delta\Phi$ - correlation in p+p

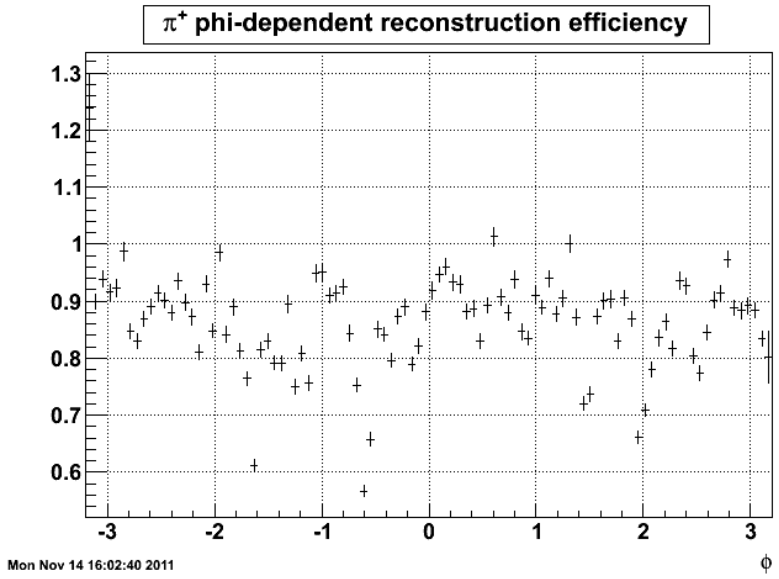

Figure 4.51: ϕ-dependent acceptance (efficiency) correction: π^+ embedded into $\sqrt{s}$ = 200 GeV in Run-9 p+p data.

data that results from the applied track-by-track ϕ-weighted efficiency correction to the $\Delta\Phi$ - correlation in Figure 4.48.

Figure 4.53 shows the full (unlike-sign) Υ candidate p_T-distribution (black-line), and it shows the associated-hadrons (associated with the unlike-sign candidates) p_T-

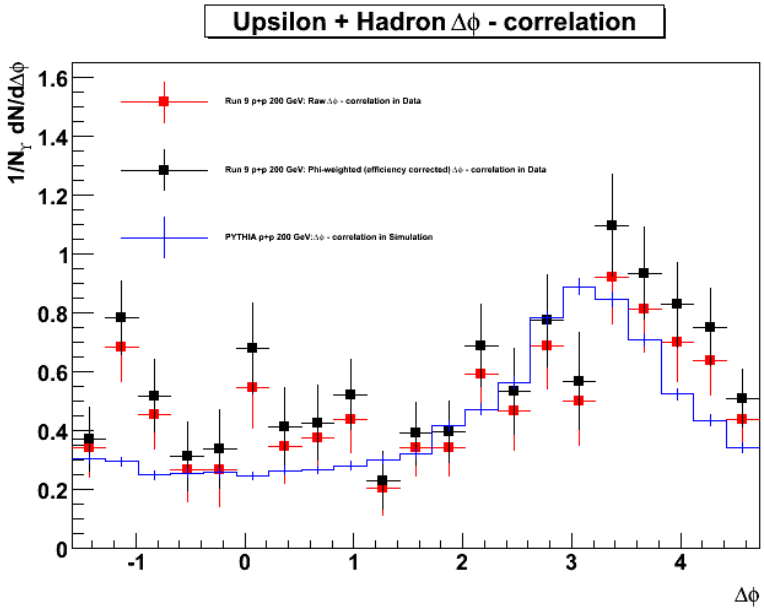

Figure 4.52: $\Delta\Phi$ - correlation: Pile-up removed and ϕ-dependent track efficiency corrected at $\sqrt{s} = 200$ GeV in Run-9 p+p data.

distribution (black-line). Looking for any 'soft' features of the associated-hadrons, the p_T was further subdivided into the near-side and away-side contributions. Figure 4.54 shows all associated-hadrons (associated with the unlike-sign candidates) p_T-distribution (black-line), along with the p_T-distributions for near-side (black-fill), and away-side (yellow-fill). The near-side p_T-distribution does appear to be slightly 'softer' than the away-side p_T-distribution, but a more quantitative comparison to predictions in PYTHIA are needed.

4.13 $\Delta\Phi$ - correlation: Data vs. PYTHIA

The $\Delta\Phi$ - correlation (Figure 4.52) was calculated over the full Υ p_T-distribution. A study of the Υ p_T and the $\Delta\Phi$ - correlation for a given Υ p_T-region in data is compared to the PYTHIA simulation.

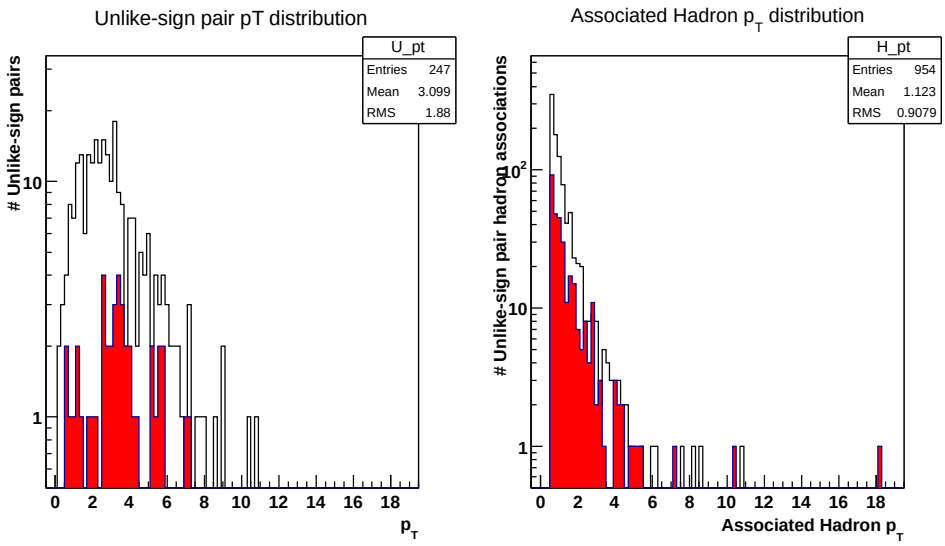

Figure 4.53: Log scale transverse momentum (p_T [GeV/c]) of (left-panel) $\Upsilon \to e^+e^-$ candidates in Run-9 for unlike-sign (black) and like-sign (red-fill), and (right-panel) unlike-sign associated-hadrons (black) and like-sign associated-hadrons (red-fill), in STAR.

4.13.1 Upsilon and Associated Hadron p_T-distributions

The p_T for Υ candidates were separated into the four distinct p_T-regions[33]. The p_T-region for Υ candidates and its associated-hadron p_T-distribution in data is compared to the PYTHIA predictions for the color octet and color singlet contributions. Figure 4.55 shows the full p_T-distribution for the data Υ candidates and the associated-hadrons, along with those same distributions in PYTHIA. Figure 4.56 and Figure 4.57 show the full p_T-distribution for the data Υ candidates and the associated-hadrons, and those in PYTHIA, for different Υ p_T-regions.

[33]Catalogued in Table 4.7.

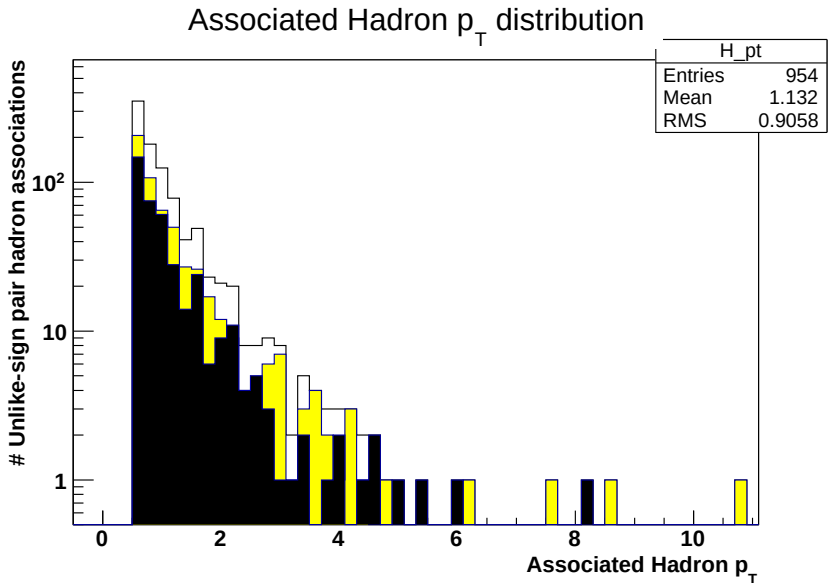

Figure 4.54: Log scale p_T-distribution in Run-9 for unlike-sign associated hadron (black-line), and the near-side associated-hadrons (black-fill), and away-side associated hadrons (yellow-fill), in STAR.

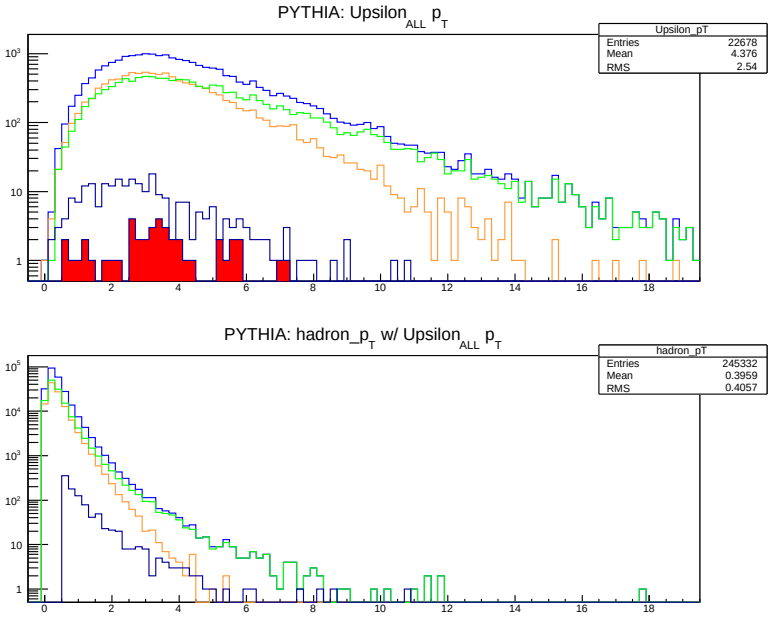

Figure 4.55: Log scale p_T-distribution in Run-9. Upper-panel: unlike-sign candidates (black-line) and like-sign candidates (red-fill) in data, PYTHIA Υ (blue-line), PYTHIA CSM Υ component (orange-line), PYTHIA COM Υ component (green-line). Lower-panel: unlike-sign associated-hadrons (black-line) in data, associated-hadrons (blue-line) in PYTHIA, the CSM component of the associated-hadrons in PYTHIA (orange-line), and the COM component of the associated-hadrons in PYTHIA (green-line).

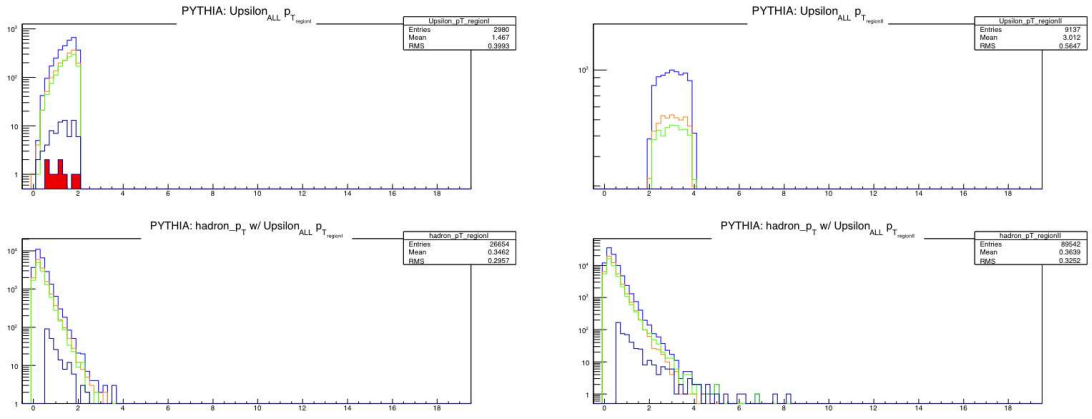

Figure 4.56: Region I and II: Log scale p_T-distribution in Run-9. Upper-panel: unlike-sign candidates (black-line) and like-sign candidates (red-fill) in data, PYTHIA Υ (blue-line), PYTHIA CSM Υ component (orange-line), PYTHIA COM Υ component (green-line). Lower-panel: unlike-sign associated-hadrons (black-line) in data, associated-hadrons (blue-line) in PYTHIA, the CSM component of the associated-hadrons in PYTHIA (orange-line), and the COM component of the associated-hadrons in PYTHIA (green-line).

4.13.2 $\Delta\Phi$ - correlation: p_T-binned

Comparison of the $\Delta\Phi_{data}$ vs. $\Delta\Phi_{PYTHIA}$ correlation is done for the Υ $p_T > 0$ region[34] (Table 4.7). For all Υ with $p_T > 0$ the $\Delta\Phi$ is calculated for four distinct p_T-regions of the associated-hadrons, as catalogued in Table 4.14.

Any deviation between the $\Delta\Phi_{data}$ vs. $\Delta\Phi_{PYTHIA}$ correlations is quantified via a χ^2 analysis, where

$$\chi^2 \equiv \sum_{i=0}^{N} \frac{(X_i - \mu_i)^2}{\sigma_i^2} = \sum_{n=0}^{N_{bins}} \frac{(\Delta\Phi_n^{data} - \Delta\Phi_n^{PYTHIA})^2}{(\sigma_n^{data})^2 + (\sigma_n^{PYTHIA})^2}. \quad (4.9)$$

It is assumed that the uncertainty in PYTHIA is zero ($\sigma_n^{PYTHIA} = 0$), leaving the

[34]This could be extended into each of the four Υ p_T-regions as shown in Figure 4.56 and Figure 4.57, but due to the low statistics in Run-9, the calculation is not performed.

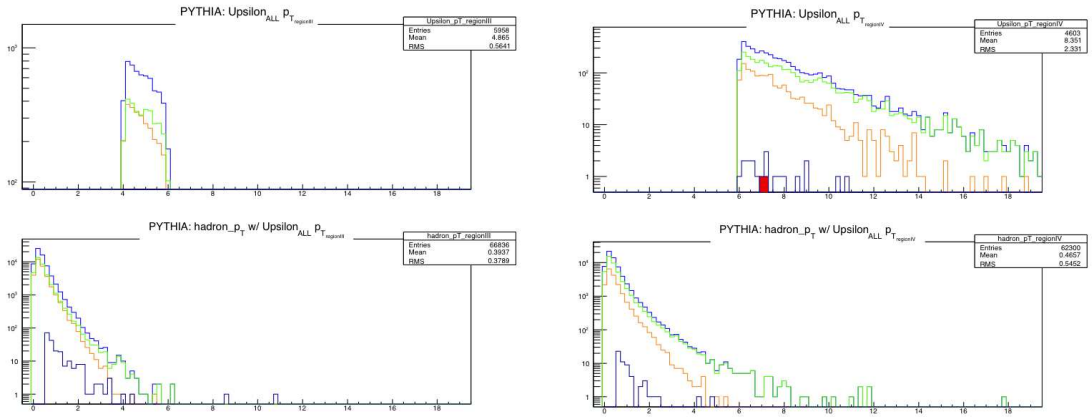

Figure 4.57: Region III and IV: Log scale p_T-distribution in Run-9. Upper-panel: unlike-sign candidates (black-line) and like-sign candidates (red-fill) in data, PYTHIA Υ (blue-line), PYTHIA CSM Υ component (orange-line), PYTHIA COM Υ component (green-line). Lower-panel: unlike-sign associated-hadrons (black-line) in data, associated-hadrons (blue-line) in PYTHIA, the CSM component of the associated-hadrons in PYTHIA (orange-line), and the COM component of the associated-hadrons in PYTHIA (green-line).

only uncertainty entering the χ^2 calculation as that which enters through the data. The definition of Eqn. (4.9) is used as the template for calculating the χ^2 of the full correlation from Eqn. (4.6) ($\Delta\Phi_{full}$ = [-1.58,4.72]),

$$\chi^2_{full} = \sum_{n=1}^{21} \frac{(\Delta\Phi_n^{data} - \Delta\Phi_n^{PYTHIA})^2}{(\sigma_n^{data})^2}. \tag{4.10}$$

The near-side correlation from Eqn. (4.7) ($\Delta\Phi_{near} = |\Delta\Phi| < 1.6$),

$$\chi^2_{near} = \sum_{n=1}^{10} \frac{(\Delta\Phi_n^{data} - \Delta\Phi_n^{PYTHIA})^2}{(\sigma_n^{data})^2}. \tag{4.11}$$

Table 4.14: Associated hadron p_T (p_T^{hadron}) and the unlike- and like-sign count.

Region	$\mathbf{p_T^{hadron}}$	**Unlike-sign count**	**Like-sign count**
	$p_T > 0.5$	247	43
I	$0.5 < p_T \leq 1.0$	74	9
II	$1.0 < p_T \leq 2.0$	112	22
III	$2.0 < p_T \leq 3.0$	42	10
IV	$p_T > 3.0$	19	2

The away-side correlation from see Eqn. (4.8) ($\Delta\Phi_{away} = |\Delta\Phi - 3.141| < 1.6$),

$$\chi^2_{away} = \sum_{n=11}^{21} \frac{(\Delta\Phi_n^{data} - \Delta\Phi_n^{PYTHIA})^2}{(\sigma_n^{data})^2}. \tag{4.12}$$

The χ^2 calculations were done with respect to the PYTHIA$_{CSM+COM}$[35], and with respect to the color octet (PYTHIA$_{COM}$) and color singlet (PYTHIA$_{CSM}$) components. The Figure 4.58 shows the $\Delta\Phi_{data}$ vs. $\Delta\Phi_{PYTHIA}$ correlations for Υ with $p_T > 0$ and associated-hadron by p_T-region. The PYTHIA does not show any significant difference between the CSM (orange) and COM (green), when looking over all p_T. However, as the PYTHIA CSM and COM comparisons are separated into p_T-bins (regions), differences between CSM and COM do appear, but statistics in data are limited. The Table 4.15 consolidates the results of the χ^2 calculation in Figure 4.58. Discussion of the χ^2 analysis between PYTHIA components of the CSM and COM relative to data is discussed in the next chapter.

[35] PYTHIA$_{CSM+COM}$ = PYTHIA$_{CSM}$ + PYTHIA$_{COM}$

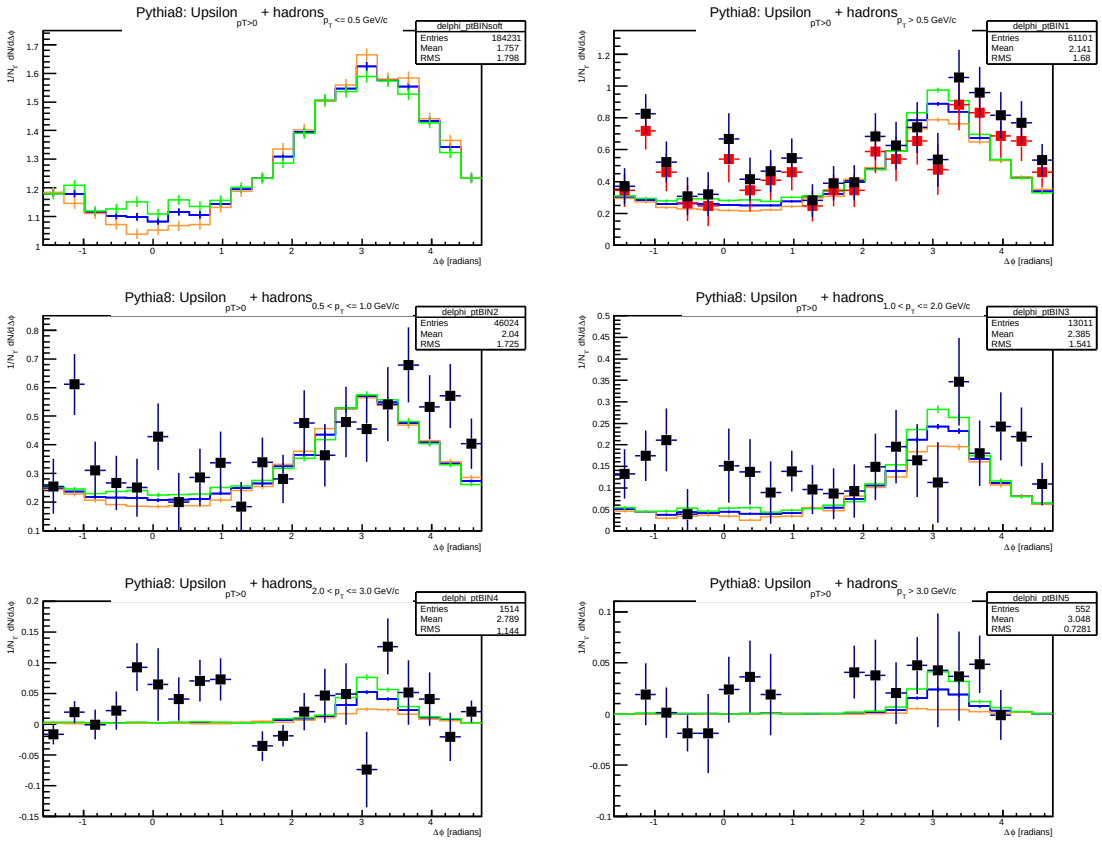

Figure 4.58: $\Delta\Phi_{data}$ vs. $\Delta\Phi_{PYTHIA}$: Efficiency corrected and background subtracted unlike-sign candidates (black-squares) in data, PYTHIA Υ (blue-line), PYTHIA CSM Υ component (orange line), PYTHIA COM Υ component (green-line).

Table 4.15: $\Delta\Phi$: χ^2/d.o.f. values using all reconstructed Υ with $\mathbf{p}_T^{\Upsilon} > \mathbf{0}$ and associated hadrons, in STAR Run-9 (2009) p+p data at $\sqrt{s}$ = 200 GeV compared to PYTHIA simulation.

$\Delta\Phi$	$\mathbf{p}_T^{hadron}$	$\chi^2_{full}/d.o.f.$	$\chi^2_{near}/d.o.f.$	$\chi^2_{away}/d.o.f.$
$\Delta\Phi_{CSM+COM}$	$p_T > 0.5$	3.03	3.90711	2.25171
	$0.5 < p_T \leq 1.0$	1.58145	1.94862	1.24766
	$1.0 < p_T \leq 2.0$	1.59966	2.1323	1.11544
	$2.0 < p_T \leq 3.0$	2.43676	3.56698	1.40929
	$p_T > 3.0$	nan	nan	nan
$\Delta\Phi_{CSM}$	$p_T > 0.5$	3.28543	4.49027	2.19013
	$0.5 < p_T \leq 1.0$	1.70307	2.23748	1.21725
	$1.0 < p_T \leq 2.0$	1.71553	2.35748	1.13195
	$2.0 < p_T \leq 3.0$	2.19056	3.0275	1.42971
	$p_T > 3.0$	nan	nan	nan
$\Delta\Phi_{COM}$	$p_T > 0.5$	2.89738	3.44809	2.39673
	$0.5 < p_T \leq 1.0$	1.50006	1.7419	1.2802
	$1.0 < p_T \leq 2.0$	1.54452	1.9504	1.17554
	$2.0 < p_T \leq 3.0$	1.91425	2.41543	1.45864
	$p_T > 3.0$	nan	nan	nan

5. SUMMARY AND DISCUSSION OF RESULTS AND OUTLOOK

5.1 Discussion of Results

The high signal to background ratio (S/B) in Υ at the STAR experiment at RHIC made it practical to investigate both the Υ(nS) [n = 1, 2, 3] line-shape and the Υ production mechanism.

5.1.1 Upsilon (nS) line-shape

A study of the Υ(nS) [n = 1, 2, 3] mass states was performed with use of the embedded data and the relative contributions of the Υ(nS) states were determined using two different fitting conditions. Allowing the relative contributions of the Υ(nS) states to vary, a fit with χ^2/d.o.f. = 11.52/12 was obtained. Fixing the relative ratios of the Υ(nS) states to the previously measured branching ratios and calculated cross-sections at NLO, a fit with χ^2/d.o.f. = 12.91/14 was obtained. The ratios of $\Upsilon(1S)/\Upsilon(2S) = 2.2 \pm 1.5$ and $\Upsilon(1S)/\Upsilon(3S) = 26 \pm 130$ were measured in the Run-9 p+p data and are in agreement with the results of Eqn. (4.2) and Eqn. (4.3). The contributions coming from Drell-Yan were also in agreement between the two different fitting procedures. It can concluded that a reasonable separation of at least the 1S from the 2S+3S states may be made if one makes mass cuts of m $<$ 9.5 GeV and m $<$ 10 GeV. The Υ(nS) cross-sections were not intended to be measured in this thesis, and further exploration into the cross-section of each Υ(nS) state would require a more detailed analysis. A non-negligible presence of polarized Drell-Yan background underneath the Υ invariant mass distribution is noted and its effect on the Υ polarization measurement was discussed.

5.1.2 *Upsilon Spin-Alignment*

The $\cos(\theta)$ distribution over all p_T was fit with a polynomial of second-order $(1 + \alpha^2)$, yielding a large Υ spin-alignment (polarization) value of $\alpha = 1 \pm 0.3$, although with a significant error and χ^2/d.o.f. $= 18.71/7$. Figure 5.1 shows the NLO and NNLO CSM calculations at Tevatron energies ($\sqrt{s} = 1.8$ TeV). On average, the p_T for Υ's produced in STAR (Figure 4.35) makes the comparison of the measured value of $\alpha = 1 \pm 0.3$ not directly comparable to the polarization values predicted by NNLO in the CSM framework.

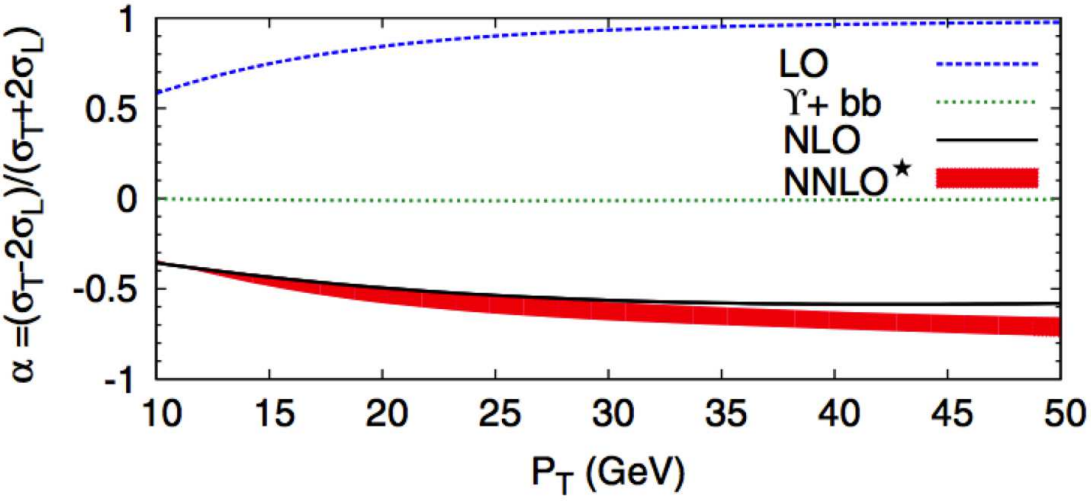

Figure 5.1: Polarization vs. p_T for the CSM NLO and NNLO calculations [8].

Figure 5.2 polarization values predicted by the COM model (NRQCD) calculation as a function of p_T, overlayed with CDF measurements for J/ψ and Υ(2S) polariza-

tion. It can be seen that the distribution of the polarization values predicted by the COM model (NRQCD) is not consistent with the general trend of the CDF data at high-p_T [3], where large transverse polarization is predicted. However, the NNLO CSM (Figure 5.1) does appear to do a reasonable job of describing the observed Υ polarization distribution seen at the Tevatron.

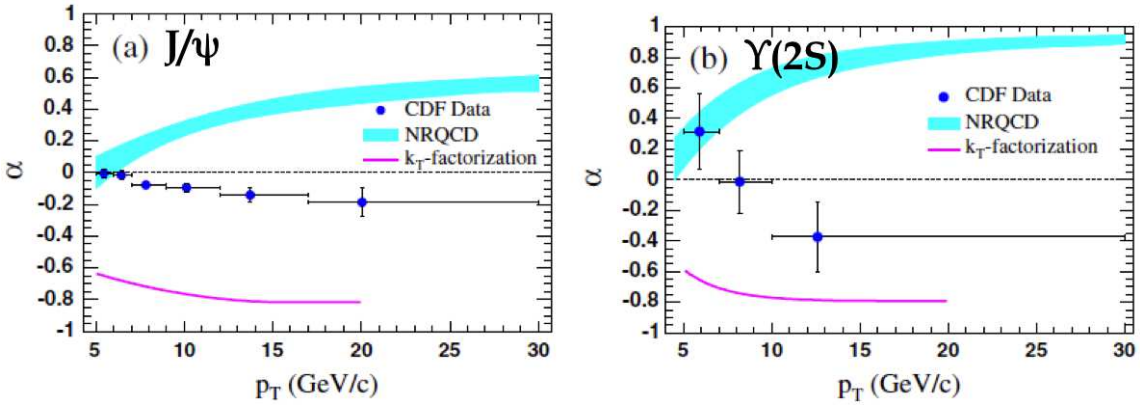

Figure 5.2: Polarization vs. p_T for the COM (NRQCD) calculations [3].

A direct comparison of $\alpha = 1 \pm 0.3$ in STAR to the COM polarization predictions (calculated for CDF at Tevatron energies) is not calculated below $p_T < 5$ GeV/c, where again, the Figure 4.35 shows the larger fraction of Υ p_T at STAR are produced. However, the $\alpha = 1 \pm 0.3$ measured STAR at RHIC may be able to provide a constraint on existing models.

The Drell-Yan contribution to the polarization may skew the Υ polarization measurement. However, since the Drell-Yan is known to be highly polarized from E866 [24], and this analysis found that the contribution to the Υ mass peak was approximately 25% $\pm$ 4% from Drell-Yan background, then the polarization signal of the

true Υ signal may conceivably gave a different polarization than the quoted $\alpha = 1 \pm 0.3$. However, as discussed in Chapter 4, normalizing the Drell-Yan contribution and using the E866 value to be $\alpha_{DY} = 1.0 \pm 0.05$, the subtraction results in $\alpha_{\Upsilon} = 1 \pm 0.3$.

5.1.3 Upsilon $\Delta\Phi$ - correlation

The Υ + h correlation measurement looked for the presence of hadronic activity directly around the reconstructed Υ. In Run-8 d+Au collisions (approximately 32 nb^{-1} integrated luminosity), the underlying event swamped any chance of seeing structure in the near-side azimuthal correlation. The activity (or lack thereof) in the azimuthal correlations between the Υ and charged hadrons in Run-9 p+p collisions (approximately 20 pb^{-1} integrated luminosity) was compared to the PYTHIA[1] simulations. The results from the χ^2 analysis (Table 4.15) show that when all $p_T > 0.5$ associated-hadrons are used in the azimuthal correlation, the comparison between PYTHIA and data (near-side and away-side) shows that χ^2/d.o.f. values for the away-side are slightly in better agreement than the χ^2/d.o.f. values for the near-side. In general, the χ^2/d.o.f. for the away-side tends to agree better than the values of χ^2/d.o.f. on the near-side, pointing to a increased disagreement between PYTHIA and data. A decrease in statistics (increasing the error in data) increases the potential disagreement between PYTHIA and data, when calculating the analogous χ^2/d.o.f. for a $\Delta\Phi$-correlation binned by associated-hadron p_T. A general trend is observed that χ^2/d.o.f. values for the away-side are in better agreement than the χ^2/d.o.f. values for the near-side as the $\Delta\Phi$-correlation is explored for associated-hadron p_T bins. Considering the χ^2/d.o.f. values in the associated-hadron binning of $0.5 < p_T < 1.0$ and $1.0 < p_T < 2.0$, for the data relative to COM is it seen

[1]All discussion on PYTHIA refer to the PYTHIA 8.1 C++ rewrite [63].

that near-side is moving more into agreement, having χ^2/d.o.f. < 2. While this is a 'softer' associated-hadronic p_T-region in the data, placing too much emphasis on this is difficult because of the lack of statistics. At even softer associated-hadronic p_T (p_T < 0.5), the upper-most left-panel in Figure 4.58 shows that the near-side does have a relatively higher contribution from COM than CSM, but no prominent associated-hadron 'activity' from soft gluon-radiation is obvious. Overall, data agrees better at low-p_T than at high-p_T. Increased Υ statistics as well as a more advanced COM and CSM event generator may be a way forward.

5.2 Outlook

The RHIC collider and STAR experiment may yield future possibilities into studying the Υ production mechanism, which has been outlined within this thesis. The possibility of increased statistics in Run-11 p+p collisions[2] provide more reconstructed candidates in the $\Upsilon \rightarrow e^+e^-$ decay channel. Future measurements of Υ spin-alignment may also want to use the Collins-Soper frame in addition to the helicity frame used in this thesis, while the azimuthal correlation measurements will also want to explore the study of a 'tuned' event generator 'MADonia' [51], in addition to the PYTHIA framework which showed no significant discriminating power between CSM and COM production.

Expansion of the STAR experiment to include muon lepton detection capabilities with a large mid-rapidity coverage detector knowns as the muon telescope detector (MTD) will allow for the use of muons in future Υ analyses. The $\Upsilon \rightarrow \mu^+\mu^-$ decay channel allows analyses to sidestep the issue of γ-conversion pairs, and minimize the contributions from Dalitz decay, as well as suffering less from radiative losses in detector materials. The MTD triggering scenarios extend from low to high-pT

[2]Run-11 integrated luminosity is greater than the Run-9 integrated luminosity used in this thesis.

can provide excellent mass resolution for attempts at separating the different Υ(nS) states. The prototype of the MTD at STAR was operational from Run-7 to Run-10.

REFERENCES

[1] V.M. Abazov et al. Measurement of Inclusive Differential Cross Sections for υ_{1S} Production in $p\bar{p}$ Collisions at $\sqrt{s} = 1.96$-TeV. *Phys.Rev.Lett.*, 94:232001, 2005.

[2] B.I. Abelev et al. J/psi Production at High Transverse Momentum in p+p and Cu+Cu Collisions at s(NN)**1/2 = 200GeV. *Phys.Rev.*, C80:041902, 2009.

[3] A. Abulencia et al. Polarization of J/ψ and ψ_{2S} Mesons Produced in $p\bar{p}$ Collisions at $\sqrt{s} = 1.96$-TeV. *Phys.Rev.Lett.*, 99:132001, 2007.

[4] D. Acosta et al. Υ Production and Polarization in $p\bar{p}$ Collisions at $\sqrt{s} = 1.8$-TeV. *Phys.Rev.Lett.*, 88:161802, 2002.

[5] A. Adare et al. J/ψ Production versus Transverse Momentum and Rapidity in $p^{+}p$ Collisions at $\sqrt{s} = 200$-GeV. *Phys.Rev.Lett.*, 98:232002, 2007.

[6] T. Affolder et al. Measurement of J/ψ and $\psi(2S)$ Polarization in $p\bar{p}$ Collisions at $\sqrt{s} = 1.8$ TeV. *Phys.Rev.Lett.*, 85:2886–2891, 2000.

[7] M. Anderson, J. Berkovitz, W. Betts, R. Bossingham, F. Bieser, et al. The Star Time Projection Chamber: A Unique Tool for Studying High Multiplicity Events at RHIC. *Nucl.Instrum.Meth.*, A499:659–678, 2003.

[8] P. Artoisenet, John M. Campbell, J.P. Lansberg, F. Maltoni, and F. Tramontano. Υ Production at Fermilab Tevatron and LHC Energies. *Phys.Rev.Lett.*, 101:152001, 2008.

[9] R. Baier and R. Ruckl. Hadronic Production of J/psi and Upsilon: Transverse Momentum Distributions. *Phys.Lett.*, B102:364, 1981.

[10] R. Baier and R. Ruckl. Hadronic Collisions: A Quarkonium Factory. *Z.Phys.*, C19:251–266, 1983.

[11] M. W. Bailey. Charmonium and Bottomonium Production in p-pbar Collisions at CDF. *ArXiv High Energy Physics - Experiment e-prints*, August 1996.

[12] V. Barger, Kingman Cheung, and W. Y. Keung. z-boson decays to heavy quarkonium. *Phys. Rev. D*, 41:1541–1546, Mar 1990.

[13] M. Beddo et al. The STAR Barrel Electromagnetic Calorimeter. *Nucl.Instrum.Meth.*, A499:725–739, March 2003.

[14] Edmond L. Berger and Daniel L. Jones. Inelastic Photoproduction of J/psi and Upsilon by Gluons. *Phys.Rev.*, D23:1521–1530, 1981.

[15] F. Bergsma et al. The STAR Detector Magnet Subsystem. *Nucl.Instrum.Meth.*, A499:633–639, 2003.

[16] J. Beringer et al. Review of Particle Physics (RPP). *Phys.Rev.*, D86:010001, 2012.

[17] H.J. Bhabha. The Scattering of Positrons by Electrons with Exchange on Dirac's Theory of the Positron. *Proc.Roy.Soc.Lond.*, A154:195–206, 1936.

[18] E. D. Bloom and C. W. Peck. Physics with the Crystal Ball Detector. *Annual Review of Nuclear and Particle Science*, 33:143–198, 1983.

[19] Geoffrey T. Bodwin, Eric Braaten, and G. Peter Lepage. Rigorous QCD Predictions for Decays of P Wave Quarkonia. *Phys.Rev.*, D46:1914–1918, 1992.

[20] Geoffrey T. Bodwin, Eric Braaten, and G. Peter Lepage. Rigorous QCD Analysis of Inclusive Annihilation and Production of Heavy Quarkonium. *Phys.Rev.*, D51:1125–1171, 1995.

[21] Geoffrey T. Bodwin, Eric Braaten, Tzu Chiang Yuan, and G. Peter Lepage. P Wave Charmonium Production in B Meson Decays. *Phys.Rev.*, D46:3703–3707, 1992.

[22] Eric Braaten, Kingman Cheung, and Tzu Chiang Yuan. Z^0 decay into charmonium via charm quark fragmentation. *Phys. Rev. D*, 48:4230–4235, Nov 1993.

[23] Eric Braaten, Sean Fleming, and Tzu Chiang Yuan. Production of Heavy Quarkonium in High-energy colliders. *Ann.Rev.Nucl.Part.Sci.*, 46:197–235, 1996.

[24] C.N. Brown et al. Observation of Polarization in Bottomonium Production at $\sqrt{s} = 38.8$-GeV. *Phys.Rev.Lett.*, 86:2529–2532, 2001.

[25] Manuel Calderon de la Barca Sanchez. Estimating Drell-Yan Contribution from NLO Calculation. http://drupal.star.bnl.gov/STAR/pwg/heavy-flavor/upsilon-analysis/estimating-drell-yan-contribution-nlo-calculation; Language: English. [Accessed: 11/26/2012].

[26] Shailesh Chandrasekharan. Solutions to Sign Problems in Lattice Yukawa Models. *Phys.Rev.*, D86:021701, 2012.

[27] Mauro R. Cosentino. Upsilon Measurement in STAR. *Int.J.Mod.Phys.*, E16:2110–2115, 2007.

[28] Philippe de Forcrand. Simulating QCD at Finite Density. *PoS*, LAT2009:010, 2009.

[29] T. A. Degrand and D. Toussaint. The Decay of b Quarks into ψ's. *Physics Letters B*, 89:256–258, January 1980.

[30] S. Durr, Z. Fodor, J. Frison, C. Hoelbling, R. Hoffmann, et al. Ab-Initio Determination of Light Hadron Masses. *Science*, 322:1224–1227, 2008.

[31] A. Emerick, X. Zhao, and R. Rapp. Bottomonia in the Quark-Gluon Plasma and their Production at RHIC and LHC. *Eur.Phys.J.*, A48:72, 2012.

[32] R.P. Feynman. Space - time Approach to Quantum Electrodynamics. *Phys.Rev.*, 76:769–789, 1949.

[33] R.P. Feynman. Mathematical Formulation of the Quantum Theory of Electromagnetic Interaction. *Phys.Rev.*, 80:440–457, 1950.

[34] Murray Gell-Mann. The Eightfold Way: A Theory of Strong Interaction Symmetry. *Unpublished US Atomic Energy Technical Report, CTSL-20, TID-12608*, 1961.

[35] S.L. Glashow. Partial Symmetries of Weak Interactions. *Nucl.Phys.*, 22:579–588, 1961.

[36] D.J. Gross and Frank Wilczek. Asymptotically Free Gauge Theories. 1. *Phys.Rev.*, D8:3633–3652, 1973.

[37] D.J. Gross and Frank Wilczek. Ultraviolet Behavior of Nonabelian Gauge Theories. *Phys.Rev.Lett.*, 30:1343–1346, 1973.

[38] D.J. Gross and Frank Wilczek. Asymptotically Free Gauge Theories. 2. *Phys.Rev.*, D9:980–993, 1974.

[39] Sourendu Gupta. QCD at Finite Density. *PoS*, LATTICE2010:007, 2010.

[40] M. Harrison, Stephen G. Peggs, and T. Roser. The RHIC Accelerator. *Ann.Rev.Nucl.Part.Sci.*, 52:425–469, 2002.

[41] Richard W. Haymaker. Confinement Studies in Lattice QCD. *Phys.Rept.*, 315:153–173, 1999.

[42] N. Jarosik, C.L. Bennett, J. Dunkley, B. Gold, M.R. Greason, et al. Seven-Year Wilkinson Microwave Anisotropy Probe (WMAP) Observations: Sky Maps, Systematic Errors, and Basic Results. *Astrophys.J.Suppl.*, 192:14, 2011.

[43] Frithjof Karsch. Lattice Results on QCD Thermodynamics. *Nucl.Phys.*, A698:199–208, 2002.

[44] Aafke C. Kraan. Experimental Aspects of Heavy Quarkonium Production at the LHC. *AIP Conf.Proc.*, 1038:45–54, 2008.

[45] J. H. Kuhn, S. Nussinov, and R. Ruckl. Charmonium production in β-decays. *Z.Phys*, C5:117–120, 1980.

[46] Willis E. Lamb and Robert C. Retherford. Fine structure of the hydrogen atom by a microwave method. *Phys. Rev.*, 72:241–243, Aug 1947.

[47] J.P. Lansberg. On the Mechanisms of Heavy-quarkonium Hadroproduction. *Eur.Phys.J.*, C61:693–703, 2009.

[48] Derek B. Leinweber. Visualizations of Quantum Chromodynamics. http://www.physics.adelaide.edu.au/theory/staff/leinweber/VisualQCD/Nobel Language: English. [Accessed: 11/26/2012].

[49] Ludmila Levkova. QCD at Nonzero Temperature and Density. *PoS*, LATTICE2011:011, 2011.

[50] E.Y. Loh, J.E. Gubernatis, R.T. Scalettar, S.R. White, D.J. Scalapino, et al. Sign Problem in the Numerical Simulation of Many-electron Systems. *Phys.Rev.*, B41:9301–9307, 1990.

[51] Fabio Maltoni and Tim Stelzer. MadEvent: Automatic Event Generation with MadGraph. *JHEP*, 0302:027, 2003.

[52] T. Matsui and H. Satz. J/psi Suppression by Quark-Gluon Plasma Formation. *Phys.Lett.*, B178:416, 1986.

[53] H. David Politzer. Reliable Perturbative Results for Strong Interactions? *Phys.Rev.Lett.*, 30:1346–1349, 1973.

[54] H. David Politzer. Asymptotic Freedom: An Approach to Strong Interactions. *Phys.Rept.*, 14:129–180, 1974.

[55] Johann Rafelski and Berndt Müller. Strangeness production in the quark-gluon plasma. *Phys. Rev. Lett.*, 48:1066–1069, Apr 1982.

[56] R. Rapp, D. Blaschke, and P. Crochet. Charmonium and Bottomonium Production in Heavy-ion Collisions. *Prog.Part.Nucl.Phys.*, 65:209–266, 2010.

[57] R. Reed, J. Balewski, L.S. Barnby, A. Ogawa, J. Lauret, et al. Vertex Finding in Pile-up Rich Events for p+p and d+Au Collisions at STAR. *J.Phys.Conf.Ser.*, 219:032020, 2010.

[58] E. Rutherford. The Scattering of Alpha and Beta Particles by Matter and the Structure of the atom. *Phil.Mag.*, 21:669–688, 1911.

[59] Abdus Salam. Weak and Electromagnetic Interactions. *Conf.Proc.*, C680519:367–377, 1968.

[60] Gerhard A. Schuler. Production of Heavy Quarks and Heavy Quarkonia. *Z.Phys.*, C71:317–328, 1996.

[61] Edward V. Shuryak. Quark-Gluon Plasma and Hadronic Production of Leptons, Photons and Psions. *Phys.Lett.*, B78:150, 1978.

[62] Edward V. Shuryak. The Quark Gluon Plasma. *Sov.Phys.Usp.*, 25:760–761, 1982.

[63] Torbjorn Sjostrand, Stephen Mrenna, and Peter Z. Skands. A Brief Introduction to PYTHIA 8.1. *Comput.Phys.Commun.*, 178:852–867, 2008.

[64] M. Stephanov. QCD Phase Diagram and the Critical Point. *Progress of Theoretical Physics Supplement*, 153:139–156, 2004.

[65] R. Vogt. J/ψ Production and Suppression. *Phys.Rept.*, 310:197–260, 1999.

[66] Steven Weinberg. A Model of Leptons. *Phys.Rev.Lett.*, 19:1264–1266, 1967.

[67] Kenneth G. Wilson. Confinement of Quarks. *Phys.Rev.*, D10:2445–2459, 1974.

[68] Hideki Yukawa. On the Interaction of Elementary Particles. *Proc.Phys.Math.Soc.Jap.*, 17:48–57, 1935.

APPENDIX A

Υ ASSOCIATED-HADRON YIELD PER Υ

The yield of hadrons associated with a true Υ can be obtained from the yields measured in like-sign pairs (LS) and unlike-sign pairs (US). The symbol Y denotes the yield, and the symbol N denotes the number. Considering the unlike-sign yields (Y^{US}), which contain yields of true Υ-associated hadrons as well as yields of background-associated hadrons. The like-sign yields (Y^{LS}) are the yields of hadrons associated to background triggers only. The true Υ-associated yields can be obtained in the following way.

$$\begin{aligned} Y^{US} &\equiv \frac{1}{N^{US}_{trigger}} \frac{dN^{US}}{d(\Delta\Phi)} \\ &= \frac{(N^{\Upsilon+h} + N^{rep+h})}{N^{\Upsilon} + N^{rep}}, \end{aligned}$$

for each $\Delta\Phi$ bin, where the quantity N^{rep} denotes the background contributions from random electron pairs and can be shown to be of order,

$$N^{rep} \approx 2\sqrt{N^{++}N^{--}}.$$

The like-sign triggered pairs are random electron pairs, defined by

$$N^{rep} \equiv N^{LS}$$

and,

$$N^{rep+h} \equiv N^{LS+h}.$$

Hence,

$$\begin{aligned} Y^{US} &\equiv \frac{1}{N^{US}_{trigger}} \frac{dN^{US}}{d(\Delta\Phi)} \\ &= \frac{N^{\Upsilon+h}}{N^{\Upsilon}+N^{LS}} + \frac{N^{LS+h}}{N^{\Upsilon}+N^{LS}}, \end{aligned}$$

for each $\Delta\Phi$ bin.

The desired quantity to extract from the data is the number of hadrons associated with Υ, per Υ trigger;

i.e. the true Υ-associated yield,

$$\frac{N^{\Upsilon+h}}{N^{\Upsilon}}.$$

Next, recall that (Y^{LS}) is the like-sign yield of hadrons associated to background triggers only,

i.e.,

$$\begin{aligned} Y^{LS} &\equiv \frac{1}{N^{LS}_{trigger}} \frac{dN^{LS}}{d(\Delta\Phi)} \\ &= \frac{N^{LS+h}}{N^{LS}}, \end{aligned}$$

for each $\Delta\Phi$ bin.

Rearranging the result of the unlike-sign yields (Y^{US}) and solve for the number of hadrons associated with Υ as follows:

$$Y^{US} = \frac{N^{\Upsilon+h}}{N^{\Upsilon}+N^{LS}} + \frac{N^{LS+h}}{N^{\Upsilon}+N^{LS}}$$

$$\begin{aligned}
\Rightarrow \frac{N^{\Upsilon+h}}{N^{\Upsilon}+N^{LS}} &= Y^{US} - \frac{N^{LS+h}}{N^{\Upsilon}+N^{LS}} \\
&= Y^{US} - \frac{N^{LS+h}}{N^{\Upsilon}+N^{LS}}(\frac{N^{LS}}{N^{LS}}) \\
&= Y^{US} - \frac{N^{LS+h}}{N^{LS}}(\frac{N^{LS}}{N^{\Upsilon}+N^{LS}}) \\
&= Y^{US} - Y^{LS}(\frac{N^{LS}}{N^{\Upsilon}+N^{LS}}),
\end{aligned}$$

where use of the expression for the like-sign yield (Y^{LS}) calculated above is made.

A final algebraic step reduces the preceding equation into the final expression for obtaining the true Υ-associated yields.

$$\frac{N^{\Upsilon+h}}{N^{\Upsilon}} = (\frac{N^{\Upsilon}+N^{LS}}{N^{\Upsilon}})Y^{US} - (\frac{N^{LS}}{N^{\Upsilon}})Y^{LS}.$$

The formula derived is used to correct for background contributions in the Υ-hadron Correlations analysis.

Depending on the strength of the correlation with 'background triggers', as measured by $LS + h$ (recall this notation means like-sign$_{pairs}$ + hadrons), the correction can increase or decrease the strength of the correlation of $US + h$ (recall this notation means unlike-sign$_{pairs}$ + hadrons). For example, if the correlation of background triggers is smaller, its effect on the correlation of the unlike-sign triggers is to wash out or reduce the true Υ + hadron correlation, so the correction must shift upward the unlike-sign correlation.